The Thesis Committee for William Robb Stewart
Certifies that this is the approved version of the following thesis:

Conjugate Heat Transfer Effects on Gas Turbine Film Cooling: Including Thermal Fields, Thermal Barrier Coating, and Contaminant Deposition

APPROVED BY
SUPERVISING COMMITTEE:

Supervisor:

David Bogard

Halil Berberoglu

Conjugate Heat Transfer Effects on Gas Turbine Film Cooling: Including Thermal Fields, Thermal Barrier Coating, and Contaminant Deposition

by

William Robb Stewart, B.S.M.E

Thesis

Presented to the Faculty of the Graduate School of

The University of Texas at Austin

in Partial Fulfillment

of the Requirements

for the Degree of

Master of Science in Engineering

The University of Texas at Austin

May 2014

Dedication

To my family, my soon to be wife, and my roommates.

Acknowledgements

I would like to thank Dr. David Bogard for his support and patience as my professor and supervisor. From him, I learned to think and analyze more critically. Thank you for always questioning my results and conclusions, and forcing me to be confident and thorough in my thoughts. I also would like to thank Dr. Halil Berberoglu for his time spent reading and editing this work as the second reader. Also, I would like to thank the University Turbine Systems Research (UTSR) for funding the bulk of this work.

The other members of the TTCRL were crucial in my time as a graduate student in helping me grow as a researcher. I gained essential knowledge and laughter from each of them. I would like to specifically thank David Kistenmacher for bringing me alongside his work and for his thorough explanations. I would also like to thank Joshua Anderson, John McClintic, Noah Mosberg, Kyle Chavez, Emily Boyd, Sean Klavetter, Gavin Packard and Adam Vaclavik.

I would like to thank my roommates for the incredible community you have been during my time in Austin; my family for their un-ending support; and Lauren Peters for agreeing to marry me while I was in graduate school.

Finally, I would like to thank my God for his compassion, grace, and abounding love; for the death and resurrection of Jesus Christ.

Abstract

Conjugate Heat Transfer Effects on Gas Turbine Film Cooling: Including Thermal Fields, Thermal Barrier Coating, and Contaminant Deposition

William Robb Stewart, M.S.E.

The University of Texas at Austin, 2014

Supervisor: David Bogard

The efficiency of natural gas turbines is directly linked to the turbine inlet temperature, or the combustor exit temperature. Further increasing the turbine inlet temperature damages the turbine components and limits their durability. Advances in turbine vane cooling schemes protect the turbine components. This thesis studies the conjugate effects of internal cooling, film cooling and thermal barrier coatings (TBC) on turbine vane metal temperatures.

Two-dimensional thermal profiles were experimentally measured downstream of a single row of film cooling holes on both an adiabatic and a matched Biot number model turbine vane. The measurements were taken as a comparison to computational simulations of the same model and flow conditions. To improve computational models of the evolution of a film cooling jet as it propagates downstream, the thermal field above

the vane, not just the footprint on the vane surface must be analyzed. This study expands these data to include 2-D thermal fields above the vane at 0, 5 and 10 hole diameters downstream of the film cooling holes. In each case the computational jets remained colder than the experimental jets because they did not disperse into the mainstream as quickly. Finally, in comparing results above adiabatic and matched Biot number models, these thermal field measurements allow for an accurate analysis of whether or not the adiabatic wall temperature was a reasonable estimate of the driving temperature for heat transfer. In some cases the adiabatic wall temperature did give a good indication of the driving temperature for heat transfer while in other cases it did not.

Previous tests simulating the effects of TBC on an internally and film cooled model turbine vane showed that the insulating effects of TBC dominate over variations in film cooling geometry and blowing ratio. In this study overall and external effectiveness were measured using a matched Biot number model vane simulating a TBC of thickness 0.6*d*, where *d* is the film cooing hole diameter. This new model was a 35% reduction in thermal resistance from previous tests. Overall effectiveness measurements were taken for an internal cooling only configuration, as well as for three rows of showerhead holes with a single row of holes on the pressure side of the vane. This pressure side row of holes was tested both as round holes and as round holes embedded in a realistic trench with a depth of 0.6 hole diameters. Even in the case of this thinner TBC, the insulating effects dominate over film cooling. In addition, using measurements of the convective heat transfer coefficient above the vane surface, and the thermal conductivities of the vane wall and simulated TBC material, a prediction technique of the overall effectiveness with TBC was evaluated.

Table of Contents

List of Tables

List of Figures

Nomenclature

Symbols

Bi	Biot number, *ht/k*
C	vane chord length = 531 mm
d	film cooling hole diameter = 4.2 mm
DR	coolant to mainstream density ratio, ρ_c/ρ_∞
h	heat transfer coefficient (W/m2-K)
I	momentum flux ratio, $(\rho c U c^2) / (\rho \infty U \infty^2)$
k	thermal conductivity (W/m-K)
M	film cooling blowing ratio, $(\rho c U c)/(\rho \infty U \infty)$
Re	Reynolds number
s	streamwise surface distance from stagnation
SH	showerhead holes
t	thickness of vane wall = 12.7 mm
t	trench depth or TBC thickness = 2.5 mm
T	temperature
Tu	turbulence intensity
U	flow velocity
x	streamwise distance
y	wall normal distance
z	spanwise distance

Greek

η	adiabatic effectiveness, $(T_\infty - T_{aw})/(T_\infty - T_{c,\ hole\ exit})$
ϕ	overall effectiveness, $(T_\infty - T_v)/(T_\infty - T_{c,\ vane\ inlet})$
τ	external effectiveness, $(T_\infty - T_{TBC})/(T_\infty - T_{c,\ vane\ inlet})$
θ	gas temperature, $(T_\infty - T_{probe})/(T_\infty - T_{c,\ hole\ exit})$

Subscripts

aw	adiabatic vane wall

c	internal coolant
IP	location of the impingement plate
PS	pressure side holes
SH	showerhead holes
TBC	thermal barrier coating
v	vane wall
w	conducting vane wall
$\bar{}$	laterally averaged

Chapter 1: Introduction

1.1. Gas Turbine Power and the Need for Higher Efficiency

The demand for natural gas for electricity generation in the US has been steadily increasing since the mid-1980s and at an even greater rate since the early-2000s. Simultaneously, the use of coal for electricity generation has been decreasing since the early-2000s. Figure 1.1 breaks down electricity generation by the major contributors in the US from 1980 to 2013. Coal led all other sources in electricity production from 1980 to 2013, yet the use of coal is decreasing from year to year while the use of natural gas is increasing to fill the gap. Energy production, which includes mechanical and electrical power, in the US tells a similar story. In 2010, natural gas passed coal as the largest contributor of energy produced in the US (United States, 2012).

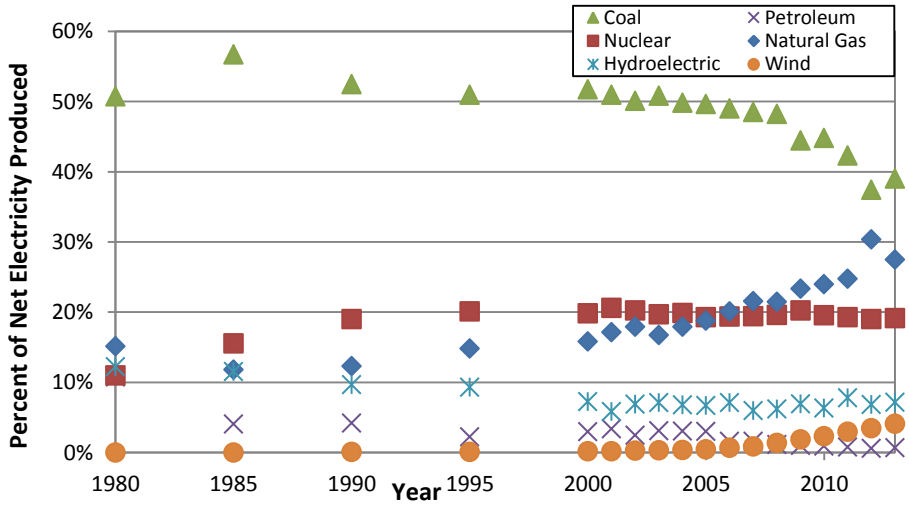

Figure 1.1: Net electricity generated in the US by source percentage contribution (United States, 2013)

Additional sources confirm the rise in demand for natural gas for energy production. Patrylak et al. (2013) estimated that natural gas electricity consumption will

increase to 56% of the market share by 2038, while coal electricity consumption will decrease to 21% by 2038. Furthermore, Patrylak et al. predicts the total demand on power in the US will increase by ~1% a year through 2038, yielding a total increase in the US energy demand of 30% over the next 25 years (Patrylak, et al., 2013). The increasing use of natural gas for power generation coupled with the increasing demand for power provide a strong indication that gas turbines will be an increasing part of our power generation system. Therefore, gas turbines should and will remain a focus of the research community, targeting efficiency and durability.

Gas turbines operate on the thermodynamic cycle called the Brayton cycle which is an internal combustion, constant pressure heat cycle. A simple schematic shows the four processes of a gas turbine cycle in Figure 1.2(a), and Figure 1.2(b) and (c) give the pressure-specific volume and temperature-specific entropy diagrams of the Brayton cycle respectively. Process 1-2 is isentropic compression of the working fluid (compressor stages); process 2-3 is constant pressure heat addition (combustion); process 3-4 is isentropic expansion (turbine stages); process 4-1 is constant pressure heat rejection (exhaust). The Brayton cycle is conventionally studied as a closed cycle where the working fluid is reused each cycle; however, in reality gas turbines run as an open system and the process from 4-1 is exhausting the working fluid to atmosphere.

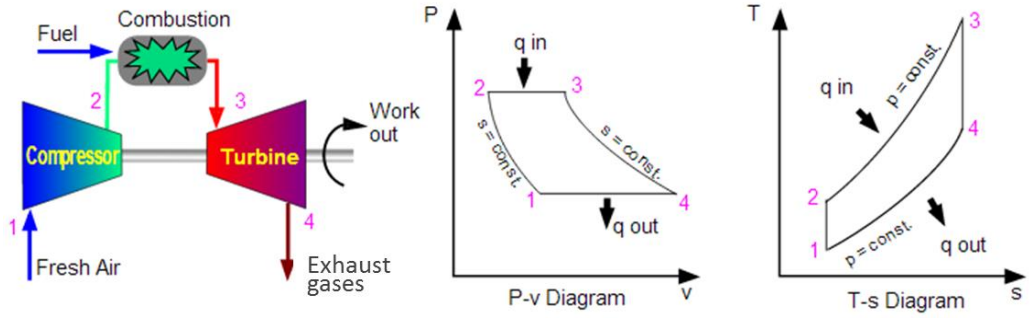

Figure 1.2: (a) Schematic of a gas turbine engine; (b) pressure-volume diagram of the Brayton cycle; (c) temperature-entropy diagram of the Brayton cycle (Brayton Cycle Laboratory)

The net work produced by a gas turbine is the energy produced by the turbine minus the energy required by the compressor. Dividing the net work by the energy added in process 3-2 from combustion gives the thermal efficiency of the Brayton cycle. A series of thermodynamic relations reduces the equation for thermal efficiency to (Schmidt, et al., 2006):

$$\eta = 1 - \frac{T_4}{T_3} \tag{1.1}$$

assuming the working fluid is an ideal gas and isentropic compression and expansion processes. Equation (1.1) makes it apparent that increasing T_3 will increase the thermal efficiency of the gas turbine. However, the T_3, or the turbine inlet temperature, is limited by the material properties of the turbine components. Hot engine temperatures decrease the durability of engine components, so research advances in gas turbine materials and cooling schemes have allowed for both increased durability and efficiency. Figure 1.3 emphasizes the benefit of these advances because increasing the turbine inlet temperature over the last 40 years is coupled with increasing combined cycle turbine efficiencies. From the early 1970s to 2000, the firing temperature, also referred to as the turbine inlet temperature, has increased over 400°C (~40%) yielding an increase in combined cycle efficiency over 10%. The combined cycle efficiency refers to the gas turbine being

coupled with a heat recovery system to increase the system efficiency by making use of the waste heat produced by the gas turbine. Advances in cycle efficiencies over the last 70 years are shown in Figure 1.4 separated by combined and simple cycles. The combined cycle efficiency growth is a function of more parameters than the turbine inlet temperature, so examining the growth in the simple gas turbine cycle efficiency emphasizes the value in increasing the turbine inlet temperature. Therefore, to continue increasing the turbine inlet temperature there need to be continuous advances in turbine component cooling.

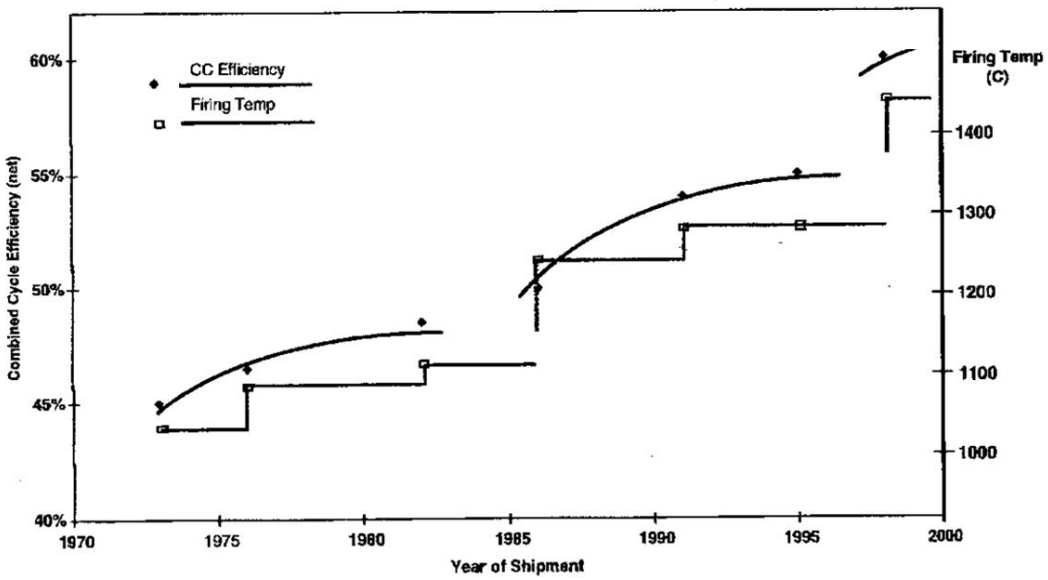

Figure 1.3: The evolution of cycle efficiencies for gas turbines over the last 60 years (Unger, et al., 1998)

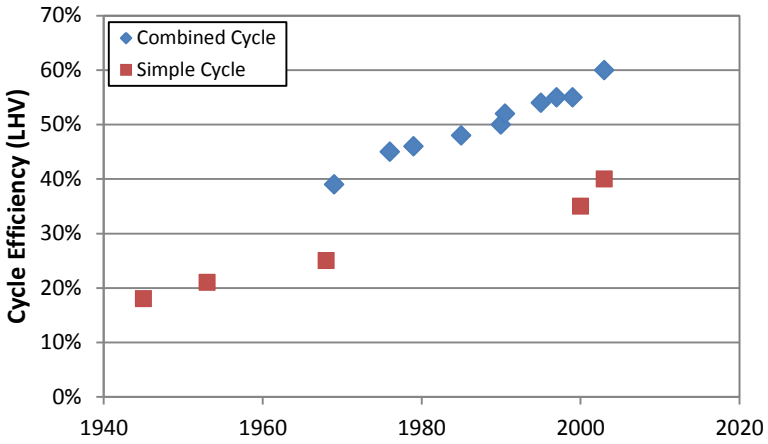

Figure 1.4: Simple and combine cycle efficiencies have increased steadily for 60 years (Unger, et al., 1998)

Three main cooling techniques dominate the thermal protection schemes for turbine blades and vanes: internal convection cooling, external film cooling and thermal barrier coatings (TBCs). The terms blade and vane are used interchangeably in this thesis. Internal convection cooling involves the use of rib turbulators, pin fins, and impingement plate cooling schemes to increase the internal (inside the vane) heat transfer coefficient to cool the vane metal temperature. External film cooling ejects cold gases through holes on the vane surface to coat the vane in a protective film. Thermal barrier coatings are ceramic materials with low thermal conductivities to insulate the vane surface from the hot mainstream gases. These three techniques are pictured in Figure 1.5. The coolant air is pulled from the compressor stages of the gas turbine before the combustor, channeled into the vane to be used for internal cooling, Figure 1.5(a), then exhausted through film cooling holes on the vane surface, Figure 1.5(b). TBCs shown in Figure 1.5(c), have up to 8 times the thermal resistance of turbine vane walls, providing significant insulation against the hot mainstream gases (Bunker, 2009) (Feurstein, et al., 2008) (Special Metals Corporation, 2004).

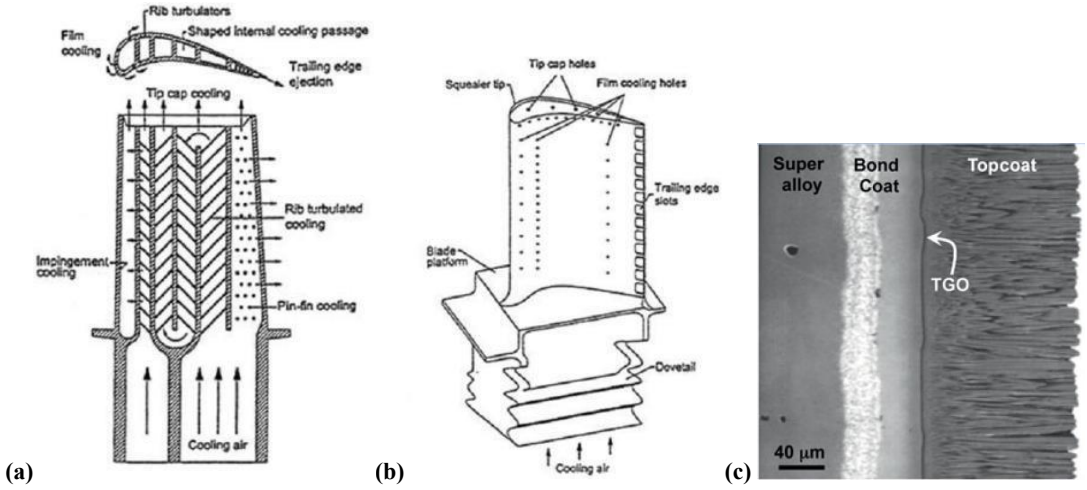

Figure 1.5: (a) Internal and (b) external cooling schemes (Han, et al., 2000) and (c) TBC coating (Clarke, et al., 2012) for a turbine vane

This study focuses on the combined effects of the thermally insulating properties of TBC, film cooling and internal convective cooling on the vane metal temperature by varying the TBC thickness and film cooling geometry. The conjugate effects of internal cooling and film cooling were investigated further with 2D thermal field measurements above adiabatic and conducting turbine vane models. These measurements allowed for a deeper understanding of how a thermally conducting wall impacted the thermal profile of a film cooling jet.

1.2. FILM COOLING BACKGROUND

1.2.1. Use of the adiabatic wall temperature

To simplify the research process internal convective cooling and external film cooling are, in general, studied separately. Film cooling research has adopted a standard of measuring the surface temperature of an adiabatic wall with film cooling to quantify

the cooling effectiveness of varying hole geometries and coolant mass flow rates. The goal of film cooling is to reduce the heat flux through the vane wall:

$$q_o = h_o(T_w - T_\infty) \tag{1.2}$$

where the subscript "o" indicates without film cooling, "*w*" indicates a measurement at the wall, and "∞" indicates a measurement of the mainstream or hot gases. The driving temperature for heat transfer is the difference between the mainstream gas and the wall temperature. The goal of film cooling is to shield the vane surface from the hot mainstream gas and reduce the driving temperature difference for heat transfer. Eckert (1984) derives the equation for heat transfer through the vane wall with film cooling:

$$q_f = h_f(T_w - T_{aw}) \tag{1.3}$$

where the subscript "*f*" indicates with film cooling, and "*aw*" indicates the adiabatic wall temperature. Eckert's analysis also assumes that the energy equation can be solved by a superposition of solutions: one for an adiabatic wall and one for an internally cooled only vane, and the result is Equation (1.3). Eckert's analysis shows that now the adiabatic wall temperature above a film cooled surface is now the driving temperature not the hot mainstream gas, and thus the net heat flux through the conducting vane surface is lowered. This model assumes the temperature of the adiabatic wall with film cooling gives a good indication of the temperature of the bulk flow above the vane wall that will dominate the heat transfer, and this assumption was investigated further in this thesis. In addition, film cooling flow changes the heat transfer coefficient on the turbine vane surface making it important to identify a new heat transfer coefficient h_f. A consequence of the superposition analysis is the assumption that fluid properties are constant across a range of temperatures, and thus assumes the thermal properties of the turbine vane will

have minimal effects on the coolant flow (Eckert, 1984). If true, this analysis provides a very elegant and simplistic method by which to study film cooling in which one is able to completely separate studying film cooling and internal cooling. The adiabatic wall temperature is commonly non-dimensionalized and studied and reported as the adiabatic effectiveness or η:

$$\eta = \frac{T_\infty - T_{aw}}{T_\infty - T_{c,hole\ exit}} \tag{1.4}$$

where $T_{c,\ hole\ exit}$ is the temperature of the coolant gas at the exit of the film cooling holes. Equation (1.4) yields a non-dimensional number between 0 and 1 indicating the effectiveness a particular film cooling configuration. Figure 1.6 shows a typical contour plot of η where the effectiveness is high near the exit of the hole and decays downstream. Note that the spanwise (z-axis) and streamwise (x-axis) directions are non-dimensionalized in terms of coolant hole diameter, *d*.

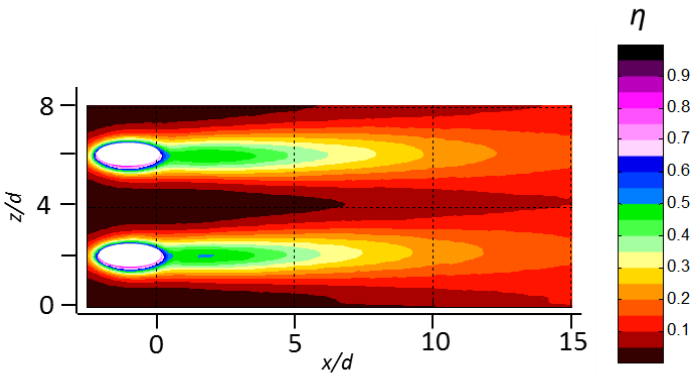

Figure 1.6: Contour plot of adiabatic effectiveness, η

Contour plots of η are great for evaluating the isolated effects of film cooling. However, there is significant interest in the conjugate cooling effects of film cooling, internal convection, and TBC. Additionally, an adiabatic vane model does not allow for the insulating properties of TBC to be studied. Therefore, experimentalists developed a

method by which to model the thermal properties of an engine vane by matching the Biot number of the test vane to an actual engine vane, termed the "matched Biot number method".

1.2.2. Matched Biot Number Method

Similar to the definition of adiabatic effectiveness, engine companies and researchers have defined a non-dimensional "metal" or actual turbine vane surface temperature termed overall effectiveness or ϕ (Bogard, et al.):

$$\phi = \frac{T_\infty - T_w}{T_\infty - T_{c,vane\ inlet}} \tag{1.5}$$

where T_c is the temperature of the coolant as it enters the turbine vane, thus taking into account the internal convective cooling and film cooling. It is called overall effectiveness because it gives an "overall" picture of the turbine cooling, including both internal and film cooling effects. For a turbine vane with TBC, ϕ is still the surface temperature of the vane metal, and it is therefore measured at the interface between the TBC and vane metal surface and a third parameter is defined as the external effectiveness or τ for surface of the TBC:

$$\tau = \frac{T_\infty - T_{TBC}}{T_\infty - T_{c,vane\ inlet}} \tag{1.6}$$

where T_{TBC} is the surface temperature of the TBC. The overall effectiveness is truly representative of the turbine vane temperature and thus essential in evaluating the cooling effectiveness of a turbine vane. Overall effectiveness, ϕ, gives a more complete representation of the turbine vane temperature than adiabatic effectiveness for a vane because it includes the conjugate cooling effects of internal cooling and TBC as well as any impact the internal cooling or TBC may have on the film cooling effectiveness.

Therefore, the overall effectiveness of a thermally scaled turbine vane is exactly representative of the overall effectiveness of a true engine component, and this can be immensely helpful in finding hot spots on turbine vanes and evaluating cooling configurations experimentally. Figure 1.7 provides images of the measurement locations and experimental techniques for measuring η, ϕ, and τ. Figure 1.7 pictures the adiabatic and conducting walls, as well as the impact of TBC on the conducting wall.

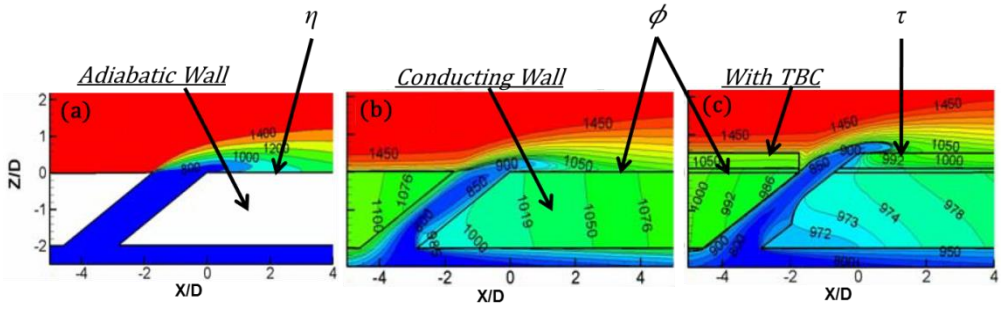

Figure 1.7: Location of measured effectiveness values, (a) adiabatic, (b) overall, and (c) external effectiveness (Na, et al., 2007)

It is difficult, if not impossible, to replicate engine conditions in a laboratory, so experimentalist often taken advantage of non-dimensional scaling parameters to simulate engine conditions. In order to develop an experimental approach to measure ϕ under laboratory conditions consider a 1-D heat transfer analysis through the vane wall:

$$q_{vane} = \frac{T_\infty - T_{c,internal\ vane}}{1/h_e + t/k + 1/h_i} = \frac{T_\infty - T_w}{1/h_e} \tag{1.7}$$

where h_e is the external heat transfer coefficient, h_i is the internal heat transfer coefficient, t is the vane thickness and k is the vane wall thermal conductivity (Dees, et al., 2009). Equation (1.7) reduces to give the overall effectiveness without film cooling, ϕ_o, as a function of h_e, h_i, t, and k of the turbine vane:

$$\phi_o = \frac{1}{1 + {h_e t}/{k} + {h_e}/{h_i}} \tag{1.8}$$

where ${h_e t}/{k}$ is the vane Biot number and ${h_e}/{h_i}$ is the ratio of external to internal heat transfer coefficients. Dees et al. used this analysis to create a model vane with similar thermal properties to an actual engine by matching both the Biot number and ratio of heat transfer coefficients. Therefore, the overall effectiveness measurements on a matched Biot number model are representative of overall effectiveness measurements on actual engine vanes. The matched Biot number method has been studied extensively in the experimental works of [(Albert, et al., 2011) (Dyson, et al., 2013) (Dees, et al., 2013)].

Albert et al. and Dyson et al. included the effects of film cooling in their analyses showing that the overall effectiveness can be found using the adiabatic effectiveness as in:

$$\phi = \frac{1 - \chi\eta}{1 + {h_e t}/{k} + {h_e}/{h_i}} + \chi\eta \tag{1.9}$$

where $\chi = \frac{T_\infty - T_{c,hole\ exit}}{T_\infty - T_{c,vane\ inlet}}$ to capture how the coolant warms due to convection inside the turbine vane and convection in the coolant hole, and η is the adiabatic effectiveness (Albert, et al., 2011) (Dyson, et al., 2012). Finally, Equations (1.8) and (1.9) can be combined to form:

$$\phi_o = \phi_o(1 - \chi\eta) + \chi\eta \tag{1.10}$$

The analysis to derive Equation (1.10) relies on the same assumptions as those of Eckert et al. (1984), using the adiabatic wall temperature as the driving temperature for heat transfer through the vane wall. Dees et al. (2013) was able to successfully predict laterally averaged overall effectiveness with film cooling using measurements of overall

effectiveness without film cooling and measurements of adiabatic effectiveness for film cooling jets that were attached to the vane surface. Therefore, it followed that hat the adiabatic wall temperature was a good indication of the driving temperature for heat transfer when the coolant jet was attached to vane surface (Dees, et al., 2013). However, other studies have shown that the adiabatic wall temperature fails to predict the overall effectiveness for both attached and separated jets (Williams, et al., 2012) (Dyson, et al., 2013). Therefore, there is obvious interest in understanding when the adiabatic wall temperature is and is not the driving temperature for heat transfer into the vane wall.

These studies of Dees, Williams and Dyson have been limited to measurements of the vane surface temperature which only gives an indication of the footprint of the jet, and the current study extensively investigated the gas temperature above the film cooled wall to understand how the matched Biot number model affects the film cooling jet temperature profile. Interactions between the coolant jet and the thermal boundary layer as well as the non-zero heat transfer rate through the wall are expected to cause differences between the thermal fields above adiabatic and conducting vane surfaces. The next three sections will discuss previous studies of CFD simulations, thermal fields off the vane surface, and TBC.

1.3. CFD Simulations of Adiabatic and Overall Effectiveness

Turbine engine conditions are very difficult to recreate in a laboratory setting with temperatures over 2000 K and pressures 10-15 times atmospheric pressure, so many experimental measurements are made in low speed scaled up facilities to match Reynolds numbers. The temperature ratio between the mainstream and coolant gases is simulated using cryogenic temperatures as opposed to hot gas conditions. Therefore, there are

obvious advantages to computer simulations that can model realistic engine conditions without assumptions using scaling parameters.

Leylek et al. (1994) used an eddy viscosity model to predict film cooling effectiveness on a flat plate without success. The computational predictions of Leylek et al. consistently over-predicted the centerline effectiveness and failed to predict how the jet spread laterally as it evolved downstream (Leylek, et al., 1994). Harrison et al. (2008) studied a wide range of RANS turbulence models and made comparisons between computational and experimental adiabatic effectiveness and heat transfer coefficients. Harrison et al. made comparisons using lateral averages of adiabatic effectiveness. Their results had varying success with some models accurately predicting the laterally averaged effectiveness for some coolant flow rates while others did not. Harrison et al. also compared the centerline effectiveness of experimental measurements and computational predictions, and the results showed an over-prediction of cooling effectiveness on the centerline Additionally, Harrison et al. compared lateral eta plots at several distances downstream of the film cooling hole exit and found that RANS models, in general, under-predicted the level of lateral spreading compared to experimental measurements (Harrison, et al., 2008).

However, lateral averages of effectiveness hide variations in surface temperature and thus obscure discrepancies in the details of the film cooling flow. Therefore, matching laterally averaged effectiveness between computational and experimental results does not indicate that the computational model is accurately predicting the film cooling flow. Dyson et al. (2012) used RANS models to predict adiabatic and overall effectiveness in the showerhead region of a turbine vane using contour plots and not lateral averages. Their study reported that the RANS model over-predicted adiabatic

effectiveness because of the inability of RANS models to predict jet dispersion. The over-prediction in adiabatic effectiveness yielded an over-prediction of overall effectiveness by the RANS model (Dyson, et al., 2012). The lack of success in film cooling prediction using RANS turbulence models has led to the use of more advanced CFD techniques.

Recently, more advanced CFD techniques have proven to give more accurate predictions of film cooling effectiveness using LES, DES and URANS. Voigt et al. compared velocity field measurements of film cooling jets to computational predictions of RANS, URANS and SAS. This study showed that the unsteady turbulence models gave better predictions of the velocity fields of downstream of the coolant hole exit. The velocity fields of the unsteady models more closely matched the lateral spreading and downstream decay of the film cooling jet velocity profiles. Additionally, in comparing adiabatic effectiveness between unsteady and steady RANS models, Voigt et al. showed that the unsteady model showed greater jet dispersion and quicker decay which would be more representative of experimental film cooling jets. While unsteady models are an improvement over RANS models, they cost of 100 times the processing time (Voigt, et al., 2010). Therefore, engine companies and researchers still use RANS turbulence models to predict both adiabatic and overall effectiveness, and if these models are still to be used, it is essential to understand their successes and flaws.

Dyson et al. compared experimental measurements of both η and ϕ on a scaled up C3X vane model to CFD predictions using a k-ω SST RANS model. The k-ω SST RANS model was used because it has been shown to be the best at predicting jet separation by Matthew et al. (Mathew, et al., 2011).This study was one of the first CFD studies of the conjugate heat transfer effects in a thermally simulated (matched Biot number) turbine vane. This comparison emphasized the results of previous studies showing that the CFD

model over-predicted centerline adiabatic effectiveness, under-predicted lateral spreading and jet dispersion. However, the comparison of contour plots of ϕ between the experimental measurements and computational predictions revealed that lateral conduction within the vane wall can hide the simulation's inability to predict the coolant jet's lateral spreading. This result emphasizes the need to examine the thermal field above the vane wall and not just the footprint of the coolant jet on the vane surface to evaluate CFD predictions of overall effectiveness (Dyson, et al., 2012).

1.4. THERMAL FIELDS

The thermal field measurements in this study provide two important comparisons in film cooling research. The first was to evaluate the impact of the thermal properties of the turbine vane on the film cooling jet profile, and the second was to provide a more complete evaluation of CFD predictions of film cooling to experimental results. Dees et al. measured thermal fields above both adiabatic and thermally conducting vane models with film cooling. For high coolant flow rates where the core of the coolant jet is separated from the vane surface, Dees et al. reported a thermal boundary layer developing underneath the core of the jet and relatively similar temperature profiles for conducting and adiabatic walls near the vane wall for cases where the jet core is attached to the vane surface. Dees et al. also reported that for cases where the coolant jet was attached to the vane surface the adiabatic wall temperature gives a good indication of the driving temperature for heat transfer, yet when the coolant jet was separated, the adiabatic wall temperature is not a good indication of the driving temperature for heat transfer. This conclusion was consistent with the previously discussed predictions of ϕ using η and ϕ_o (Dees, et al., 2013). However, Dees et al. (2011) speculated that some of the observed

differences between the adiabatic and conducting walls were from geometric variations between the adiabatic and conducting vane models leaving questions as to whether the differences in thermal profiles where from geometric variations in vane models or the thermal properties of the vane model (Dees, et al., 2011).

Mathew et al. experimentally measured the thermal profiles of film cooling jets on a thermally simulated (matched Biot number) leading edge model of a turbine vane and compared these measurements to computational predictions from the Realizable κ-ε model and the Shear Stress Transport κ-ω model (κ-ω SST model). Their results showed the Realizable κ-ε model over-predicted the level of coolant jet dispersion observed experimentally, and the Shear Stress Transport κ-ω model under-predicted the turbulence generated by the coolant jet injection into the mainstream flow and thus under-predicted the coolant jet dispersion. This study was limited to one coolant flow rate at two locations on the leading edge model and did not include measurements from an adiabatic model for comparison to the matched Biot number model (Mathew, et al., 2011).

Dyson et al. performed a comprehensive CFD analysis of thermal fields above both thermally conducting and adiabatic vane surfaces using a k-ω SST RANS model. This CFD study reported that in no case is the adiabatic wall temperature the driving temperature for heat transfer. The separated coolant jets interacted with the thermal boundary layer providing some cooling protection, and the attached jets above the adiabatic vane surface were much colder than the jets above the thermally conducting model because the conducting wall had warmed the coolant near the wall (Dyson et al. 2012). However, the open literature lacks a comprehensive experimental analysis of thermal fields off the vane wall focusing on the adiabatic wall temperature as the driving temperature for heat transfer. Therefore, the thermal field measurements in this study

were made on adiabatic and thermally conducting C3X model turbine vanes identical to the computational work of Dyson et al. This allows for comprehensive evaluations of both the adiabatic wall temperature as the driving temperature for heat transfer and the RANS model predictions of the thermal fields from Dyson et al.

The thermal field measurements given in this thesis are reported as θ, or:

$$\theta = \frac{T_\infty - T_{gas,x,y,z}}{T_\infty - T_{hole\ exit}} \tag{1.11}$$

where T_{gas} was the temperature downstream of the coolant jet. The conducting vane model warmed the coolant gas it passed through the coolant hole. Therefore, the temperature at the exit of the coolant hole is used for both matched Biot number and adiabatic vane models to account for warming due to in-hole convection in the coolant hole.

1.5. THERMAL BARRIER COATING

Experimental measurements of the insulating effect of TBCs on overall cooling effectiveness have only recently emerged in the literature as use of the matched Biot number experimental technique has grown. NASA (1980) conducted the first study of TBC on turbine vanes and found that the ceramic coating lowered the vane metal temperature, with improvements in overall effectiveness of 40% with no additionally cooling. However, for lower Reynolds numbers (Re = 0.28x10^5) there were regions of the vane where the increased surface roughness from the TBC tripped the boundary layer, increased the heat transfer coefficient and thus increased the vane metal temperature (Gladden, et al., 1980). The experiments of Gladden et al. did not include the effects of film cooling. Maikell et al. simulated the effects of TBC on a matched Biot number leading edge model with film cooling. They found the external surface temperature of the

TBC was higher, but the metal temperature beneath the TBC was lowered. The presence of TBC also decreased the sensitivity of the metal temperature to the angle of attack of the approach flow (Maikell, et al., 2009).

To further understand the impact of TBC on turbine vane cooling it is important to consider previous research on turbine vane cooling without TBC. In turbine cooling measurements with TBC, deviations from the expected trends of previous studies without TBC are attributed to the presence of the TBC. Nathan et al. showed increases in both adiabatic and overall effectiveness on a leading edge model with increasing coolant flow rate with cylindrical holes (Nathan, et al., 2012). Typically, adiabatic effectiveness drops off for high coolant flow rates because the jets separate from the vane surface, but the leading edge region allows for coolant to build up near the stagnation line. Albert et al. reported the same increases in adiabatic and overall effectiveness in the leading edge region of a full turbine vane model. Additionally, Albert et al. found dramatic increases in overall effectiveness on the pressure side of the vane when trenched cooling holes were used vs. standard cylindrical holes because the trenched holes provided greater levels of adiabatic effectiveness. However, overall effectiveness dramatically improved with film cooling from cylindrical holes vs. no film cooling and internal cooling only (Albert, et al., 2011).

More recently, the works of Davidson et al. and Kistenmacher et al. showed that the insulating properties of TBC dominated over varying film cooling geometries and coolant flow rates. Davidson et al. studied a collection of film cooling hole geometries including cylindrical holes, craters, and trenches. Trench and crater hole geometries are known to provide higher levels of adiabatic effectiveness (Dorrington, et al., 2007); however, with TBC, the overall effectiveness or vane metal temperature was less

sensitive to variations in the film cooling geometry (Davidson, et al., 2012) (Kistenmacher, et al., 2013). Measurements of the TBC surface temperature, τ, showed that some geometries greatly improved the film cooling effectiveness over others, but overall effectiveness only saw slight improvements. In addition, overall effectiveness decreased on a vane surface without TBC when the coolant mass flow rate was increased significantly, but on a vane surface with TBC the overall effectiveness remain largely unchanged. The TBC thickness studied by Davidson et al. Kistenmacher et al. was in the higher region of the spectrum of TBC thickness for actual turbine vanes, so this study examined the overall cooling effectiveness with a thinner TBC because it was unknown if a thinner TBC would continue to dominate the turbine cooling. In addition, a deeper analysis of the impact of TBC and film cooling in the leading edge region of the vane was studied.

1.6. DEPOSITION

Contaminant deposition in gas turbine engines is the result of impurities in the ingested air such as sand or other debris, and ash particles from coal syngas. Figure 1.8 shows the result of volcanic ash particles that entered a gas turbine on high pressure turbine vanes. Contaminant deposition erodes the leading edge, causes the TBC to spall, and plugs film cooling holes. Furthermore, deposition increases the turbulence level near the vane surface which increases the heat transfer coefficient and degrades film cooling performance. Therefore, it is of interest to study and understand the impact of contaminant deposition on turbine vane cooling and more specifically on overall effectiveness.

Figure 1.8: Volcanic ash deposition on gas turbine vane surface (Hamed, et al., 2006)

Albert et al. (2011) experimentally simulated contaminant depositions on a film cooled turbine vane using a wax spray technique. Albert et al. measured adiabatic effectiveness with and without contaminant depositions and found no noticeable degradation in film cooling performance with deposition. Their study found that the surface temperature of the vane significantly impacted the level of deposition that formed on the vane surface. An isothermal (T_w=T_∞) model without film cooling experienced the greatest level of deposition while a matched Biot number model with film cooling and internal cooling showed very small levels of film cooling. Davidson et al. (2012) studied simulated deposition for a turbine vane coated with TBC with various film cooling geometries, and they found that deposition was changed noticeably with film cooling geometry. Additionally, they found that film cooling caused the height of the depositions to double on the external surface of the TBC compared to depositions that formed without film cooling. Depositions decreased film effectiveness for all film cooling geometries except round holes, but overall effectiveness increased with deposition for all

film cooling geometries. Davidson et al. found that the insulating effect of the layer of deposition dominated over the increased heat transfer coefficient from the depositions.

Measurements of pressure loss in the wake of the vane with and without deposition were taken by Erickson et al. (2010) for varying Reynolds numbers and turbulence conditions. For low Reynolds numbers, Erickson et al. found that the deposition tripped the boundary layer and resulted in greater pressure losses especially on the pressure side of the turbine vane. However, with greater levels of inlet turbulence, they found that deposition had less of an influence on the pressure losses.

The work of this thesis focuses on simulated wax deposition on a vane model coated in a thinner TBC compared to the work of Davidson et al. Albert et al showed a significant effect of surface temperature on deposition, and the thinner TBC resulted in a colder vane surface because of reduced insulation. Furthermore, the trench configuration in this study was thinner than the trench of Davidson et al. This study also took measurements of temperature and velocity in the wake of the turbine with and without deposition. This was the first study to characterize the surface temperature and wake profile for the same turbine vane model with and without deposition.

This thesis presents three studies: using experimentally measured thermal fields to evaluate CFD simulations of film cooling and to evaluate the adiabatic wall temperature as the driving temperature for heat transfer; the results of a using different thickness TBCs on turbine vane overall effectiveness with a showerhead and both pressure side round holes and a realistic trench; and the results of simulated contaminant deposition on the overall effectiveness for a thinner TBC and on the wake profile behind the vane.

Chapter 2: Experimental Setup

2.1. TEST SECTION

The experimental measurements for this study were made in a 50 hp closed loop wind tunnel in the Turbulence and Turbine Cooling Research Laboratory (TTCRL) at the University of Texas at Austin. The wind tunnel was coupled with a secondary flow loop powered by a 5 hp blower to provide the coolant for internal convection and film cooling. The wind tunnel primary and secondary flow loops are pictured in Figure 2.1. Turbine inlet temperatures are around 2000 K and turbine coolant temperatures are around 1000 K. It is difficult to match these conditions in the laboratory, so researches focuses on matching the ratio of densities between the coolant and mainstream flow instead of the specific temperatures. The density ratio is defined as:

$$DR = \frac{\rho_c}{\rho_\infty} \tag{2.1}$$

where ρ_c is the density of the coolant, and ρ_∞ is the density of the mainstream gas. Typical gas turbines have density ratios between 1.8 and 2.0. The mainstream flow temperature in the TTCRL was maintained at a steady state temperature of 305 K using water heat exchanger, and the coolant flow loop was maintained at 254 K using a liquid nitrogen (LN2) heat exchanger in the secondary flow loop. This temperature ratio gave a *DR* =1.20±0.05 which is out of the range of a typical gas turbine. However, the work of Ethridge et al. showed how to scale film cooling effectiveness by coupling the coolant mass flow rate and *DR* (Ethridge, et al., 2001). Defining two non-dimensional mass flow rates, the first is blowing ratio:

$$M = \frac{\rho_c U_c}{\rho_\infty U_\infty} \tag{2.2}$$

and the second is momentum flux ratio:

$$I = \frac{\rho_c {U_c}^2}{\rho_\infty {U_\infty}^2} \tag{2.3}$$

where U_c and U_∞ are the velocities of the coolant and mainstream respectively. The results of Ethridge et al. showed that blowing ratios, $M < 0.7$, adiabatic effectiveness scaled well with blowing ratio, and for momentum flux ratios, $I > 0.4$, adiabatic effectiveness scaled well with momentum flux ratio regardless of *DR*. Figure 2.1 shows orifice flow meters in the secondary coolant flow loop that measured the mass flow rate and flow control valves to adjust M and I. The mainstream flow loop had a series of desiccant packs that pulled humidity from the mainstream air to prevent frost from building up at the cryogenic coolant temperatures.

The mass flow rate through an orifice plate was found using the pressure drop across the plate:

$$\dot{m}_{coolant} = \frac{\rho C_d A}{\sqrt{1-\beta^4}} \sqrt{\frac{2\Delta p}{\rho}} \tag{2.4}$$

where ρ is the coolant density, C_d is the discharge coefficient of the orifice, A is the area of the orifice, β is the ratio of orifice to pipe diameters, and Δp is the pressure drop across the orifice plate. The discharge coefficient, C_d, was found experimentally using a laminar flow element in line with the orifice plates. These measurements produced a calibration for C_d in terms of the pipe Reynolds number that was used in the experiments. The orifice plates were sized such that they were operated in a region of the calibration where C_d is mostly constant. The uncertainty in the coolant flow rate was largely dependent on the uncertainty in the pressure transducer used to measure the pressure drop, the calibration for C_d, and the geometric measurements of the coolant pipe and orifice plate. There were

three pressure transducers used in this thesis (one for the fore passage or u-bend in, one for the u-bend out, one for the aft or radial passage), and they were Omega PX653 high accuracy differential pressure transducer. They each were calibrated against a micro-manometer and had a calibration bias uncertainty of ±1.5 *Pa*.

The wind tunnel velocity was measured using a Pitot-static probe upstream of the test section containing the test vane. The differential pressure for the Pitot-static probe measurement was made using an Omega PX2650, and after calibration against the micro-manometer, the transducer had a uncertainty of ±1 *Pa*. This translated into an uncertainty of ±0.1 *m/s.* This uncertainty, along with the uncertainty in the coolant flow rate measurement gave an uncertainty of $M = \pm 0.25$ for the UTSR vane, and a range from $M =$ 0.015 to 0.05 for the PW vane. There was greater uncertainty for the blowing ratio on the UTSR vane because the u-bend had an inflow and an outflow to measure, as opposed to just an inflow as was the case for the PW vane, and the combined uncertainty from the two pressure transducers required to measure the difference between the in and out flow was higher than the uncertainty for one pressure transducer. The vane nomenclature is explained in Section 2.2.

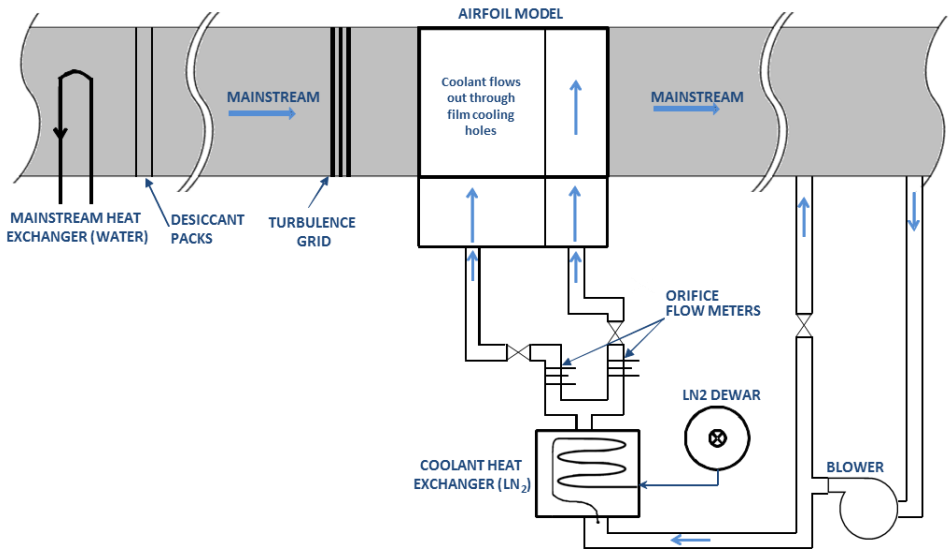

Figure 2.1: Schematic of wind tunnel and secondary coolant flow loop

The turbine vane model tested in the wind tunnel was an 11.6x scale model of the C3X vane which is a first stage vane from a helicopter engine (Ames, 1998). A birds-eye-view of the test section is given in Figure 2.2. The test section had a simulated three vane linear cascade with adjustable walls. The adjustable walls allowed for the pressure distribution on the vane surface to be adjusted to match the vane pressure distribution of a CFD simulation of an infinite cascade. Figure 2.3 shows a plot of the pressure distribution compared to the CFD prediction across the vane surface in terms of the chord length, *C*.

The turbulence grid, 0.5 meters upstream of the vane cascade provided isotropic turbulence levels of Tu = 20% ± 1% across the cascade pitch 0.14 meters (or 0.27 x/C) upstream of the vane cascade (Pichon, 2009). Table 2.1 gives a complete set of geometric and flow parameters for the test section.

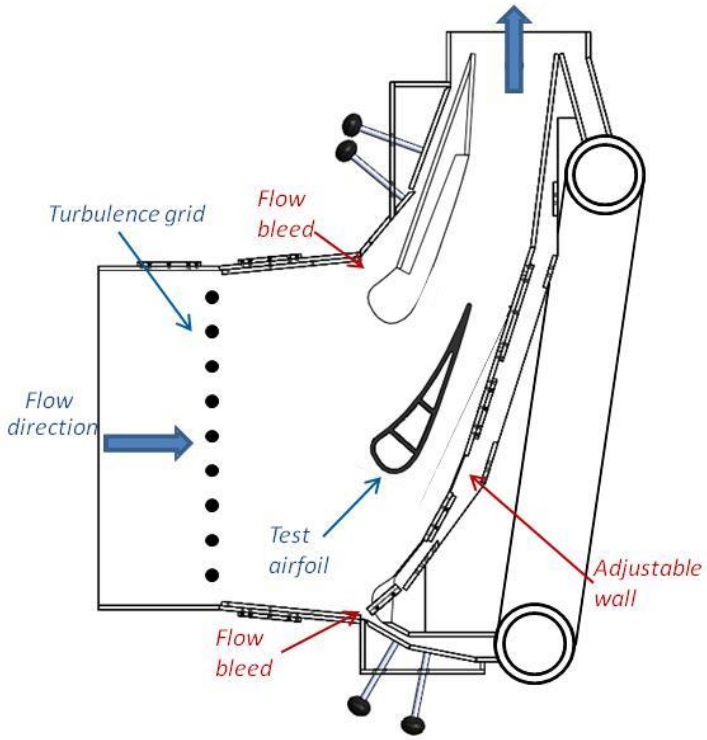

Figure 2.2: Schematic of the test section

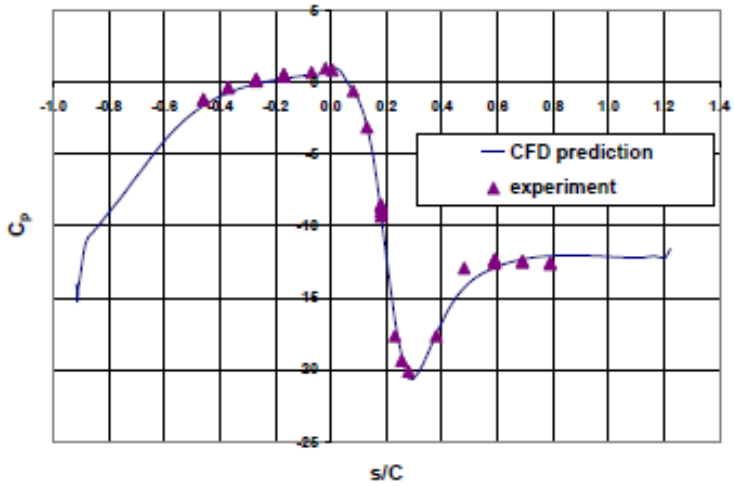

Figure 2.3: Vane pressure distribution in comparison to CFD prediction (Dees, et al., 2009)

Table 2.1: Test section flow and geometric parameters

Parameter	Value	Units
Chord Length (C)	531	mm
Vane Span (H)	549	mm
Vane Pitch (P)	457	mm
Turning Angle	72	degrees
Mainstream Velocity (U_∞)	5.8 ± 0.05	m/s
Mainstream Temperature (T_∞)	305 ± 0.5	K
Density Ratio (DR)	1.2 ± 0.01	-
Chord Exit Reynolds Number	7×10^5	-

2.2. VANE MODELS

Three vane models were used in this study and are discussed in the following section: two matched Biot number models, the conductng PW vane model and UTSR vane model, and one adiabatic model, the adiabatic PW vane model.

A typical gas turbine engine vane has a surface averaged external heat transfer coefficient of h_e = 5850 W/m^2K (Bunker, 2009), so a reasonable range for h_e is 1000-10000 W/m^2K. Bunker also gives a typical vane wall thickness of t = 2 mm, and Specialty Metals gives the thermal conductivity for Nickel Based super-alloys typically found in gas turbine engines to be k = 20 $W/m\text{-}K$ (Special Metals Corporation, 2004). Thus, the range of Biot numbers a typical gas turbine vane is expected to have is $0.1 < Bi < 1.0$. The matched Biot number models were constructed of DuPont Corian® which has a thermal conductivity of 1.0 W/mK. Dees et al. measured the external heat transfer coefficient on the scaled up C3X vane model and reported that $35 < h_e < 90$ W/m^2K (Dees, et al., 2012). The thickness of the model vane wall was t = 12.7 mm. Thus, the model C3X vane in this study had a Biot number: $0.5 < Bi < 1.2$.

The other important thermal scaling parameter in model vane design is the ratio of internal to external heat transfer coefficients. The two matched Biot number models in this study used different methods to match the ratio of internal to external heat transfer coefficients.

2.2.1. Conducting PW Vane Model

The first had a proprietary internal impingement plate designed with consultation from industry partners to match the ratio of internal and external heat transfer coefficients. For the remainder of this thesis, this vane will be referred to as the "conducting PW vane". Figure 2.4 shows a schematic of the PW vane and its internal impingement plate cooling design, and pictured in both Figure 2.1 and Figure 2.4, the PW vane had fore and aft passages fed by separate cooling lines. The unique cooling lines allowed for varying levels of coolant mass flow rate that flow out of the fore and aft passages. For this study only one row of film cooling holes was tested on the suction side of the PW vane model. The thermal field measurements were made at 0, 5, and 10 hole diameters downstream of this row of film cooling holes.

2.2.2. Adiabatic PW Vane

To be certain any variations in the thermal field measurements were solely a result of the thermal properties of the vane, geometric consistency was maintained between the adiabatic and conducting vane models, so the impingement plate was also included in the adiabatic PW vane model.

Ideally, the model used for adiabatic effectiveness measurements would be perfectly adiabatic, but this is impossible experimentally. Thus, the adiabatic PW vane

model was constructed of polyurethane foam with a low thermal conductivity, k = 0.043 *W/m-K*. The impact of and corrections for conduction through the vane wall and lateral conduction within the vane wall will be discussed in future sections (Section 3.3.2).

The PW vane models had a single row of holes on the suction side of the vane at s/C = 0.512 (spanwise distance normalized by chord length). The film cooling holes had surface angle, α = 25°, a diameter, d = 6.35 *mm*, and a spanwise spacing of p/d = 4. The location of these film cooling holes is depicted in Figure 2.4.

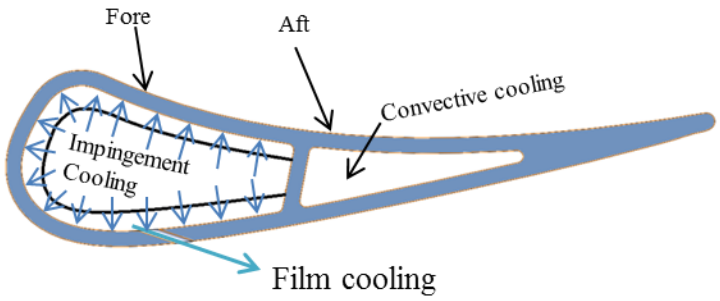

Figure 2.4: Schematic of internal cooling geometry for the PW vane

2.2.3. UTSR Vane

The third model vane tested in this study had a different internal cooling geometry consisting of a U-bend channel pictured in Figure 2.5. This vane model will be referred to as the "UTSR vane" for the remainder of this thesis. The UTSR vane was constructed of the same DuPont Corian® as that of the conducting PW vane. The U-bend channel was designed to match the ratio of internal to external heat transfer coefficients using the analysis shown by Albert et al. (2011). This analysis shows that, using Nusselt number correlations, the heat transfer coefficient ratio was matched when both flow and geometric parameters were matched. Albert's analysis is summed in Equation (2.5):

$$\frac{h_e}{h_i} = \frac{\left(\frac{Nu_x k}{x}\right)_e}{\left(\frac{Nu_{Dh} k}{D_h}\right)_i} = \frac{\left(\frac{C_1 Re_x^a Pr^b k}{x}\right)_e}{\left(\frac{C_2 Re_{Dh}^m Pr^n k}{D_h}\right)_i} \tag{2.5}$$

Equation (2.5) shows that matching external and internal Reynolds numbers (Re_x/Re_{Dh}), the ratio of chord length (the length scale, x) to internal passage hydraulic diameter (D_h), external geometry (C_1), internal geometry (C_2), and assuming the Prandlt number does not vary significantly with temperature, only matching the ratio of thermal conductivities of the mainstream and coolant gases is needed to match the ratio of external to internal heat transfer coefficients (Albert, et al., 2011). However, Albert also showed that ratio of thermal conductivities when T_∞ = 305 K and T_c = 220 K has a 40% deviation from the ratio at engine conditions. Albert furthered the analysis to show that this discrepancy caused a maximum error in ϕ of 0.04. However, it is important to note that the bulk of the data presented in this study is presented in comparison to data from a similar matched Biot number model, so the error in ϕ, which is a bias error, can largely be ignored.

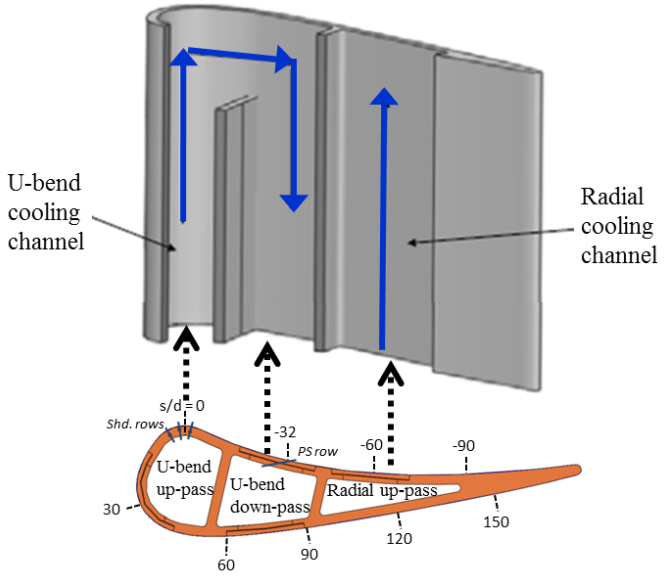

Figure 2.5: Schematic of internal cooling geometry for the UTSR vane

A comprehensive analysis of the ratio of TBC to vane wall thermal conductivity and thickness in actual turbine engines was conducted in order to select a material with an appropriate thickness and thermal conductivity. Table 2.2 uses the studies of Bunker, Clarke, et al., Feurstein, et al., and Soechting to give actual engine thermal conductivities and thicknesses. The previous work of Davidson et al. (2012) used a cork that was in the range the appropriate range of thermal conductivity and thickness, and a major thrust of this study was to use thinner cork to study a thinner region of the range of TBC thicknesses. The cork used in this study fell into the appropriate ranges of thermal conductivity and thickness. However, in studying the thinner cork, it was discovered the thermal conductivities between the two thicknesses of cork were different. It therefore became convenient to match both the ratios of the thickness and the thermal conductivity of TBC and vane wall conditions by using the ratio of thermal resistances, where:

$$R_{TBC} = \frac{t_{TBC}}{k_{TBC}}, \qquad R_w = \frac{t_w}{k_w} \tag{2.6}$$

The analysis showed that a typical ratio of TBC to vane wall thermal resistance ranges from 0.56 to 8.26. The work of Davidson, et al. and Kistenmacher, et al. had a TBC to vane wall ratio of thermal resistance of 3.78. The work of this study desired to reduce the thermal resistance of the TBC by 33%. All of this analysis is outlined in Table 2.2 for both the previous model vane of Davidson, et al. and the current model vane for this study. The UTSR vane was coated in cork of thickness, t_{TBC} = 2.5 *mm*, and k_{TBC} = 0.08 *W/m-K* giving a thermal resistance of R_{TBC} = 0.032 m^2*-K/W*. The measurement technique for finding the thermal conductivity of the cork will be discussed in Section 2.4 Thermal Conductivity Measurement Techniques.

Table 2.2: UTSR vane and TBC thermal properties (Bunker, 2009) (Clarke, et al., 2012) (Feurstein, et al., 2008) Invalid source specified. **(Davidson, et al., 2012) (Dees, et al., 2012)**

Parameter	Real Vane	Current Model Vane	Previous Model Vane	Units
Vane Thickness	1.5 - 3.0	12.7	12.7	mm
TBC Thickness	0.1 - 0.7	2.5	4.4	mm
Vane Conductivity	20 - 25	1.0	1.0	W/m-K
TBC Conductivity	0.8 – 1.7	0.080	0.092	W/m-K
Heat Transfer Coeff.	1000 – 10000	35 - 90	35 - 90	W/m^2-K
Vane Thermal Resistance	0.00006 – 0.00015	0.0127	0.0127	m^2-K/W
TBC Thermal Resistance	0.00008-0.00050	0.032	0.048	m^2-K/W
TBC/Vane Thermal Resistance	0.56 – 8.26	2.52	3.78	-
Vane Biot	0.1 – 1.0	0.5 – 1.2	0.5 – 1.2	-
TBC Thickness/ Hole diameter (t/d)		0.6	1.0	-

The UTSR vane had two separate film cooling configurations, one with and one without a showerhead of film cooling holes on the leading edge of the vane model. Both configurations had a single row of film cooling holes on the pressure side of the vane as indicated in Figure 2.5, at s/C = -0.25 or s/d = -32. This row of 24 cylindrical holes on the pressure side had a diameter, d = 4.2 *mm*, surface angle, α = 30°, and spanwise spacing, p/d = 3. The showerhead on the leading edge consisted of 3 rows of 18 holes with diameter, d = 4.2 *mm*, surface angle, α = 25°, and spanwise spacing, p/d = 5.6.

The pressure side cylindrical holes were, for some experiments, embedded in the TBC to create realistic configurations with and without a trench, analogous to that of Kistenmacher, et al. (Kistenmacher, et al., 2013). Figure 2.6 illustrates the cylindrical

holes on the vane surface with and without the realistic trench cut into the TBC. The trench configuration is described as realistic because manufacturing tolerances were considered in its design. Ideally the trench wall would begin immediately at the edge of the film cooling holes, but that requires unrealistic machining abilities.

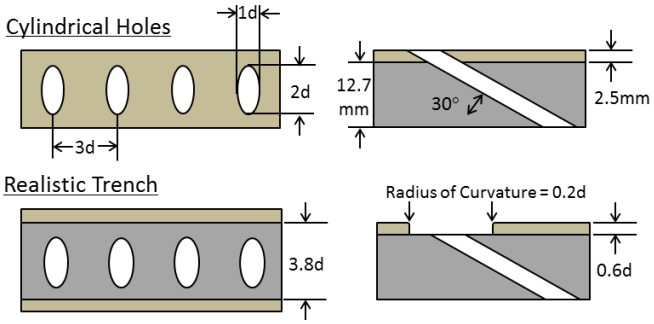

Figure 2.6: Schematic of the pressure side film cooling holes on the UTSR vane

2.3. MICRO-THERMOCOUPLES, TRAVERSE SYSTEM, THERMOCOUPLES AND IR THERMOGRAPHY

The thermal field measurements were made using a micro-thermocouple probe traversed in the plane normal to the film cooling jet flow. The micro-thermocouple probe was an Omega CHCO-002 thermocouple with 2 *mil* (0.05 *mm*) thick wire. The very thin wire was used to reduce conduction effects on the temperature measurement because of the expected steep temperature gradients within the film cooling jet. To further reduce conduction errors due to the temperature gradients in the wall normal direction, the probe was oriented roughly parallel to the vane surface, as pictured in Figure 2.7. In addition, the fine thermocouple bead diameter allowed for tight measurement resolution within the film cooling jet profile. The probe and traverse system are pictured in Figure 2.8(a), and Figure 2.8(b) zooms in on the thermocouple junction. This probe was built specifically for these tests.

The traverse system used a Zaber Technologies T-LSR150B and a T-LSR75B, with 150 *mm* and 75 *mm* of travel respectively, connected normal to each other so the probe could be traveled in two directions. Figure 2.7 illustrates how the micro-TC probe was traversed in relation to the vane and film cooling jet, and Figure 2.8(a) shows how the linear slides connected to the micro-TC probe. To create a particular profile the probe was traversed normal to the vane surface and across a coolant hole pitch. The T-LSR150B traversed the probe in the wall-normal direction, and the T-LSR75B traversed the probe in the spanwise direction.

The T-LSR150B used the vane wall as a reference position ($y/d = 0$) by which to report the position of the probe. The micro-TC probe was zeroed against the vane wall by visual inspection prior to each experiment, and then checked periodically throughout an experiment. The zero position for the probe was by slowly bringing the probe towards the vane surface and observing when the probe wire began to bend, indicating contact between the probe and the vane surface. This was done 5 times in a row, and the location of the wall was recorded each time. Using this set of probe locations, the repeatability of the wall location was repeatable to $\delta y/d = \pm 0.03$. The T-LSR75B used markings on the vane surface as reference positions for measuring the spanwise location, and then checked the spanwise measurements by checking for symmetry in the thermal fields. The spanwise location is reported in the same manner for both the contour plots of effectiveness and the thermal profiles where $z/d = 0$ was between two coolant jets and $z/d = 2$ was the centerline of a coolant jet. The repeatability for the spanwise measurement is $\delta z/d = \pm 0.1$. Zaber Technologies reported the accuracy for both linear slides to be $\pm 15\ \mu m$ which is included in the previously reported uncertainty values (Zaber, 2014).

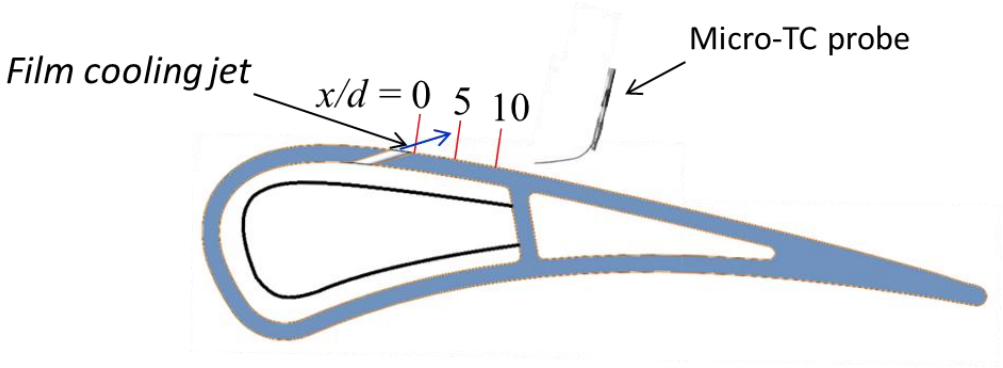

Figure 2.7: Illustration of the micro-TC probe in relation to the model vane

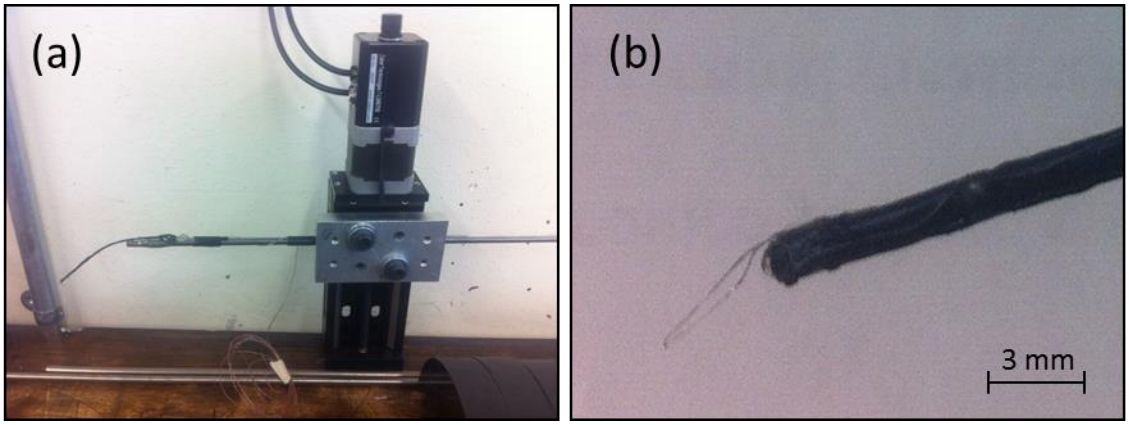

Figure 2.8: Micro-TC probe attached to the Zaber Technologies T-LSR75B linear slide

To simplify the data processing and shorten the experiment run time, temperature data was collected for one half of the film cooling jet then mirrored across the centerline. However, before making the assumption that the film cooling jets were symmetric much testing went in to proving this theory. Initially, contour plots of adiabatic and overall effectiveness for the PW vane were studied to show the symmetric nature of the coolant jets for 4 blowing ratios. Figure 2.9 presents the contour plots of adiabatic and overall effectiveness showing the symmetry of the film cooling jet flow on the surface of the adiabatic and conducting PW vanes. The overall effectiveness contour plots produced by the conducting PW vane did show a similar level of symmetry; however, overall

effectiveness plots showed less lateral variation because of the lateral conduction within the vane wall that does not exist in the adiabatic vane model.

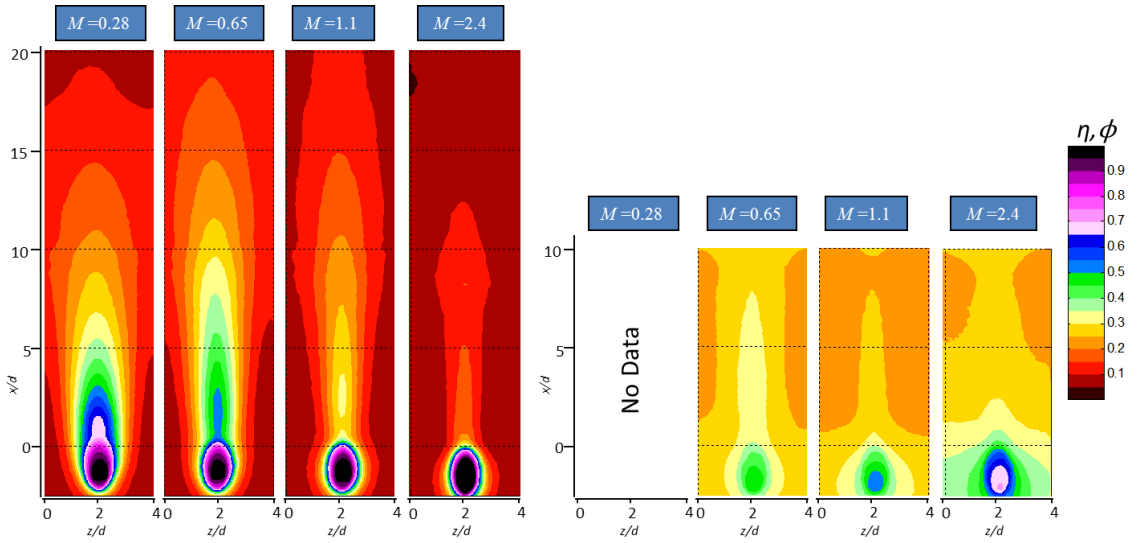

Figure 2.9: Contour plots of adiabatic and overall effectiveness for the PW vane suction side holes for 4 blowing ratios showing symmetry

After finding the contour plots to have symmetric nature, distinct thermal profile lines were compared on either side of the film cooling jet centerline at x/d = 5 and 10 to show that the off-the-vane temperatures were symmetric as well as the on-the-surface temperatures. Collections of these thermal profiles above the conducting and adiabatic PW vane model showing symmetry was seen in Figure 2.10 and Figure 2.11, respectively. For both vane models, thermal profiles taken at equivalent distances from the centerline, on opposite sides of the centerline were equivalent verifying that the coolant jet profiles are symmetric.

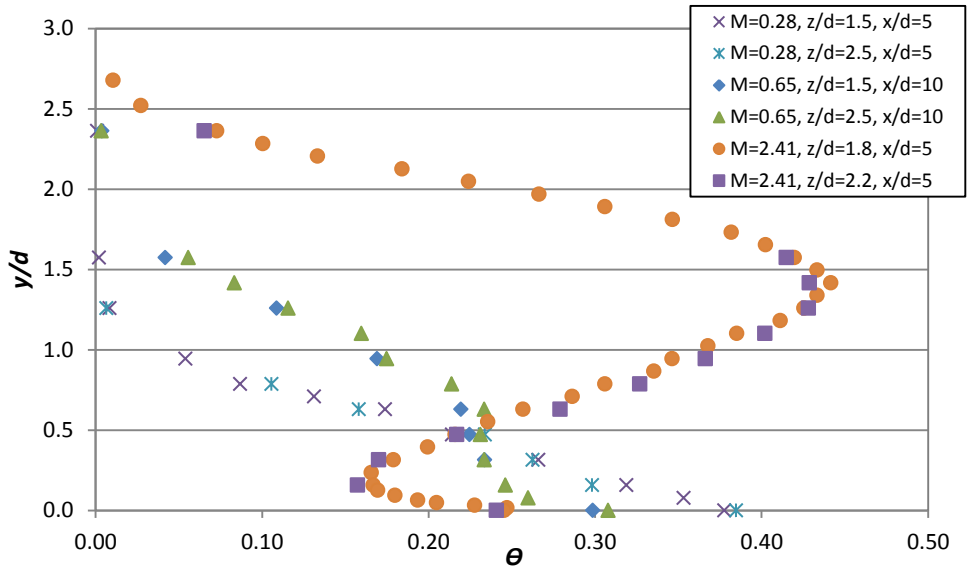

Figure 2.10: Thermal profiles above the conducting PW vane model for different blowing ratios and downstream distances comparing both sides of the film cooling jet thermal profile (*z/d*=2 is the centerline).

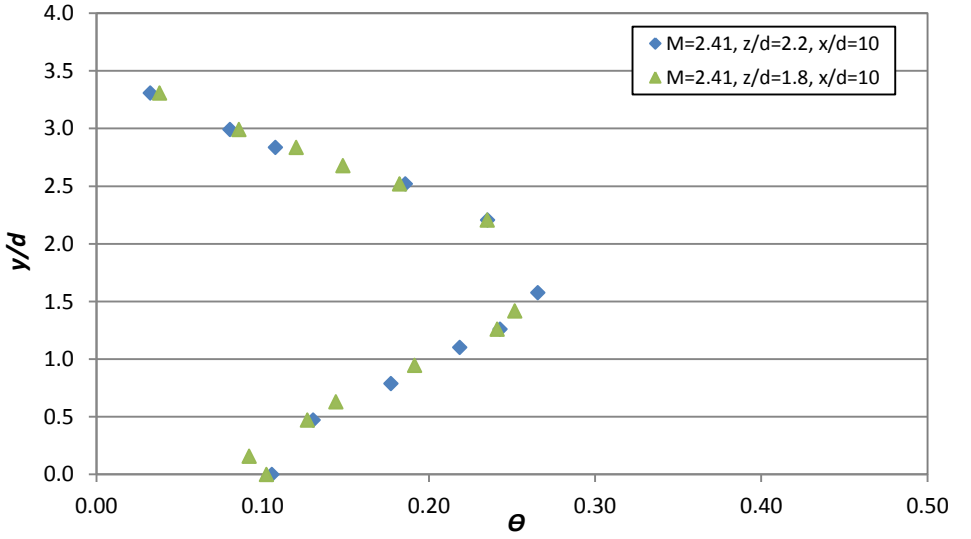

Figure 2.11: Thermal profiles above the adiabatic PW vane model for M=2.41 and x/d=10 comparing both sides of the film cooling jet thermal profile (z/d=2 is the centerline).

The traverse system moved the micro-TC probe in a systematic matrix with a few exceptions. Vertical lines of measurements were made at 10-15 different spanwise positions. Each vertical line of measurements had 10-15 wall-normal positions, and each position was an average of 2-4 data points. The following *z/d* positions were measured

for all cases: z/d = 0, 0.315, 0.63, 0.94, 1.1, 1.26, 1.42, 1.57, 1.73, 1.9, 2, and 2.1 sometimes with additional positions as well. Occasionally, the data or visual inspection would reveal the centerline was inaccurately measured, and the location data was adjusted to the appropriate value. At least one line of measurements was taken for a spanwise position past the jet centerline ($z/d > 2$) to insure the entire jet thermal field was capture using the symmetry assumption. The measurement resolution in the wall normal direction was determined during the experiment and was a function of the thermal gradient in the coolant jet thermal field. The micro-TC probe was moved in increments of 0.16d or 1 *mm*, and if the change in θ, between the original and new probe positions, was greater than 0.05, the probe would traversed back 0.08d. This process was to assure tight measurement resolution for producing the contour plots of θ. The Zaber Technologies traverse system was capable of repeatable movements down to 0.1 *mm* or 0.015d which allowed for a very tight measurement resolution when necessary.

2.3.1. Thermocouple measurement uncertainty

All thermocouples used in this thesis were either surface or bead type E thermocouples. The standard calibration given for the type E thermocouples used in this study gave temperature measurements with an uncertainty of ± 1 K. A tighter uncertainty band was desired for effectiveness measurements, so the thermocouples were calibrated. To insure consistency, they were all calibrated from 253 to 310 K in a glycol bath against a thermistor, and all thermocouple temperature measurements were then accurate to ±0.2 K for a bias uncertainty. The bias uncertainty in temperature measurements propagated into uncertainties for θ and ϕ (for the UTSR vane), $\delta\theta = \delta\phi = 0.006$ because both

measurements were made with thermocouples. Additionally, this bias uncertainty yielded an uncertainty in density ratio of $\delta DR = 0.001$.

2.3.2. Infrared camera measurement uncertainty

Two IR cameras were used in this study, a FLIR Systems ThermaCAM™ P20 and a FLIR T620. The experiments conducted on the UTSR vane used the P20, and the PW vane was tested using the T620. The P20 has a viewing area of 240x260 pixels, giving a spatial resolution on the vane of 1.5 *pixels/mm*. The T620 has a viewing area of 640x480 pixels, giving a spatial resolution on the PW vane of 3.6 *pixels/mm.* Both camera were calibrated against the type E surface thermocouples on the surface of the vane across the range of expected temperature measurements. The standard error of fit for the IR calibration gave an uncertainty of ± 1.3 K for the P20 and ± 0.5 K for the T620. These propagate into bias uncertainties for overall effectiveness on the PW vane of $\delta\phi$ = 0.01, external effectiveness for the UTSR vane of $\delta\tau$ = 0.02, and adiabatic effectiveness for the PW vane of $\delta\eta$ = 0.01.

2.3.3. Precision uncertainties

Additionally, measurement averaging times were considered to lower precision uncertainties from fluctuations in the flow. Two second averages of the mainstream and coolant temperatures were sufficient to reduce the precision uncertainty to be insignificant in comparison to the calibration bias uncertainties for the thermocouples. The one exception was the micro-thermocouple used for the thermal field measurements. The flow field for these measurements was essentially a mixing layer between hot and cold flows, so large fluctuations were seen in the temperature field, and averaging times

were increased to decrease the measurement uncertainty. For this reason, the precision uncertainty in θ, $\delta\theta$ = 0.015, was greater than in the precision uncertainty in ϕ for the UTSR vane, $\delta\phi$ = 0.005. The precision uncertainty in external effectiveness was $\delta\tau$ = 0.005 which was equivalent to that of overall effectiveness because the dominating fluctuating temperatures were the same for both measurements. The precision uncertainty for overall effectiveness measurements on the PW vane was larger than that of the UTSR vane because the PW vane had lower coolant flow rates that were prone to larger variations in temperature. Thus, the precision uncertainty for ϕ on the PW vane was $\delta\phi$ = 0.014.Temperature fluctuations in the flow also had an impact on the density ratio, causing it to fluctuate with bounds of $\delta DR = \pm$ 0.005.

2.4. Thermal Conductivity Measurement Techniques

Cork was used to simulate TBC because it is pliable, and it has a low thermal conductivity relative to the DuPont Corian® material used in the vane construction. Reported values for the thermal conductivity of cork range from 0.04 – 0.07 *W/m-K* (Eni14) (Matias, et al., 1997), so the thermal conductivity of the specific cork used in this study was measured. The thermal conductivity of the cork was measured using two different measurement rigs shown in Figure 2.12.

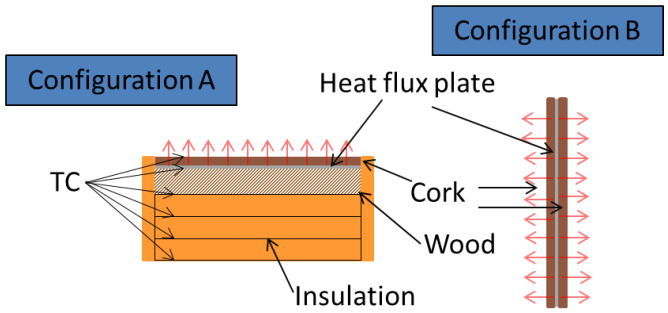

Figure 2.12: Illustrations of both thermal conductivity measurement rigs

Configuration A, shown in Figure 2.12, used a constant heat flux boundary condition on one side of the cork and measured the temperature drop across the cork to determine the thermal conductivity and thermal resistance:

$$R_{cork} = \frac{k_{cork}}{t_{cork}} = \frac{q"_{cork}}{T_{cork,bottom} - T_{cork,top}} \tag{2.7}$$

where t_{cork} is the cork thickness, q''_{cork} is the heat flux going through the cork, and the two temperatures measure the temperature drop across the cork. The heat flux plate was constructed of 0.001" thick stainless steel shim purchased from Trinity Brand Industries. A 6 volt 500 amp Trilectron power supply, model number 3P-500X6, provided constant current into two aluminum bus bars, seen in Figure 2.13, which supplied the current to the heat flux plate. The heat flux coming from the heat flux plate was measured using the voltage drop across the plate and the current running through the plate. The voltage drop was measured directly, and the current was found using the voltage drop across a shunt resistor in series with the heat flux plate. The shunt resistor had a resistance of 3.3E-4 Ohms and was rated to 0.25% accuracy when exposed to up to 100 amps. Typically the output power from the power supply was 20-25 Watts or ~650 W/m^2 across the plate.

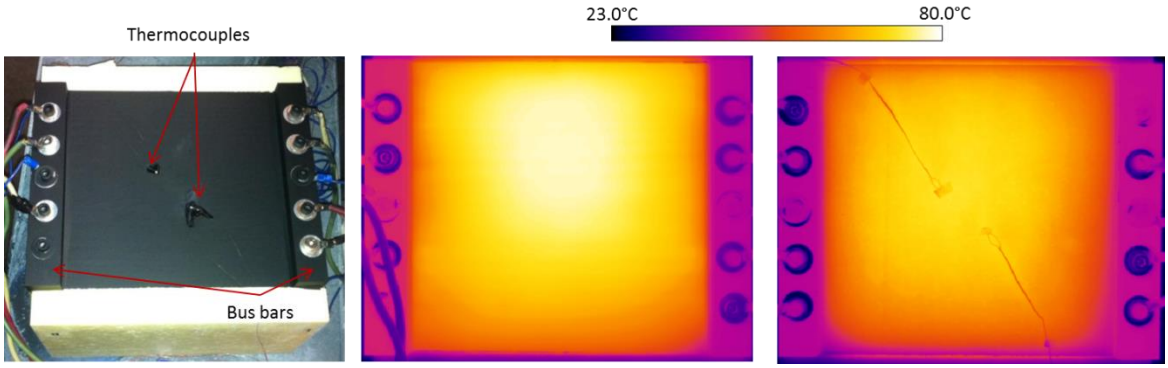

Figure 2.13: Visible and IR images of the heat flux plate (a) heat flux plate with no cork; (b) IR image of heat flux plate with no cork; (c) IR image of heat flux plate coated in cork.

The IR images in Figure 2.13 showed that a fraction of the heat from the heat flux plate flowed backwards into the wood and insulation and out through the sides of the box. Two methods were used to quantify the losses through the back and sides of the measurement rig: an empirical natural convection model and temperature measurements below the wood and inside the insulation. The empirical natural convection model was for a constant heat flux vertical plate from *The Fundamentals of Heat and Mass Transfer* (Incropera, et al., 1990). The IR image, in Figure 2.13(a) gave a temperature distribution over the plate giving Rayleigh and Nusselt numbers for surface of the plate. The Nusselt numbers were then used to find heat transfer coefficients, and then using Newton's law of cooling, the ambient temperature in the room, the plate temperature and the heat transfer coefficient, the total heat flux coming from the plate was found. This analysis gave the total heat flux from the plate that went into and through the cork; the difference between this total heat flux and that of the heat flux plate was assumed to be the losses out of the sides and back of the measurement rig.

To double check the losses found using the previous analysis, the heat flux through the wood and insulation was estimated using the known values for the thermal conductivity of both pine and ASTM C578 polystyrene insulation and the temperature drop across the pine and polystyrene insulation. However, there were also heat flux losses out of the sides of the thermal conductivity measurement rig, and these could not be accurately measured. So, the difference between the total heat flux from the plate and the sum of the heat flux from the natural convection model and the heat flux through the wood and insulation was determined to be the losses through the sides of the rig. Future experiments matched the same temperature conditions at the wood and insulation interfaces to replicate the conditions for when the side losses were measured. A 50%

uncertainty was then assumed for these side heat flux losses. Configuration A yielded a thermal resistance measurement of the cork, R_{cork} = 0.032 ±0.003 $K\text{-}m^2/W$. The 10% uncertainty band on this measurement is predominantly a result of the empirical model used to estimate the side losses.

Configuration B, also shown in Figure 2.12, was designed to minimize the presence of side losses by forcing most of the heat flux to go through the cork layer. By placing cork on either side of the heat flux plate, the heat only had one path, through the cork. In addition, creating both sides to be symmetric, it was assumed that equal amounts of heat flux went through each sheet of cork. Configuration B gave a thermal resistance for the cork, R_{cork} = 0.035 ±0.0017 $K\text{-}m^2/W$ which falls within the uncertainty of the initial measurement, validating both measurements. The uncertainty for Configuration B was roughly half of that of Configuration A because there were no assumptions for heat flux losses. Actually, the uncertainty for Configuration B came from the standard deviation of 20 measurements.

At the end of this report an analysis of the ability to predict the insulating effect of the TBC is given using data from Davidson, et al., and Dees, et al. The thermal resistance of the cork used to simulate TBC by Davidson, et al., was measured for this study using Configuration A, and therefore, the value for thermal resistance used in this study was that of Configuration A.

2.5. DEPOSITION EXPERIMENTAL SETUP

The contaminant deposition was simulated in the same manner as Davidson et al. (2012), using partially molten wax to model deposition on a turbine vane. The wax used in this study was RT31 from Rubitherm Technologies GmbH. Figure 2.14 shows a variac

controlled a heated jacket to pre-heat a reservoir of wax to 325 K, and a second variac heated a compressed air line to pre-heat the sprayer nozzle to 325 K. The Spray Systems Co. 63067-1/8JJAUCO atomizing spray nozzle was activated by a pneumatic control line indicated in Figure 2.14. The hot air and wax lines were insulated in a jacket and carried into the tunnel via one of the turbulence rods in Figure 2.2 and Figure 2.15. The nozzle exit temperature of 325 K was selected in the analysis of Davidson, et al. so that the wax particles would remain partially molten when they impacted the surface of the vane. During the rest of the experiments in this study, the mainstream temperature was 305 K, but for these deposition experiments, the mainstream temperature was adjusted to 301 K, so that the wax was in a partially molten state when in the mainstream.

The same wax spray system used in a similar experimental setup was studied with hot-wire measurements downstream of the wax sprayer in high turbulence conditions by Pichon (2009), and it was found the velocity profile was unchanged by the wax sprayer. The high mainstream turbulence generated by the turbulence grid broke apart the expected wake from the wax sprayer.

Wax was sprayed for 3 minutes with 140 grams of wax released from the wax sprayer. During the spray, the wax deposition levels on the vane surface reached a steady state level beyond which any additional wax sprayed would cause wax already deposited on the vane surface to break off and new wax would then deposit in its place.

First, it was important that the physical flow conditions of true engine deposition matched the flow conditions for the simulated wax deposition. The Stokes number is a non-dimensional parameter indicating the time response of a particle to the flow field around it; for $Stk >> 1$, the particle will not follow the flow field, but for $Stk << 1$ the particle will follow the flow field very closely. The Stokes number is defined as:

$$Stk = \frac{\tau}{l_{char}/U_{char}} = \frac{\rho_p d_p^2 U_{char}}{18 l_{char} \mu_{char}} \tag{2.8}$$

Particles that follow the flow field closely were not expected to impact the vane surface; however, larger particles that break from the flow field were expected to impact the vane surface because their momentum will carry them outside the flow field. The coolant hole diameter and approach velocity to the cascade were used as the characteristic length scale and velocity, 4.2 mm and 5.8 m/s in our model, 1 mm and 250 m/s at engine conditions. Bons et al. (2005) reported coal ash deposition particles on turbine vanes to have a diameter, d_p = 1-10 μm. Using the viscosity of air at engine conditions, the expected Stokes number for coal ash deposition particles in a turbine were *Stk* ~ 21. Then, back calculating the necessary wax particle diameter to match the Stokes number at wind tunnel conditions yielded $d_{wax\ particle}$ ~ 80 μm. SEM images of wax particle deposition from Davidson et al. showed wax particles in this range of diameters (Davidson, et al., 2012). This analysis was presented in more detail in the works of Albert et al. (2011) and Davidson et al. (2012).

The second interaction it was important to match was the sticking interaction between contaminant particles that causes deposition growth. Numerous studies have shown (Walsh et al., 1990, Wenglarz and Fox 1990, and Crosby et al., 2008) a strong dependence of deposition growth rate on temperature, and that peak deposition growth rates occur near the softening temperature of the contaminants. In other words, the sticking probability of a contaminant greatly increased when the particle was partially molten. Therefore, this partially molten state of the fly ash contaminants was the physical condition that was matched with the wax particles. In order to accomplish this, the nozzle exit temperature was set to 325 K and the mainstream temperature was 301 K. The

solidification temperature of the wax was 304 K, so the wax particles would partially cool between the nozzle exit and impacting the vane surface, ensuring the partially molten state necessary to replicate the sticking conditions for fly ash in a turbine engine. This analysis is included in further detail in the works of Albert (2011) and Davidson (2012).

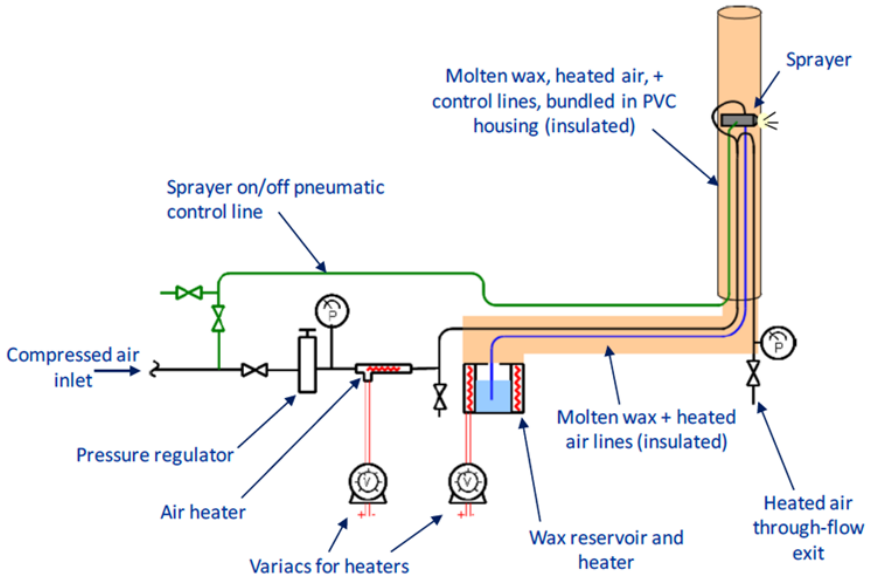

Figure 2.14: Schematic of the wax sprayer system

Figure 2.15: Wax sprayer in the wind tunnel replaces one of the turbulence rods

2.6. SUMMARY OF UNCERTAINTIES

Table 2.3: Collection of uncertainty bands for all measurements

Parameter	Precision uncertainty	Bias uncertainty	Units	Discussed in section
Adiabatic effectiveness (PW vane), $\delta\boldsymbol{\eta}$	-	± 0.01	-	2.3.2
Overall effectiveness (PW vane), $\delta\boldsymbol{\phi}$	± 0.014	± 0.01	-	2.3.3, 2.3.2
Overall effectiveness (UTSR vane), $\delta\boldsymbol{\phi}$	± 0.005	± 0.006	-	2.3.3, 2.3.1
External effectiveness, $\delta\boldsymbol{\tau}$	± 0.005	± 0.02		2.3.3, 2.3.2
Gas temperature, $\delta\boldsymbol{\theta}$	± 0.015	± 0.006	-	2.3.3, 2.3.1
Density ratio, δDR	± 0.01	± 0.005	-	2.3.3, 2.3.1
Mainstream velocity, δU_{∞}	± 0.05	± 0.1	m/s	2.1
Blowing ratio for PW vane, δM	± 0.05	± 0.015 – 0.05	-	2.1
Blowing ratio for UTSR vane, δM	± 0.05	± 0.25	-	2.1
Thermal resistance, δR	-	± 10%	m^2K/W	2.4

Chapter 3: Thermal Field Measurements

The thermal fields measurements made in this study were made on the adiabatic and conducting PW vanes for a single row of round film cooling holes on the suction side of the vane. Measurements were made to generate thermal profiles at x/d = 0, 5 and 10.

3.1. ADIABATIC EFFECTIVENESS MEASUREMENTS

This section presents the adiabatic effectiveness measurements made in this study in the form of contour plots and lateral averages. These data were collected in preparation for the thermal field measurements.

3.1.1. Comparison to previous data

Measurements of adiabatic effectiveness had previously been taken on the PW vane for the same row of film cooling holes on the suction side of the vane and reported in a study by Williams, et al. (Williams, et al., 2012). Therefore, it was logical to compare these previously collected measurements to those made for the present study as a check on consistency and repeatability before beginning the thermal field experiments. A comparison of the laterally averaged adiabatic effectiveness, $\bar{\eta}$, is given in Figure 3.1 between the measurements made in 2011 by Williams, et al., and those made in 2013 for the present study. There was a notable difference in that the previous data had a consistently higher $\bar{\eta}$ than the current measurements except for $M \approx 1.1$. Upon examining the data furthered it was determined that the data correlated best at the lowest effectiveness values. The results for $\bar{\eta}$ agree between the two tests for $\bar{\eta} < 0.1$ for all three blowing ratios. However, Figure 3.2 shows the same laterally averaged data for $M = 0.65$ with uncertainty bars, and all measurements agree within their uncertainty bands except

for a short region near the hole exit. The uncertainty in adiabatic effectiveness for the 2011 measurements was $\delta\eta = \pm 0.023$, and the uncertainty for the current measurements was $\delta\eta = \pm 0.01$. The laterally averaged effectiveness curves for the higher blowing ratios also agreed with uncertainty was taken into account.

Contour plots of adiabatic effectiveness are given in Figure 3.3 for the three blowing ratios of Figure 3.1. Both the contour plots and the laterally averaged curves of adiabatic effectiveness show peak effectiveness values for $M = 0.65$. The contour plots also show small discrepancies between the measurements made in 2011 and the measurements made for the current study. However, all of these deviations fall within the experimental uncertainty. The experimental uncertainty results from the temperature measurements as well as the blowing ratio measurements. The surface temperature measurements for the 2011 data were taken with a Flir P25 Infrared camera, while the current measurements were made with a Flir T620 Infrared camera. These cameras were calibrated against surface thermocouples as described in Chapter 2, and their calibration curves are shown in Figure 3.4. The calibration curve for the P25 had much greater fluctuations in measurements and thus had greater experimental uncertainty which was shown in Figure 3.2.

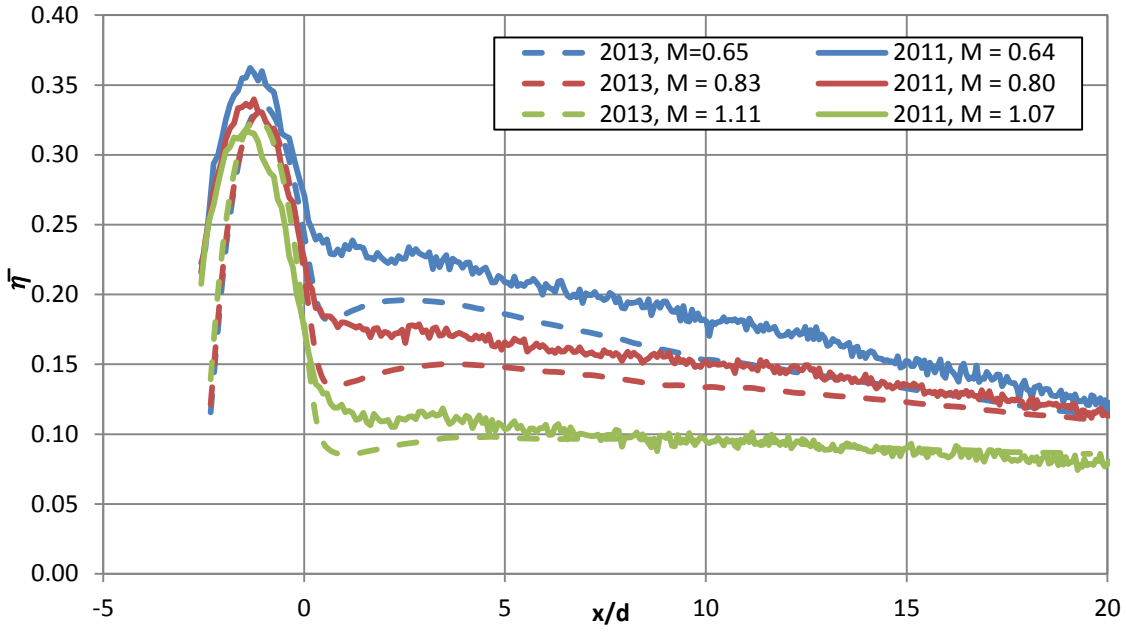

Figure 3.1: Laterally average adiabatic effectiveness for the PW vane

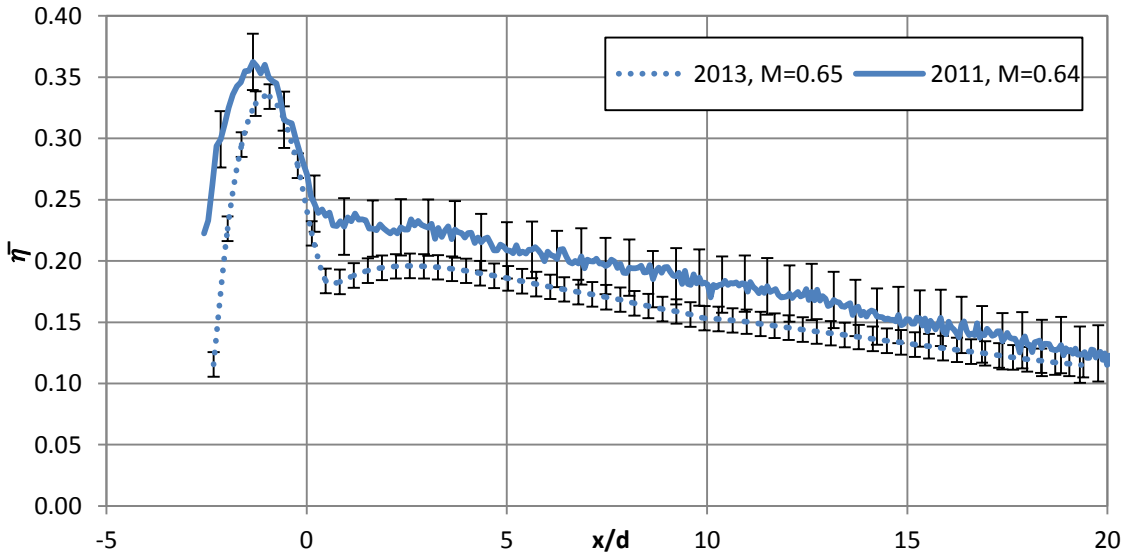

Figure 3.2: Laterally averaged adiabatic effectiveness for the 2013 and 2011 measurements with uncertainty bars

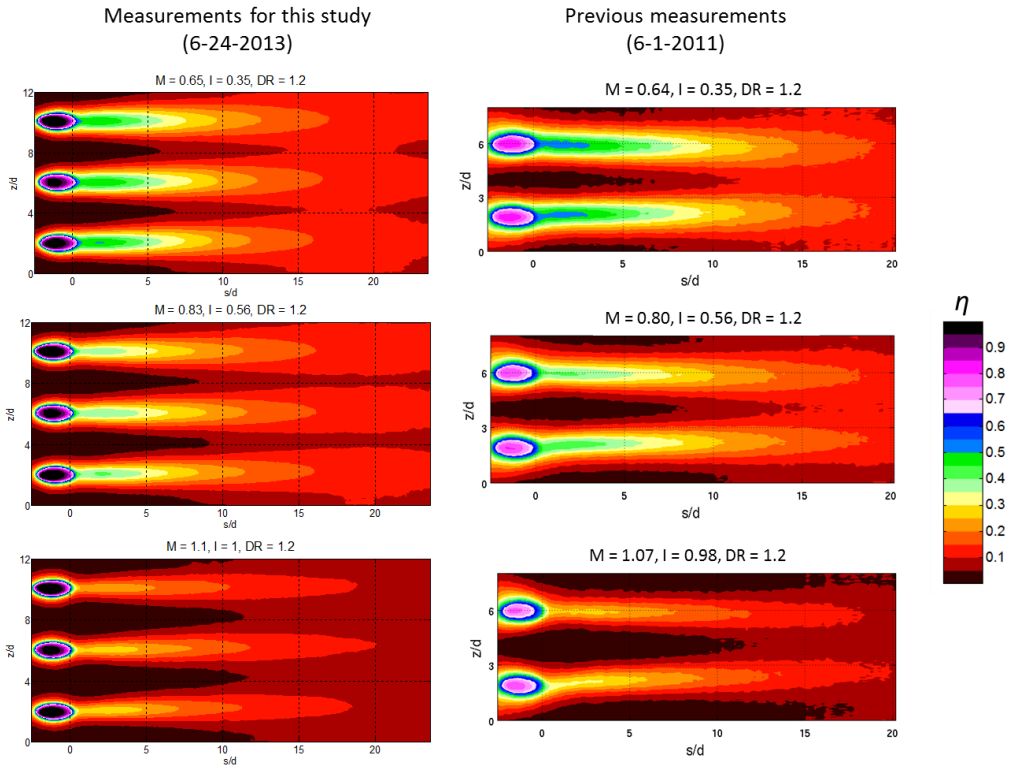

Figure 3.3: Contour plots of adiabatic effectiveness

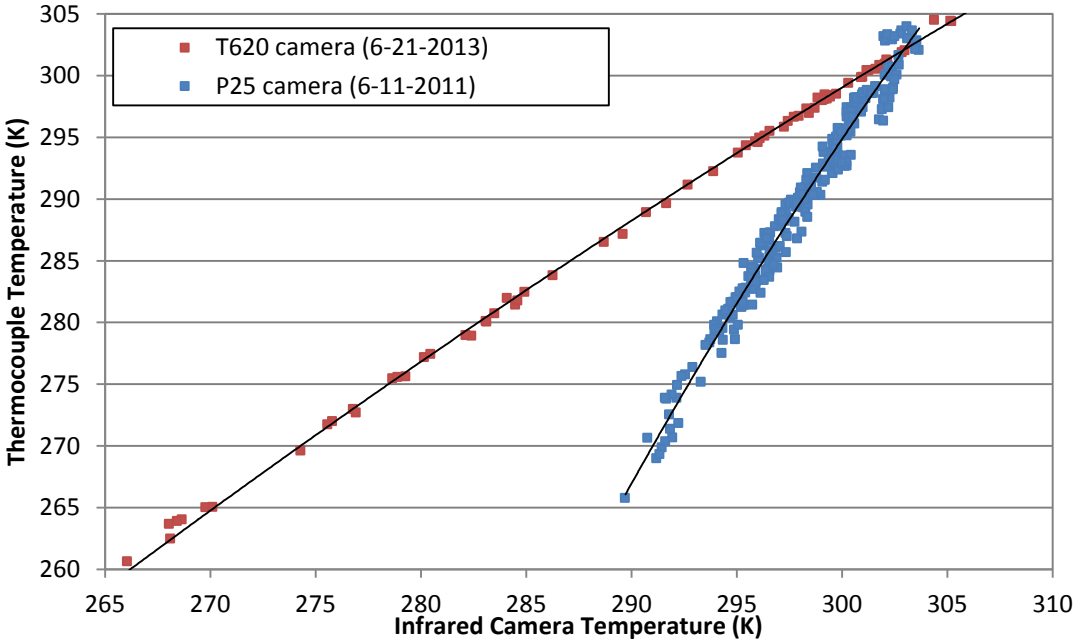

Figure 3.4: IR camera calibrations for the T620 (current measurements) and P25 (previous measurements)

3.1.2. Comparison to RANS simulations

The ultimate goal was to compare thermal fields between CFD data and experimental measurements, and so adiabatic effectiveness data were first compared to understand what types of differences were expected and what differences we wanted to better understand. Figure 3.5 presents laterally averaged adiabatic effectiveness for both the experimental measurements and computational simulations (Dyson, et al., 2012).

For the experimental measurements, the quick drop in $\bar{\eta}$ near $x/d \approx 1$ for $M = 0.65$, 1.11, and 2.41 implied the coolant jets separated from the jet surface, and in the case of $M = 0.65$ and 1.11, $\bar{\eta}$ started increasing shortly after this drop implying the coolant jets had partially reattached to the vane surface. However, these conclusions were just speculations based on the surface temperature measurements, to really know whether or not the jet was separated and reattaching, the thermal field above the wall needs to be analyzed. In contrast, $\bar{\eta}$ for $M = 0.28$ started much higher and steadily decayed at a faster rate because there was significantly less coolant on the vane surface and it diffused more quickly. In the case of $M = 2.41$, $\bar{\eta}$ dropped quickly and did not recover, implying the coolant jets at this blowing ratio were completely separated.

The computational predictions of $\bar{\eta}$ sometimes over-predicted laterally averaged effectiveness ($M = 0.28$), and sometimes under-predicted laterally averaged effectiveness ($M = 1.11$ and 2.41), and sometimes under-predicted and over-predicted $\bar{\eta}$ as was the case for $M = 0.65$. The point here was that, in general, it is difficult to resolve trends between CFD data and experimental measurements for laterally averaged adiabatic effectiveness data. The only consistent trend observed in Figure 3.5 was the "over-separated" nature of the computational predictions of $\bar{\eta}$ for $x/d \approx 1$ where the initial dip in $\bar{\eta}$ was much larger for the computational data than for the measurements for $M = 0.65$, 1.11, and 2.41.

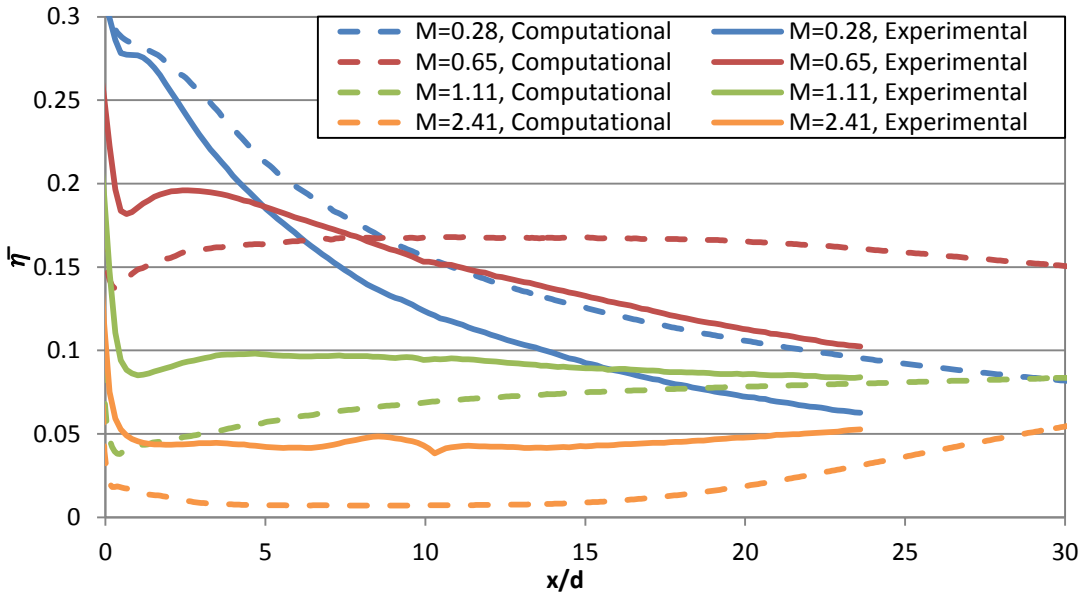

Figure 3.5: Laterally averaged adiabatic effectiveness measurements compared to CFD simulations

The contour plots of η, presented in Figure 3.6, gave greater insight into the differences between the computational data and the experimental measurements. The decrease and increase in effectiveness near the jet exit seen in the plots of $\bar{\eta}$ was also seen in the contour plots of η for the experimental measurements. Additionally, Figure 3.6(a) does not show the decrease followed by an increase in the experimental contour plots of $M = 0.28$ which contrasted the computational prediction in Figure 3.6(b) which showed a slight decrease in η and an increase around $x/d = 1$. The experimental contour plots for $M = 0.65$ and 1.11 show a decrease in η right at the hole exit and an increase around $x/d \approx 2$, and the computational predictions also show this quick decrease in η, but the increase does not occur until further downstream. The highest blowing ratio showed an interesting case where the computational jet leaves no footprint on the vane surface while the experimental measurements show the coolant jet having a low effectiveness footprint. It was speculated that the quick decrease in η, followed by an increase in η, was the result

of the coolant jet separating from the vane surface then reattaching, but to fully evaluate the CFD predictions and jet separation, the thermal field above the vane was analyzed.

In general, the computational predictions under-predicted the lateral dispersion and decay of the coolant jet. In Figure 3.6, none of the computational coolant jets merged at any downstream location while experimental measurements at the three lower blowing ratios all showed jet merging at some downstream position. Additionally, the computational jets remained colder for distances further downstream when compared to the experimental results. By x/d = 15, the centerline of the jet in Figure 3.6(a) had decayed to around $\eta \approx 0.10$, while the centerline of the jet in Figure 3.6(b) had decayed to $\eta \approx 0.30$. A similar trend was seen for M = 0.65 and 1.11 where the computational prediction showed much higher η values far downstream of the coolant holes while the experimental data showed significant decay; however, M = 2.41 did not exhibit this trend because for the computational jet there was zero effectiveness on the vane surface. Just as the contour plots of η were necessary to show how the coolant spread on the vane surface and that the computational data under-predicted lateral spreading, the thermal field above the vane wall is necessary to fully evaluate the CFD predictions of the coolant flow.

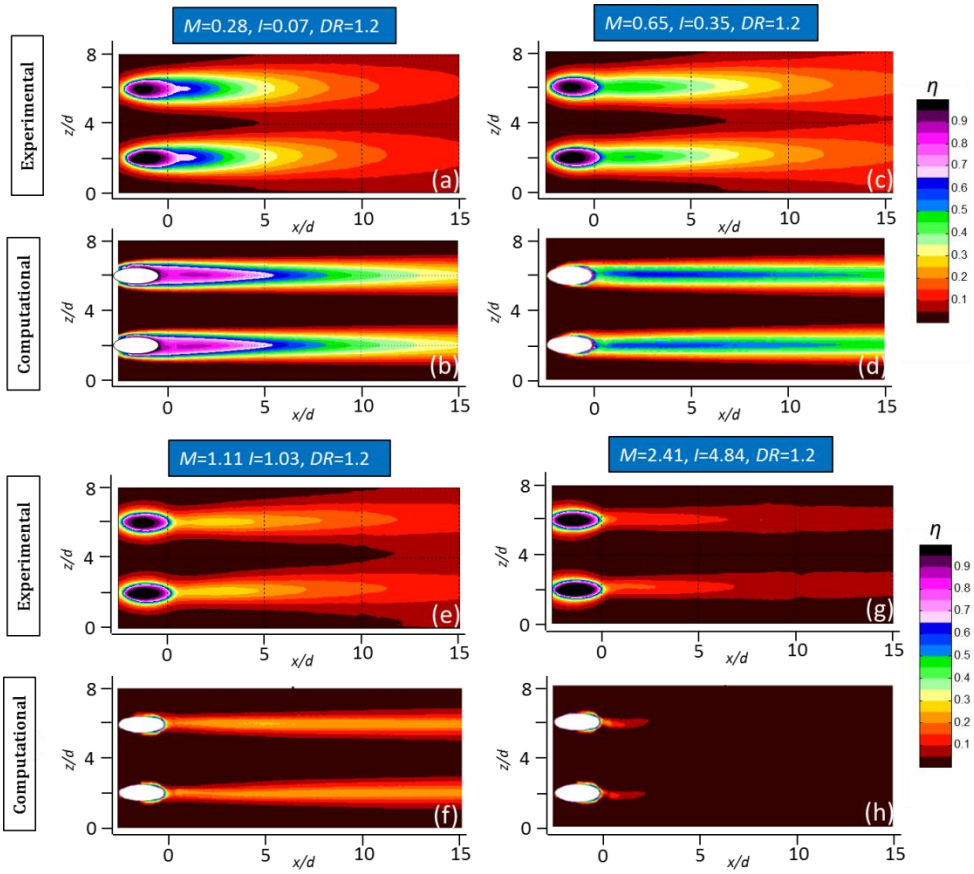

Figure 3.6: Contour plots of adiabatic effectiveness experimental measurements compared to computational predictions (Dyson, et al., 2012)

3.2. OVERALL EFFECTIVENESS MEASUREMENTS

This section presents the overall effectiveness measurements made in this study in the form of contour plots and lateral averages. These data were collected in preparation for the thermal field measurements.

3.2.1. Comparison to previous measurements

The overall effectiveness measurements were compared to the previous data (2011), and while some discrepancies were seen, all measurements agreed within experimental uncertainty.

3.2.2. Comparison to RANS simulations

Similar to the adiabatic effectiveness measurements, overall effectiveness measurements were made to compare with the computational predictions in order to better understand differences with the thermal field measurements. Laterally averaged overall effectiveness measurements and computational predictions are presented in Figure 3.7. In comparison to the laterally averaged η plots, the laterally averaged ϕ plots were much less indicative to showing trends across coolant flow rates and between the experiments and computations. Each blowing ratio had a very unique $\bar{\eta}$ profile in Figure 3.5, but all blowing ratios had very similar $\bar{\phi}$ profiles in Figure 3.7. Overall effectiveness is the result of the conjugate effects of internal cooling and film cooling. For the PW vane model the level of internal cooling increases with blowing ratio because the film coolant and the internal coolant are the same. The $\bar{\phi}$ plot for M = 0.65 most likely had higher effectiveness than M = 1.11 and 2.41 because of the higher level of film cooling effectiveness shown in Figure 3.6(c) even though M = 1.11 and 2.41 had higher levels of internal cooling, and M = 2.41 had higher effectiveness than M = 1.11 because of the greater level of internal convection cooling and in-hole convection cooling. These trends were better shown in contour plots of overall effectiveness in Figure 3.8. Cold regions between the coolant holes indicated the level of in-hole convection cooling, and cold regions downstream of the film cooling holes indicated the level of film cooling.

However, with the matched Biot number model, there was significant lateral conduction in the vane wall that hid some of the film cooling effectiveness.

In the comparison of the RANS simulations and the experimental $\bar{\phi}$ measurements, it was difficult to find any discernable difference, and in fact most of the computational data lies within the uncertainty of the experimental measurements. In the computational simulation, the aft passage was simulated using an internal heat transfer coefficient from channel flow. Dyson (2012) reported that this was a poor approximation of the heat transfer in the aft passage, and for this reason, overall effectiveness dips for $x/d > 11$ in Figure 3.7 in the computational simulations because the internal cooling was poorly simulated for this location. However, the thermal field measurements were conducted upstream of the aft passage in a region above the fore passage, and therefore it was not expected that this difference would have an effect on the comparisons made in this study.

Similar to the plot $\bar{\eta}$ measurements, the $\bar{\phi}$ measurements were not very insightful into the differences between the computational and experimental coolant jets. Thus, contour plots of ϕ were compared between the computational data and experimental measurements in Figure 3.8. The computational model predicted a colder vane surface for $M = 0.65$ especially under the coolant jet where ϕ was predicted to be greater than 0.35, and it was experimentally measured to be ~0.25 – 0.30. However, for $M = 1.11$, the simulation predicted the ϕ distribution on the surface well except for between the coolant hole exits. The CFD model over-predicted the effect of in-hole convection cooling which resulted in an over-prediction of ϕ between the coolant holes. For $M = 2.41$, the level of in-hole convection was better predicted which was seen by the more similar ϕ distributions for $x/d < 0$. Additionally, the prediction of the downstream ϕ distribution

was acceptable for x/d < 15. However, the CFD prediction of ϕ for M=2.41 was not expected to show signs of film cooling because the contour plot of η in Figure 3.6(h) showed no signs of film cooling, and Figure 3.8(h) showed higher levels of effectiveness underneath the coolant jet. This was likely the cause of increased heat transfer coefficients between the coolant jets but will be explored in depth in thermal fields section. The under-prediction of jet spreading seen in Figure 3.6 was hidden in Figure 3.8 because of the lateral conduction in the vane wall.

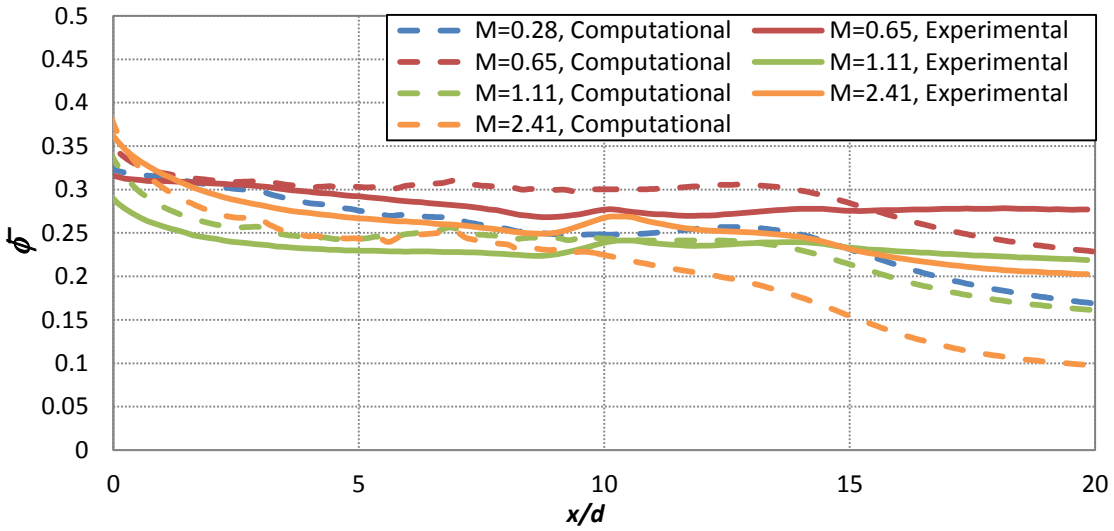

Figure 3.7: Laterally averaged overall effectiveness measurements compared to CFD simulations (Dyson, et al., 2012)

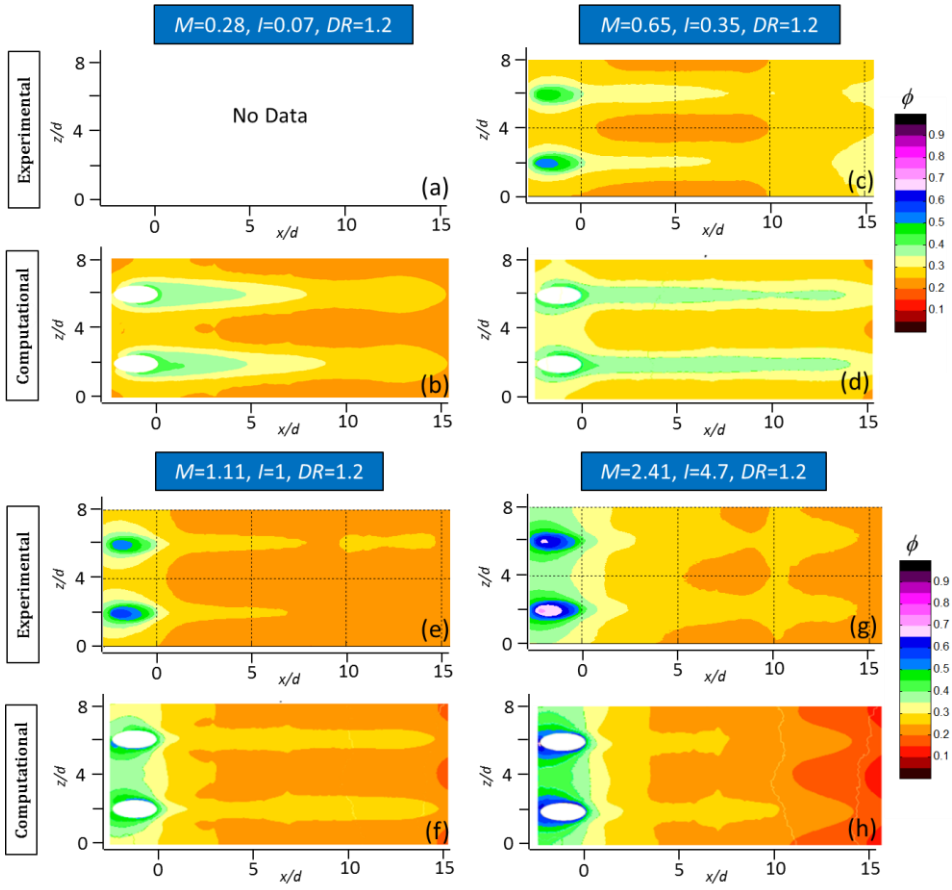

Figure 3.8: Contour plots of overall effectiveness experimental measurements compared to computational predictions

3.3. THERMAL FIELD MEASUREMENTS

This section presents the thermal field measurements for the PW adiabatic and conducting vane models. Measurements were made at x/d = 0, 5, 10 for M = 0.28, 0.65, 1.11, and 2.41. Measurements at x/d = 0 will be presented separately, but measurements at x/d = 5 and 10 will be presented by blowing ratio and compared to CFD simulations of Dyson, et al. The purpose of these measurements was to directly measure the conjugate heat transfer effects on the thermal fields of film cooling jets for a well simulated turbine vane.

3.3.1. Thermal fields at $x/d = 0$

It was important to make measurements immediately at the hole exit, at $x/d = 0$, to compare the thermal profiles of the jets exiting the adiabatic and conducting vane models. If the profiles were similar, then the downstream thermal profiles could be compared; however, if the profiles had significantly different profiles exiting the hole, it would have been difficult to compare the adiabatic and conducting vane thermal fields. The profiles could have been significantly different because of the in-hole convection that occurred in the case of the conducting vane model. The mean gas temperature sometimes increased as much as 10 K from inside the vane to the hole exit. This convection could have altered the thermal profile of the jet before it exits the hole.

Contour plots of the thermal fields are presented in Figure 3.9 comparing the adiabatic and conducting vane models at x/d = 0. In Figure 3.9(b), (d), (f) and (h), the thermal boundary layer developed over the conducting vane model and was seen for $z/d<1$ and $z/d > 3$. The upstream conditions were the same for all four blowing ratios, so the consistency in the thickness of the thermal boundary layer, $y/d = 0.25$, was a good check on repeatability.

For $M = 0.28$, the wall-normal dispersion of the jet was equivalent for the adiabatic and conducting vane models. The lateral dispersion was more difficult to gauge because of the thermal boundary layer; however, the lateral dispersion of the jet core, an area expected to be untouched by mixing with the thermal boundary layer, was equivalent between the two vane models. The wall-normal spreading of the jet was comparable for the other three blowing ratios between the adiabatic and conducting models, as well. Additionally, the lateral spreading of the jet core was similar for $M = 0.65$, 1.11, and

2.41, but with the presence of the thermal boundary layer the lateral dispersion was more difficult to judge.

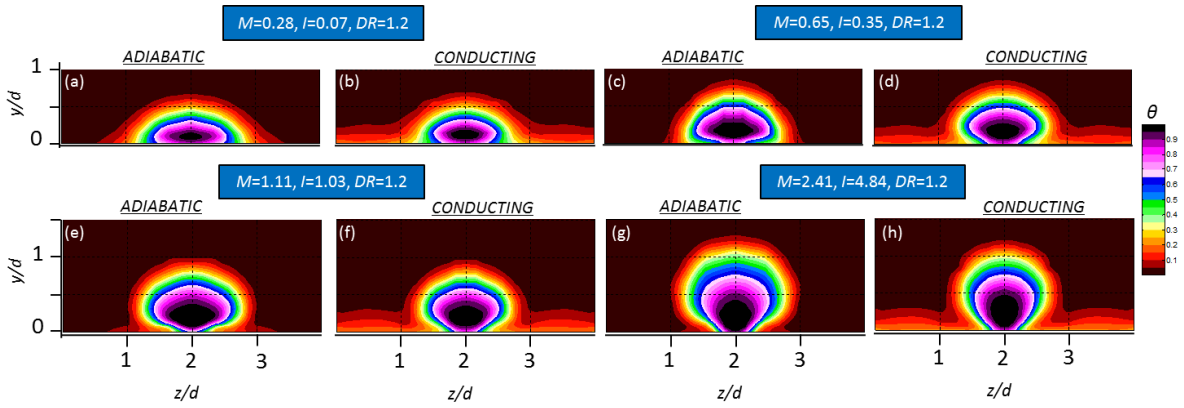

Figure 3.9: Experimental thermal field measurements at $x/d = 0$ for $M = 0.28, 0.65, 1.11$, and 2.41

Surprisingly, these measurements indicated that the thermal boundary layer only flowed around the coolant jet, not over it, for all four blowing ratios. This result is highlighted in Figure 3.10 which shows centerline profiles of θ for all four blowing ratios and above the adiabatic and conducting vane models. None of the centerline profiles of θ above the conducting vane show an increase in θ over the adiabatic vane profile near the top of the jet as would be expected if the upstream thermal boundary layer flowed over the top of the coolant jet. The thermal boundary layer produced no significant effect on the centerline θ profile at $x/d = 0$.

The centerline profiles of θ in Figure 3.10 were also very similar near the vane wall between the adiabatic and conducting vane models. At $x/d = 0$, there had not been any heat transfer between the coolant jet and the vane wall that had significantly altered the thermal profile of the coolant jet exiting the hole, even near the vane wall. Also, even the lowest blowing ratio showed slight separation this close to the hole exit. The core of the coolant jet was at $y/d = 0.1$.

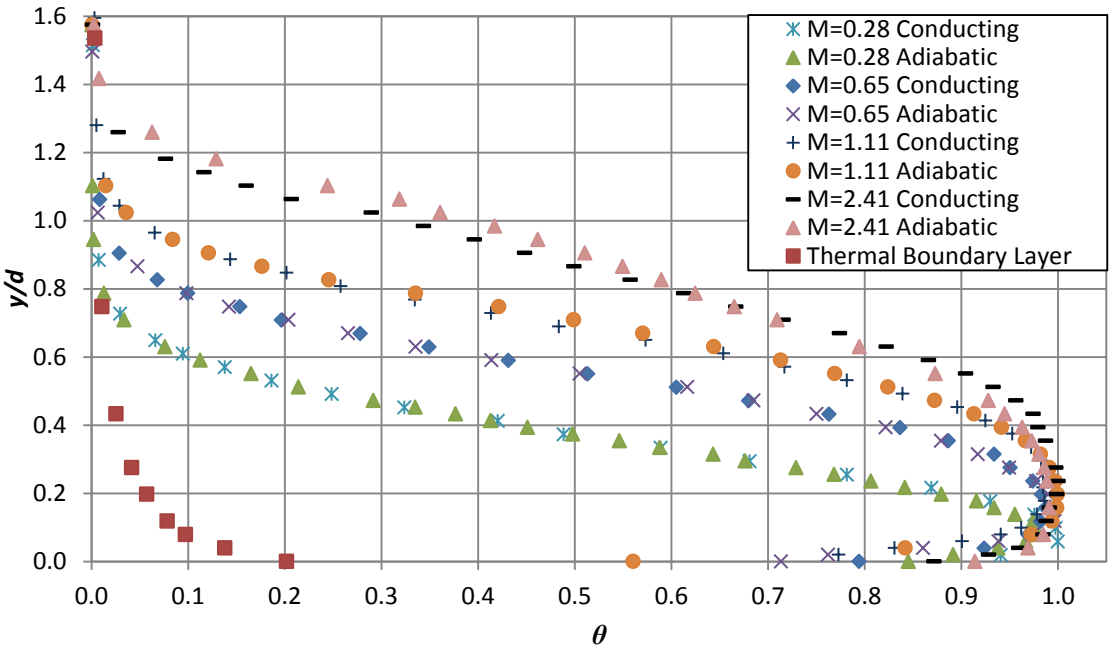

Figure 3.10: Centerline profiles of θ above the adiabatic and conducting vane models at $x/d = 0$

3.3.2. Thermal fields for $M = 0.28$

Experimental and computational (Dyson, et al., 2012) thermal fields are presented in Figure 3.11 for $M = 0.28$ at $x/d = 5$ and 10. Both the experimental measurements and the computational jet showed that jet core or coldest region of the coolant jet was attached to the vane surface at both $x/d = 5$ and 10. At $x/d = 5$, the core of the experimental coolant jet above the adiabatic vane wall was $\theta \approx 0.35$ in Figure 3.11(a), but the core of the experimental jet above the conducting vane wall was $\theta \approx 0.40$ in Figure 3.11(e). A similar difference was seen at $x/d = 10$. The jet core was colder above the conducting vane because the coolant jet was mixing with the cold thermal boundary layer above the conducting vane as opposed to the hot mainstream flow above the adiabatic vane model. Off the centerline the vane wall was colder than the over-flowing gas, so the outside regions of the jet were cooled by the vane wall. This cooled gas was then swept

towards the centerline by the counter-rotating vortices. However, overall, the thermal profiles of the coolant jets above the adiabatic and conducting vane walls were very similar. The extent of the wall-normal dispersion of the jets above the adiabatic and conducting vane wall was equivalent. It was more difficult to determine the extent of the lateral spreading of the coolant jet above the conducting vane because of the interaction with the thermal boundary layer. However, making the comparison above y/d = 0.5, where the effect of the thermal boundary was expected to be minimal, the lateral dispersion was equivalent between the two vane models.

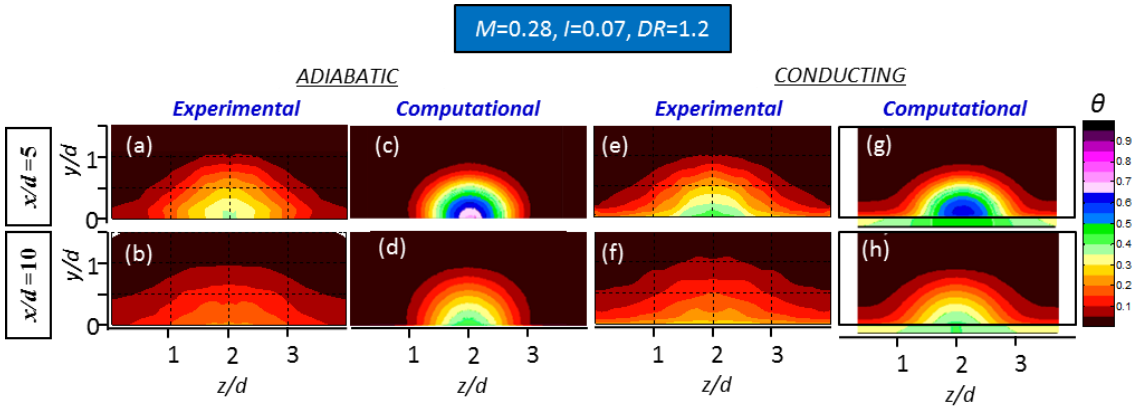

Figure 3.11: Experimental and computational (Dyson, et al., 2012) thermal fields above the adiabatic and conducting vane surfaces at x/d = 5 and 10, M = 0.28

Figure 3.11(c) and (d) showed that the CFD simulation accurately predicted the extent of the wall-normal spreading of the coolant jet at x/d = 5 and 10, showing it extended to y/d = 1. However, the level of lateral spreading was significantly under-predicted which was consistent with the contour plots of η in Figure 3.6. By x/d = 5, the experimental jet above the adiabatic wall in Figure 3.11(a) had already spread the entire width of the pitch, but the simulated jet had only spread to half the pitch. The computational prediction of the coolant jet above the conducting vane wall hides some of

the under-prediction in lateral spreading because of the interaction with the thermal boundary layer.

The core of the CFD coolant jet in Figure 3.11(c) was $\theta \approx 0.75$ while the core of the experimental jet in Figure 3.11(a) was $\theta \approx 0.35$. The computational model predicted a much colder jet core than the experimental results showed, and this was likely the result of the under-prediction in lateral spreading. The simulation predicted a substantially colder jet core for both vane models at both locations.

Figure 3.12 and Figure 3.13 present centerline profiles of θ above the adiabatic and conducting vane models at $x/d = 5$ and 10, respectively. The IR camera measurement of the surface temperature was included for comparison to the gas temperature above the wall and to determine if the adiabatic wall temperature was an appropriate approximation for the driving temperature for heat transfer. It is impossible to experimental measure a truly adiabatic vane surface, so the effects of lateral conduction could only be minimized by using a low thermal conductivity material. However, a perfectly adiabatic wall can be simulated computationally, so the differences between a vane model with a truly adiabatic wall and vane model with thermal properties similar to the low thermal conductivity polyurethane used in the experimental vane are shown in Figure 3.14. Typically, a 1-D conduction correction is applied to measurements of adiabatic effectiveness on the vane model to account for conduction through the vane wall. However, there was also lateral conduction of heat towards the centerline of the coolant jet profile, so in some regions the 1-D through-wall correction was appropriate and in some regions it was not appropriate. Figure 3.14 provides a comparison of computationally simulated surface temperatures for a truly adiabatic vane wall and a low thermal conductivity vane wall. The jet centerline temperatures on the truly adiabatic

vane surface were colder than the centerline temperatures on the low thermal conductivity vane wall. This was the result of lateral conduction of heat towards the jet centerline in the low thermal conductivity wall. The through wall 1-D correction will reduce η in all locations, but this would only exacerbate the error in the centerline temperatures for the low thermal conductivity wall. Therefore, the surface temperature measurements of the "adiabatic vane" reported in Figure 3.12 and Figure 3.13 do not include the 1-D correction. A 3-D conduction correction could be formed from the CFD surface temperature data given in Figure 3.14, but this correction would only apply for the CFD data and not the experimental measurements. For this reason, the gas temperature measurements above the adiabatic vane surface were used to determine if the adiabatic wall temperature was the driving temperature for heat transfer and not the vane surface temperature measurement.

In Figure 3.12, the gas temperatures above the adiabatic and conducting vane model were consistent except for $y/d < 0.25$, where the gas temperature above the conducting model was colder than the gas above the adiabatic model. The deviation between the two profiles had extended to $y/d \approx 0.5$ at $x/d = 10$ in Figure 3.13 because more mixing had now occurred. The dotted red line indicates the adiabatic wall temperature measured with the IR camera without a one-dimensional correction for conduction through the vane wall. For the adiabatic wall temperature to be a reasonable approximation of the driving temperature for heat transfer, it needs to be the effective freestream temperature that the conducting wall sees, implying there has not been a significant change in the thermal profile because of conjugate effects. The driving temperature, or effective freestream temperature, is where the thermal profile above the conducting wall deviates from the adiabatic wall because that would be the edge of the

thermal boundary layer for the conducting wall. At x/d = 5, in Figure 3.12, the deviation between the two thermal profiles occurs near the vane surface and at a temperature close to the adiabatic wall temperature, so the adiabatic wall temperature was a reasonable approximation of the driving temperature for heat transfer. However, at x/d = 10 in Figure 3.13, the deviation occurred much further from the vane surface and at a much different temperature than the temperature near the adiabatic vane surface. Therefore, at this position the adiabatic wall temperature was not a good indication of the driving temperature for heat transfer.

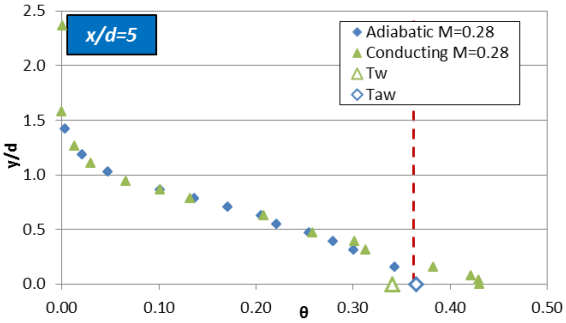

Figure 3.12: Centerline profiles of θ, z/d = 2, x/d = 5, M = 0.28

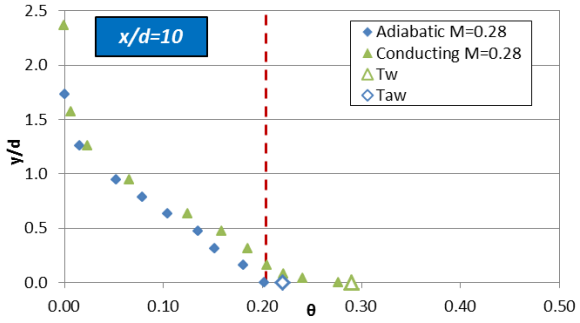

Figure 3.13: Centerline profiles of θ, z/d = 2, x/d = 10, M = 0.28

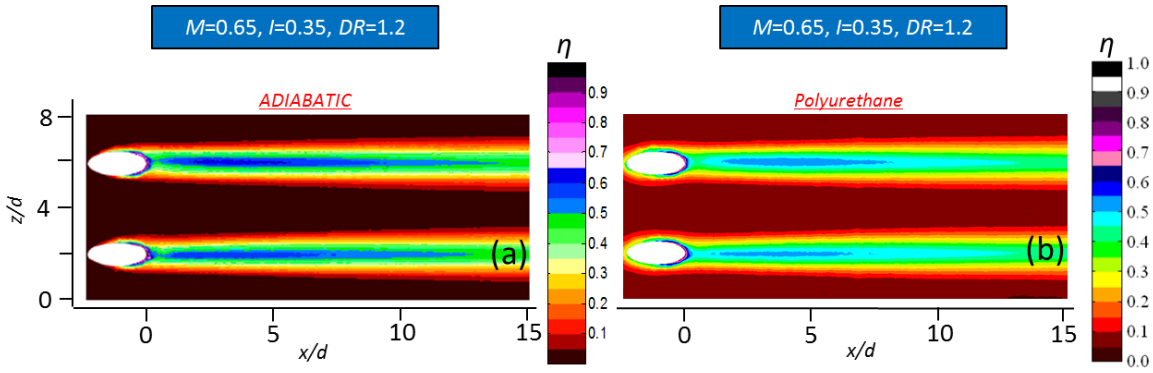

Figure 3.14: Comparison of CFD simulations of an (a) adiabatic wall and a (b) low thermal conductivity wall (Dyson, et al., 2012)

3.3.3. Thermal fields for $M = 0.65$

Experimental and computational (Dyson, et al., 2012) thermal fields are presented in Figure 3.15 for $M = 0.65$ at $x/d = 5$ and 10. At $x/d = 5$, Figure 3.15(a) and (e) show similar experimental thermal profiles above the adiabatic and conducing vane models except in the region very neat the vane wall, $y/d < 0.25$. In contrast to the results for $M = 0.28$, the near wall region was warmer (lower θ) above the conducting wall than above the adiabatic wall. The thermal profiles of the centerline of the experimental jets at $x/d = 5$ shown in Figure 3.16, including IR camera measurements of surface temperature, show that the conducting wall temperature was significantly warmer than the coolant jet core. Thus, the conducting wall warmed the coolant gas near the vane wall causing the difference in thermal profiles between the conducting and adiabatic vane models. Furthermore, at $x/d = 10$, the thermal profiles were largely similar between the conducting and adiabatic vane models in Figure 3.15(b) and (f), and the centerline thermal profiles of the experimental coolant jets in Figure 3.17 highlight this similarity. In Figure 3.17, the thermal profiles were almost identical except for the region very near the vane wall, $y/d < 0.2$, where the vane wall, now colder than the core of the coolant jet, was cooling the gas above the wall. Despite the small differences between the thermal profiles above the adiabatic and conducting vane models, the adiabatic wall temperature was a good approximation of the driving temperature for heat transfer for $M = 0.65$ because the θ at the deviation between the two thermal profiles was a good representation of the wall temperature.

In Figure 3.16, the gas temperature measurements above the adiabatic wall were slightly colder (higher θ) than the surface temperature measurement. This was representative of the previously discussed lateral conduction towards the vane centerline,

and this was why the gas temperature measurements were used to determine whether or not the adiabatic wall gives a good indication of the driving temperature for heat transfer.

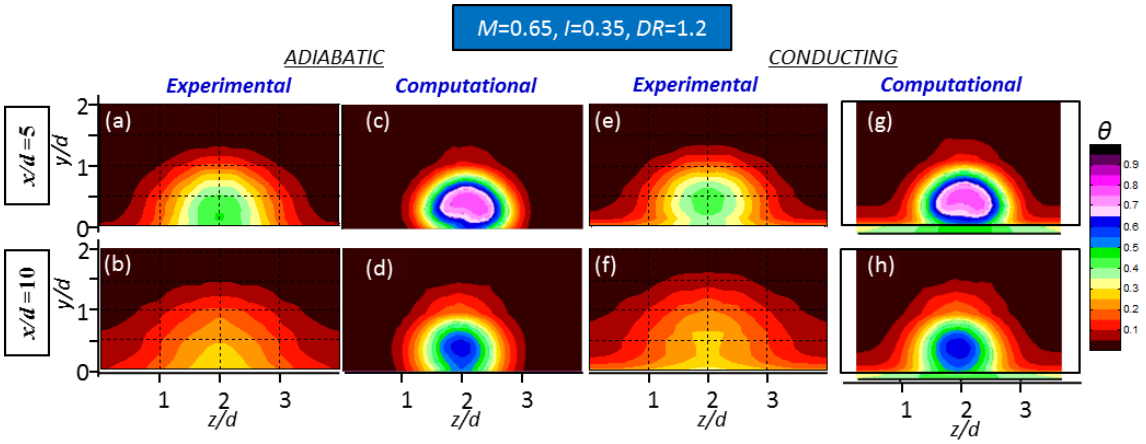

Figure 3.15: Experimental and computational (Dyson, et al., 2012) thermal fields above the adiabatic and conducting vane surfaces at x/d = 5 and 10, M = 0.65

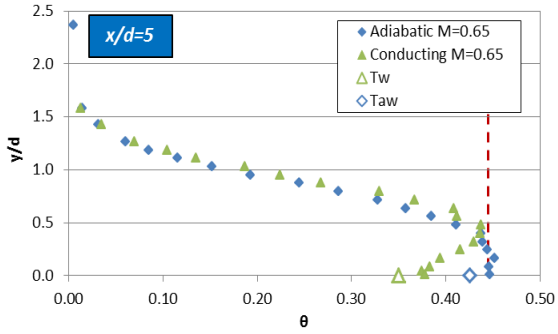

Figure 3.16: Centerline profiles of θ, z/d = 2, x/d = 5, M = 0.65

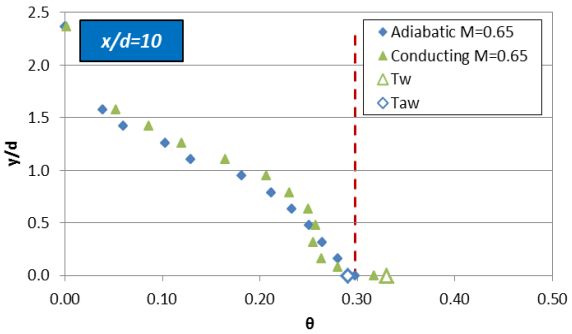

Figure 3.17: Centerline profiles of θ, z/d = 2, x/d = 10, M = 0.65

The full 2-D thermal profiles in Figure 3.15 show the computational model predicted a much colder jet core above both the adiabatic and conducting vane models and at both streamwise positions. A comparison of the centerline thermal profiles of the experimental and computational coolant jets at x/d = 5 is given in Figure 3.18. Figure 3.18 emphasizes the magnitude of the discrepancy between the computationally predicted thermal profile and the experimentally measured thermal profile. The thermal profiles aligned for y/d > 1.0, but for y/d < 1, the CFD model predicted a much colder thermal

profile with jet core temperature of $\theta \approx 0.8$, where the experimental profile had a jet core of $\theta \approx 0.44$. Additionally, the core, or coldest region, of the experimental jet extends to very near the vane surface in the experimental measurements, while the computational jet showed significant decrease between the core and the wall. Both the experimental and simulated coolant jets extended to $y/d = 1.25$ in Figure 3.15(a) and (c), showing that the CFD model did accurately predict the level of wall-normal spreading again; this result was confirmed in Figure 3.18. However, the computation under-predicted the lateral spreading as it did for $M = 0.28$. The experimental coolant jet spanned the entire pitch in Figure 3.15(b) while the computational coolant jet spanned only half the pitch in Figure 3.15(d). Additionally, the level of lateral spreading grows from $x/d = 5$ to 10 for the experimental jet, but the computational coolant jet did not grow in size significantly between $x/d = 5$ and 10. The under-prediction in lateral spreading was the result of an under-prediction in turbulent mixing that is a common problem with RANS models. Comparing the computational thermal profiles above the adiabatic and conducting vane wall shows the conducting wall had very little to no effect on the coolant jet profile.

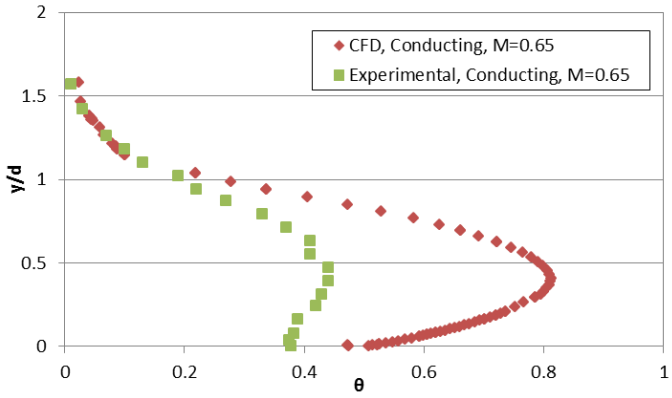

Figure 3.18: Centerline profiles of θ at x/d=5 and M=0.65 comparing experimental measurements and computational predictions (Dyson, et al., 2012)

3.3.4. Thermal fields for $M = 1.11$

The experimentally measured and computationally simulated 2-D thermal profiles at $x/d = 5$ and 10 for $M = 1.11$ are shown in Figure 3.19. Comparing Figure 3.19(a) and (e), the conducting vane wall affected the thermal profiles only near the edges of the jet where the jet interacted with the thermal boundary layer at $x/d = 5$. The centerline experimental thermal profiles of the jet above the adiabatic and conducting vane walls in Figure 3.20 shows there was a very small effect of the wall for $y/d < 0.05$. The conducting wall had a limited effect on the thermal profile because $T_w \approx T_{aw}$. However, the core of the coolant jet in Figure 3.19(f), above the conducting wall, was larger than the core above the adiabatic wall in Figure 3.19(b). The centerline thermal profiles at $x/d = 10$ are presented in Figure 3.21, and the profiles align between the two models for $y/d > 1$ and deviate for $y/d < 1$. The colder jet core above the conducting wall was different from the results for $M = 0.28$ and 0.65 because for $M = 0.28$ and 0.65 the coldest region of the coolant jet existed very near the jet wall. The coolant jet was separated from the vane wall for $M = 1.11$, so a counter-rotating vortex pair (CVP) exists. In the case of the adiabatic wall, the CVP drew in hot mainstream gas, warming the core of the coolant jet, but in the case of the conducting vane wall, the CVP drew in the cold thermal boundary layer, cooling the core of the jet. At $x/d = 5$, the adiabatic wall temperature was a good estimation of the driving temperature for heat transfer because the thermal profile was largely unaffected by the conducting vane wall; however, at $x/d = 10$, the adiabatic wall temperature was not a good indication of the driving temperature for heat transfer because the thermal profile was beginning to be significantly altered by the conducting vane wall.

The CFD prediction of the film cooling jet in Figure 3.19(c) shows the CVP has actually split the jet core into to two parts which was an over-prediction of the strength of the CVP when compared to Figure 3.19(a). The strength of the CVP was broken up by turbulent mixing in the experimental measurements, but the under-prediction of turbulent mixing in the computational data resulted in the over-prediction of the CVP. The core of the jet above the conducting vane wall in Figure 3.19(h) was moderately colder than the core of the jet above the adiabatic wall in Figure 3.19(d). This was consistent with the trend in the experimental measurements where the CVP drew in the cold thermal boundary layer as opposed to hot mainstream gas, resulting in a colder jet core and near wall region.

Consistent with the $M = 0.28$ and 0.65, the CFD model predicted a much colder jet core than was experimentally measured. The two cores of the predicted jet in Figure 3.19(c) were $\theta \approx 0.8$ while the core of the jet in the experimental measurements in Figure 3.19(a) was $\theta \approx 0.45$. Additionally, at $x/d = 5$, the experimental jet had spread laterally to 75% of the pitch, while the computationally predicted jet had only spread to 50% of the pitch. Furthermore, the predicted jet did not grow or diffuse from $x/d = 5$ to $x/d = 10$, and the experimentally measured jet did. However, both the thermal profiles measured and simulated showed the jet the spreading in the wall normal direction to $y/d \approx 2$ at $x/d = 10$, so the CFD model did adequately predict the level of wall normal spreading

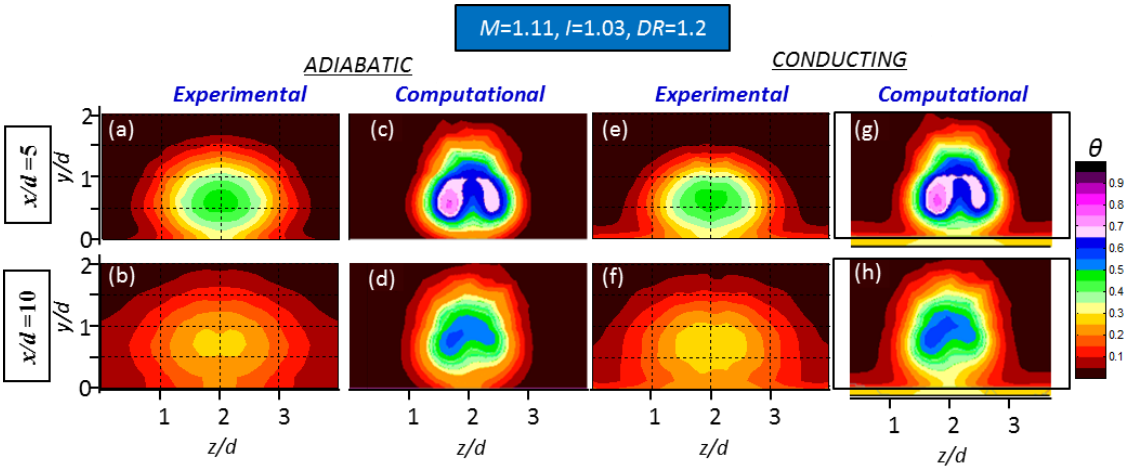

Figure 3.19: Experimental and computational (Dyson, et al., 2012) thermal fields above the adiabatic and conducting vane surfaces at x/d = 5 and 10, M = 1.11

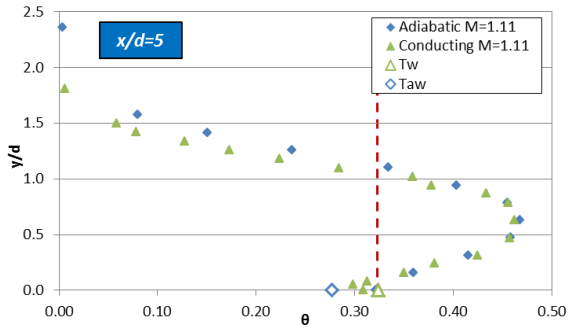

Figure 3.20: Centerline profiles of θ, z/d = 2, x/d = 5, M = 1.11

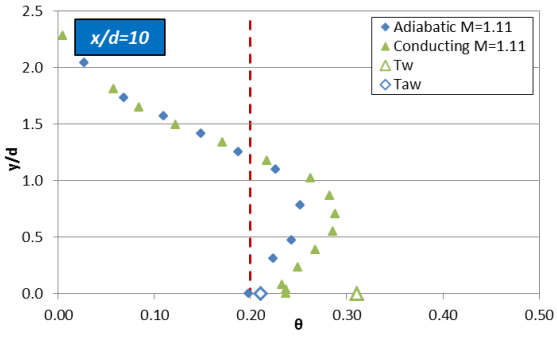

Figure 3.21: Centerline profiles of θ, z/d = 2, x/d = 10, M = 1.11

3.3.5. Thermal fields for M = 2.41

The experimentally measured and computationally simulated 2-D thermal profiles at x/d = 5 and 10 for M = 2.41 are shown in Figure 3.22. The experimental thermal profiles at x/d = 5 above the adiabatic, Figure 3.22(a), and conducting, Figure 3.22(e), vane models were identical except a region very near the vane wall, y/d < 0.25. The core of the coolant jet in both thermal profiles showed a slight kidney shape as a result of the CVP, but by x/d = 10, neither thermal profile showed a kidney shaped core in Figure 3.22(b) or (f). The thermal profiles were identical at x/d = 10 above the adiabatic and

conducting vane models except for $y/d < 0.5$. Figure 3.23 and Figure 3.24 present centerline thermal profiles of θ above the adiabatic and conducting vane models at x/d =5 and 10, respectively, along with IR camera measurements of surface temperature. The core of the coolant jet was so far separated from the surface of the vane there was no mixing between the jet core and the thermal boundary layer. In fact, in Figure 3.23, a thermal boundary layer was measured developing underneath the coolant jet core above the conducting vane mode. The centerline profile of θ above the conducting vane decreased to a value near the adiabatic wall temperature as it approached the vane wall, then increased to the conducting wall temperature. In this case, because the minimum θ between the jet core and the wall was near the adiabatic wall temperature, the adiabatic wall temperature was a reasonable approximation for the driving temperature for heat transfer. In Figure 3.24, the thermal boundary layer continued to develop, deviating further from the thermal profile above the adiabatic vane model. As the coolant jet continues downstream, this thermal boundary layer will continue to grow and the deviation between the thermal profile above the conducting vane and adiabatic vane models will grow with it. At $x/d = 10$, the minimum θ between the jet core and vane wall was different than the gas temperature above the adiabatic wall, so at this location the adiabatic wall temperature was not a good indication of the driving temperature for heat transfer.

While the experimental measurements showed kidney bean shape in the thermal profile in Figure 3.22(a), the computational prediction showed the CVP had split the jet into two cores in Figure 3.22(c). The over-prediction of the strength of the CVP was consistent for the thermal fields for $M = 1.11$. The CVP lifted the thermal boundary layer beneath the jet into the jet core above the conducting vane model in Figure 3.22(g) and

(h). The CFD model predicted a colder jet core than measured experimentally, but the core temperature difference between the predicted ($\theta = 0.6$) and measured ($\theta = 0.43$) was closest at M =2.41 among all blowing ratio, but the simulation still had a 40% error. This was most likely the result of the over-prediction of the strength of the CVP warming the jet core in the simulation, the way turbulent mixing was warming the jet core in the experiment. So, although the prediction more closely agreed with the experimental results than the other blowing ratios, the fundamental physics driving the dispersion of the coolant jet in the case of the experimental and computational thermal fields was different.

The CFD model correctly predicted the height of the coolant jet core, but over-predicted how far the jet would extend above the vane surface. Furthermore, the computation under-predicted the extent of the lateral spreading in comparison to the experimental thermal fields. At x/d = 10, the experimental thermal field in Figure 3.22 (b) spanned the entire pitch, while the predicted thermal field in (d) only covered 75% of the pitch. This was consistent with the results from the previous blowing ratios.

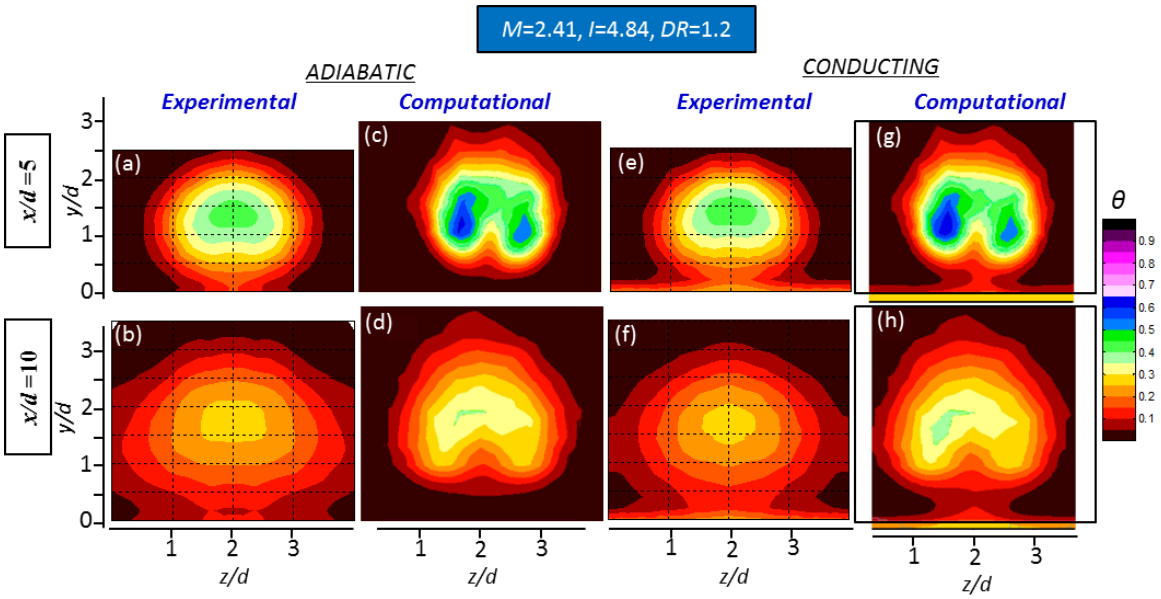

Figure 3.22: Experimental and computational (Dyson, et al., 2012) thermal fields above the adiabatic and conducting vane surfaces at x/d = 5 and 10, M = 2.41

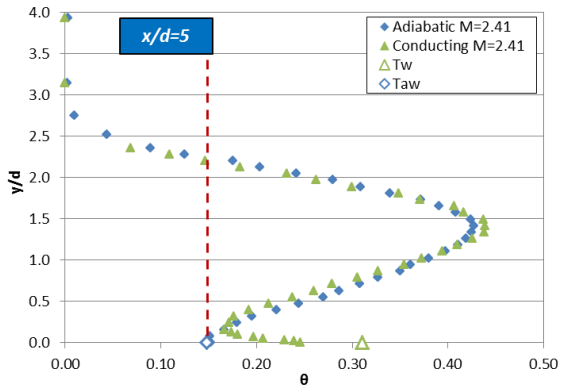

Figure 3.23: Centerline profiles of θ, z/d = 2, x/d = 5, M = 2.41

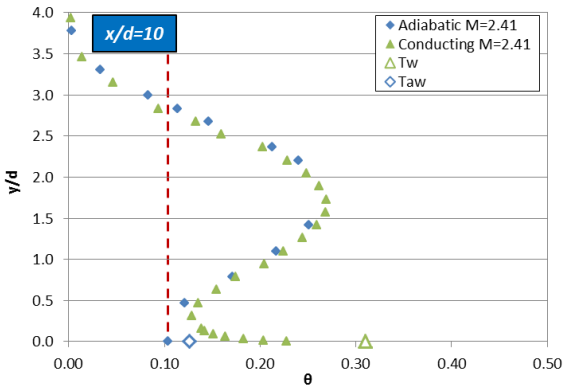

Figure 3.24: Centerline profiles of θ, z/d = 2, x/d = 10, M = 2.41

Chapter 4: Effects of TBC Thickness on Cooling Effectiveness

The experiments measuring the overall and external cooling effectiveness with a simulated thermal barrier coating (TBC) were made on the UTSR vane coated in cork. The experiments were organized into three configurations: one with no film cooling, one with a row of round holes on the pressure side with three rows of showerhead cooling on the leading edge, one with round holes embedded in a realistic trench on the pressure side of the turbine vane. These configurations were tested with blowing ratios $M = 0.5 – 5.0$ from the pressure side row of holes. All blowing ratios reported as *Mps* indicate the coolant flow from the pressure side holes, and those reported as *Mshd* indicate the coolant flow from the showerhead cooling, unless otherwise indicated. All plots report effectiveness versus *s/d*, which is distance from the stagnation line non-dimensionalized by the cooling hole diameter. Negative values of *s/d* indicate the pressure side of the vane model, and positive values of *s/d* indicate the suction side of the vane model.

4.1. No Film Cooling

Figure 4.1 presents the overall effectiveness, ϕ, across the vane surface for the thick TBC of Davidson et al. (2012) with $t/d = 1.0$, the no TBC case of Dees et al. (2013), and the results of this study with TBC thickness $t/d = 0.6$. Recall that for the vane tests with TBC, the overall effectiveness, ϕ, was the measurement of the interface temperature between the TBC and vane wall, and the external effectiveness, τ, was the measurement of the external surface temperature of the TBC. The addition of TBC, $t/d = 0.6$, showed a significant improvement in overall effectiveness over the uncoated vane model of $\Delta\phi \approx 0.25$ across the most of the vane surface, doubling the cooling effectiveness in many locations without additional coolant mass flow rate. This was consistent with Davidson et

al. (2012), who saw a significant increase in overall effectiveness, or a decrease in the vane metal temperature, with the addition of TBC compared to the results of Dees et al. (2013) without TBC. The three datasets in Figure 4.1 were essentially parallel to one another. The increase in ϕ from the no TBC case to the t/d = 0.6 case was $\Delta\phi \approx 0.25$, and the increase in ϕ from the no TBC case to the t/d = 1.0 case was $\Delta\phi \approx 0.35$. The thermal resistance of the TBC with t/d = 0.6 was 35% less than the thermal resistance of the TBC with t/d = 1.0, which was similar to the 30% decrease in the added overall cooling effectiveness from adding TBC t/d = 1.0 vs. adding the TBC t/d = 0.6 to the vane model.

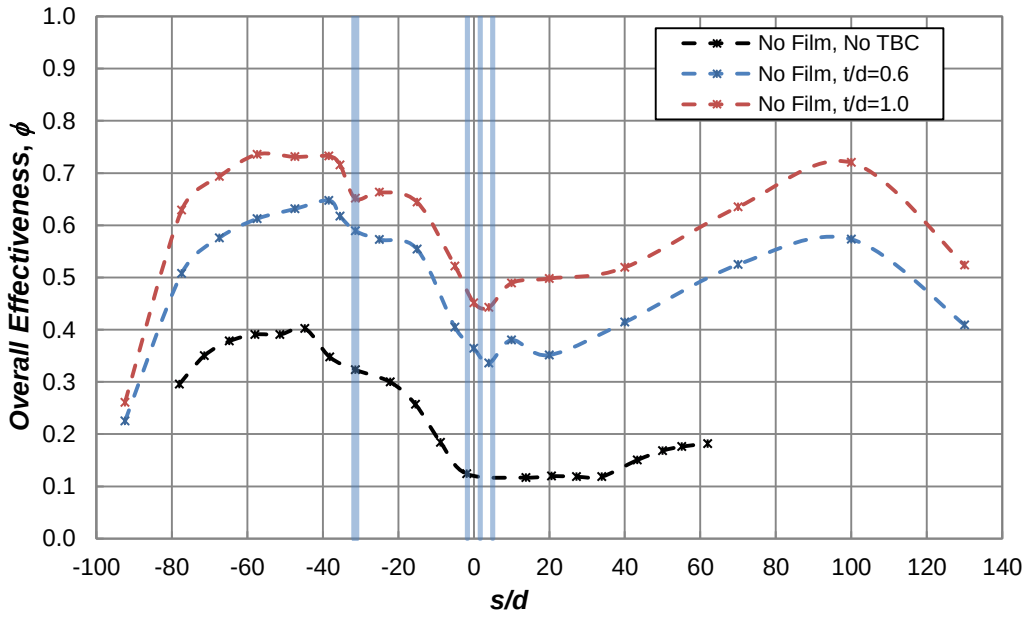

Figure 4.1: Overall effectiveness, ϕ, with only internal convection cooling for TBC with t/d = 0.6, t/d = 1.0 (Davidson, et al., 2012), and no TBC (Dees, et al., 2012)

4.2. Pressure Side Round Holes

Figure 4.2 presents the overall effectiveness, ϕ, with no film cooling, and pressure side round holes with three rows of showerhead cooling. The figure indicates the location of the round holes and showerhead holes with the light blue vertical lines on the

graph. There was a significant increase in ϕ in the showerhead region of the vane with film cooling, with effectiveness values as high as 0.8 for M_{shd} = 3.2. Even for M_{shd} = 0.8, the lowest blowing ratio, $\phi \approx 0.69$ while without film cooling $\phi \approx 0.35$ on the leading edge of the vane. Adding TBC with t/d = 0.6 to the vane model tripled the overall effectiveness on the leading edge without film cooling, and then with the addition of film cooling, the overall effectiveness double. These strong improvements with showerhead cooling are discussed further in Section 4.4 Showerhead Cooling.

Figure 4.2 shows an increase of $\Delta\phi$ = 0.1 near s/d = -25 which is upstream of the pressure side film cooling holes and far downstream of the showerhead cooling holes. The added cooling effectiveness from showerhead blowing had decayed by $s/d \approx$ -20, so the sudden increase in ϕ near s/d = -25 was the result of convective cooling inside the cooling holes, and the conduction of this cooling upstream of the holes. The in-hole convective cooling had its greatest improvement at the location of the holes, s/d = -31.4, where ϕ increased by 0.19 for M_{ps} = 3.0. Even the lowest blowing ratio, M_{ps} =1.0, showed an increase in ϕ of 0.15 at the location of the holes. In Figure 4.3, the contour plots of external effectiveness, τ, showed the increased cooling effectiveness from in-hole convection as well. For all blowing ratios, τ was great between s/d = -25 to -30, which can only be attributed to internal cooling upstream of the coolant holes.

Immediately downstream of the pressure side round holes, the overall effectiveness dropped off, and at s/d = -47.4, the overall effectiveness with film cooling had collapsed to the no-film cooling value. Figure 4.4 zooms in on the region near the pressure side round holes. In Figure 4.4, M_{ps} = 3.0 showed the highest ϕ at the location of the holes, but M_{ps} = 1.0, had the highest effectiveness just downstream of the row of holes at s/d = -35.4. In fact, the ranking of lowest to highest effectiveness by blowing

ratio switches from s/d = -31.4 to s/d = -35.4. This indicated that the in-hole convection dominated the cooling effectiveness at the location of the holes, but immediately downstream of the holes the increased heat transfer coefficient had the dominating effect on the cooling effectiveness.

The contour plots of external effectiveness in Figure 4.3, or the non-dimensionalized TBC temperature, explain why the lower blowing ratios had higher overall effectiveness downstream of the row of holes. For M_{ps} = 1.0, there were streaks of high τ downstream of the film cooling holes, implying the film cooling jets were attached to the vane surface, and τ was increased downstream of the coolant holes compared to upstream of the holes. There were clear streaks of cooling effectiveness downstream of the holes for M_{ps} = 1.0. However, for $M_{ps} \geq 1.5$, τ decreased downstream of the film cooling holes which indicates that the film cooling jets were separated from the vane surface. The separated jets and low τ values downstream of the film cooling holes caused the warmer metal temperatures and lower ϕ values.

The contour plots of τ in Figure 4.3 showed increased levels of τ far downstream of the film cooling holes for M_{ps} = 1.5, 2.0 and 3.0 indicating the separated film cooling jets reattached to the vane surface near $s/d \approx$ -50. Jet reattachment increased the overall effectiveness in Figure 4.4 at s/d = -57.4 for M_{ps} = 1.5, 2.0 and 3.0. Coolant jet separation and reattachment were observed for pressure side round holes on an adiabatic C3X vane model by Albert et al. (Albert, et al., 2011).

A comparison of overall effectiveness for the vane model with film cooling, M_{ps} = 2.0, between TBC t/d = 0.6, TBC t/d = 1.0, and no TBC is given in Figure 4.5. The no TBC and TBC t/d = 1.0 cases also showed increased overall effectiveness in the showerhead, upstream of the pressure side round holes, and at the location of the pressure

side round holes. However, the no TBC overall effectiveness improved greatly downstream, $\Delta\phi$ =0.1, of the pressure side round holes with film cooling which was not observed in the two cases with TBC where $\Delta\phi$ = 0.03. It was hypothesized that the thinner TBC, *t/d* =0.6, would begin to see greater improvements with film cooling when compared to the thicker TBC, *t/d* = 1.0, but the insulating layer of TBC still dominated over the film cooling effectiveness. Also, the overall effectiveness with film cooling for the no TBC case was only higher than the TBC *t/d* = 0.6 without film cooling in the showerhead region. TBC was capable of significantly improving the cooling effectiveness without increasing the mass of coolant used.

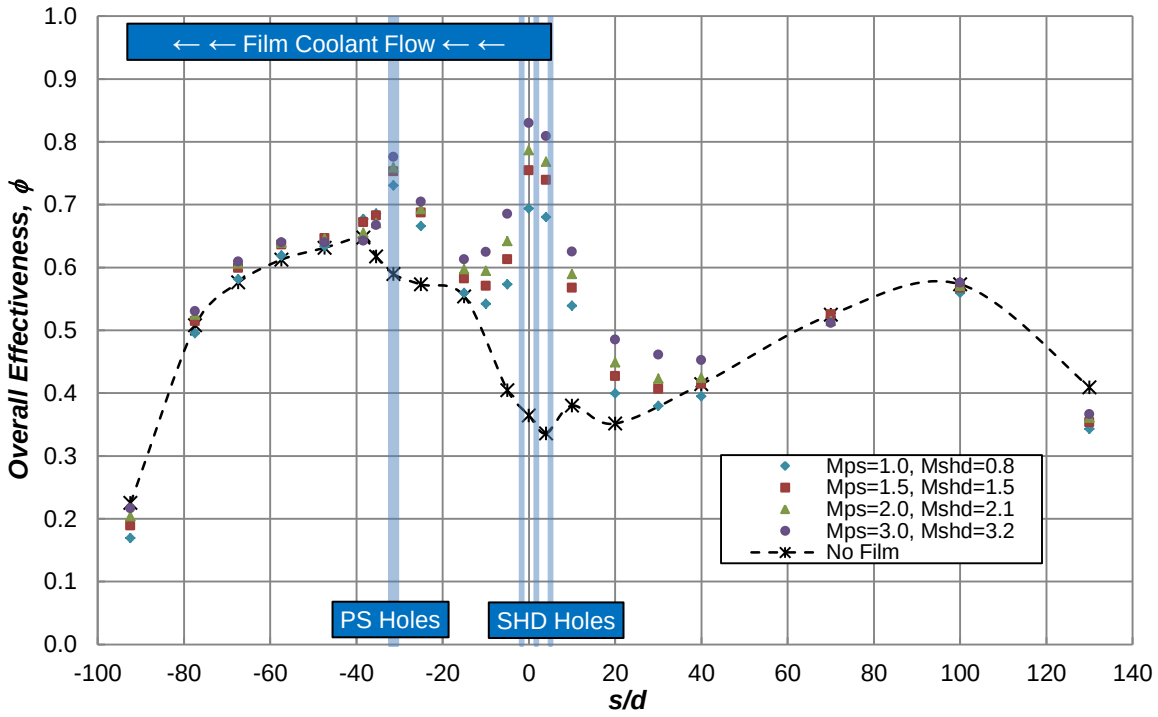

Figure 4.2: Overall effectiveness, ϕ, with TBC, *t/d* = 0.6, with showerhead and pressure round holes

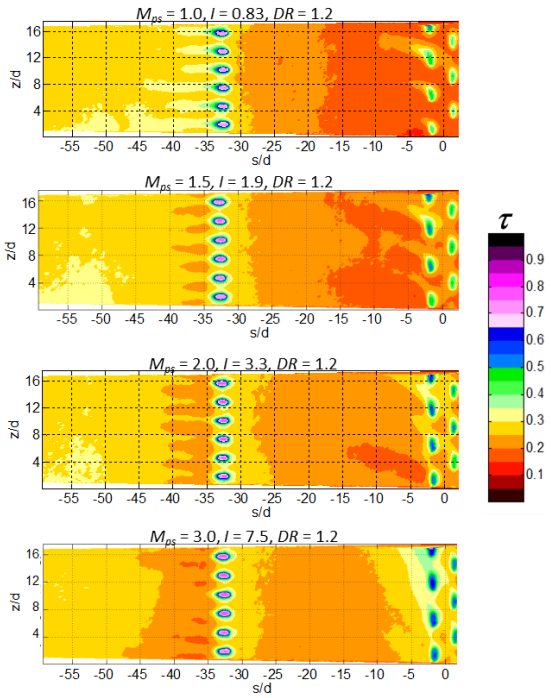

Figure 4.3: Contour plots of external effectiveness, τ, with pressure side round holes and showerhead blowing, TBC thickness t/d = 0.6

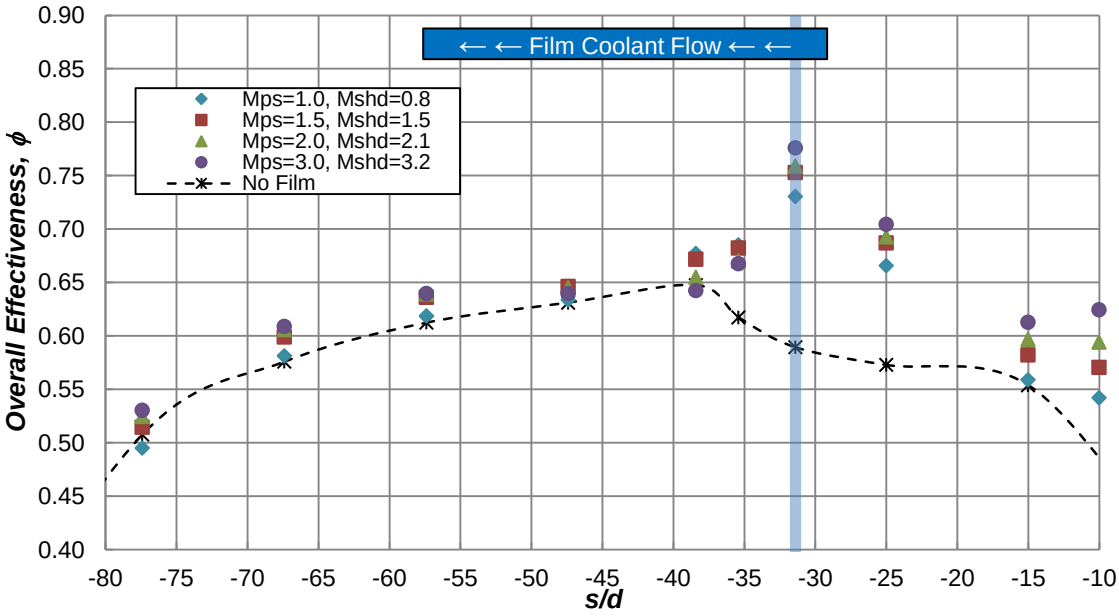

Figure 4.4: Overall effectiveness, ϕ, with TBC, t/d = 0.6, with showerhead and pressure round holes

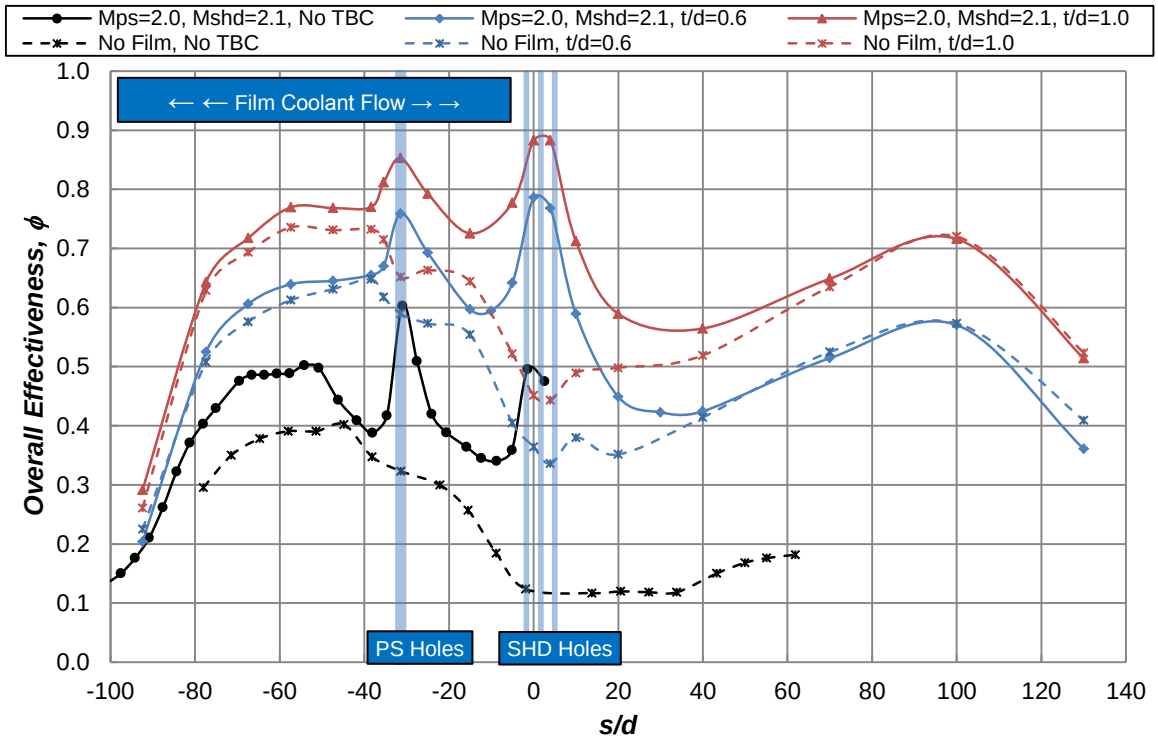

Figure 4.5: Overall effectiveness, ϕ, for showerhead and round hole blowing with no TBC (Dees, et al., 2013), TBC t/d = 1.0 (Davidson, et al., 2012), and TBC t/d = 0.6

4.3. Pressure Side Realistic Trench

Trenched film cooling has been shown to greatly increase adiabatic effectiveness, and the work of Kistenmacher et al. (2013) showed a trench embedded in the TBC helped significantly increase external (Albert, et al., 2011) (Kistenmacher, et al., 2013). Therefore, a realistically machineable trench was cut into the TBC around the pressure side round holes to investigate the effects of improving the film cooling effectiveness. The overall effectiveness results with pressure side trenched round holes and no showerhead blowing for M_{ps} = 0.5, 1.0, 2.0, 3.0, and 5.0 are presented in Figure 4.6 shows the location of the trench at s/d = -31.4, the same location of the round holes discussed in the previous section.

The effect of in-hole convection was seen upstream of the trench just as it was seen upstream of the round holes in that there were high levels of ϕ at s/d = -25. However, unlike the round holes that showed even higher levels of ϕ at the location of the holes, the realistic trench had a significant drop in ϕ at the location of the holes. The values of ϕ decreased to levels lower than the no film cooling line. The round holes had TBC covering and insulating the area between the holes where the vane surface was completely exposed to the hot mainstream gas in the trench. Similar to the round holes results, however, ϕ was highest immediately downstream of the holes for M_{ps} = 1.0. Further downstream (s/d > 45), the coolant jets at higher blowing ratios, M_{ps} = 2.0 and 3.0, have higher overall effectiveness most likely because the jets are reattaching to the vane surface.

Contour plots of external effectiveness, τ, with the pressure side trench for M = 0.5, 1.0, 2.0, 3.0 and 5.0 are given in Figure 4.7. The IR camera measured temperature helped confirm and explain the warm temperatures (low ϕ) seen inside the trench. The effectiveness measured inside the trench was the overall effectiveness because there was no TBC, and this was the case. Both the TC embedded in the trench and the IR camera measured effectiveness values between 0.55 and 0.60 at s/d = -31.4.

The contour plots of τ revealed that the coolant was not pooling inside the trench and then spilling over as a uniform covering as it was intended. The goal of trenched film cooling is to replicate slot film cooling when using discrete holes, but Figure 4.7 shows the film cooling remained as discrete jets. Dorrington et al. (2007) studied several trench depths with recessed walls to find a threshold for a minimum trench height for effective trenched film cooling and found t/d needed to be larger than 0.75 for the trench to allow the coolant to pool and spill over. The trench in this study was embedded in the TBC, and

the TBC thickness was t/d = 0.6 which was less than the threshold found by Dorrington et al. The shallow trench height explains why discrete coolant jets were seen in the contour plots of τ instead of a uniform flow.

The highest of levels of τ were downstream of the trench for M_{ps} = 1.0 which was consistent with the highest levels of ϕ. However, while the higher levels of external effectiveness for M_{ps} = 1.0 than for M_{ps} = 2.0 did yield higher levels of overall effectiveness, the improvement in overall effectiveness was very small because the insulating presence of TBC decouples the relationship between film cooling improvements and metal temperature improvements. The higher blowing ratios, M_{ps} = 2.0 and 3.0, were separated from the vane surface just downstream of the trench but reattached further downstream by s/d = -45 and -50 respectively. The contour plot of τ for M_{ps} = 5.0 did not show the coolant jet reattaching to the vane surface, so it was likely the jet was too far separated to reattach to the vane surface. The external effectiveness decreased downstream of the trench between the cooling holes for M_{ps} = 2.0, 3.0, and 5.0, and this was most likely the result of increase heat transfer coefficients due to the separated jets.

Figure 4.8 compares the overall effectiveness results with the realistic trench between the TBC t/d = 0.6 and TBC t/d = 1.0 for M =2.0. The overall effectiveness with the thicker TBC show significant improvement over the no film cooling line at the location of the trench and downstream which stood in contrast to the results from the thinner TBC. The round holes showed only minimal improvement over the no film cooling case for the thicker TBC in Figure 4.5, but the realistic trench caused an increase of 0.1 in overall effectiveness downstream of the trench. Contour plots of τ comparing the thicker and thinner TBC with realistic trenches are shown in Figure 4.9 for M = 2.0.

When compared to the thicker TBC, it was made the clear the shallower trench, $t/d = 0.6$, did not perform nearly as well as the realistic trench in the thicker TBC. The higher film effectiveness obtained with the thicker TBC resulted in significantly increased ϕ values when film cooling was used with the thicker TBC.

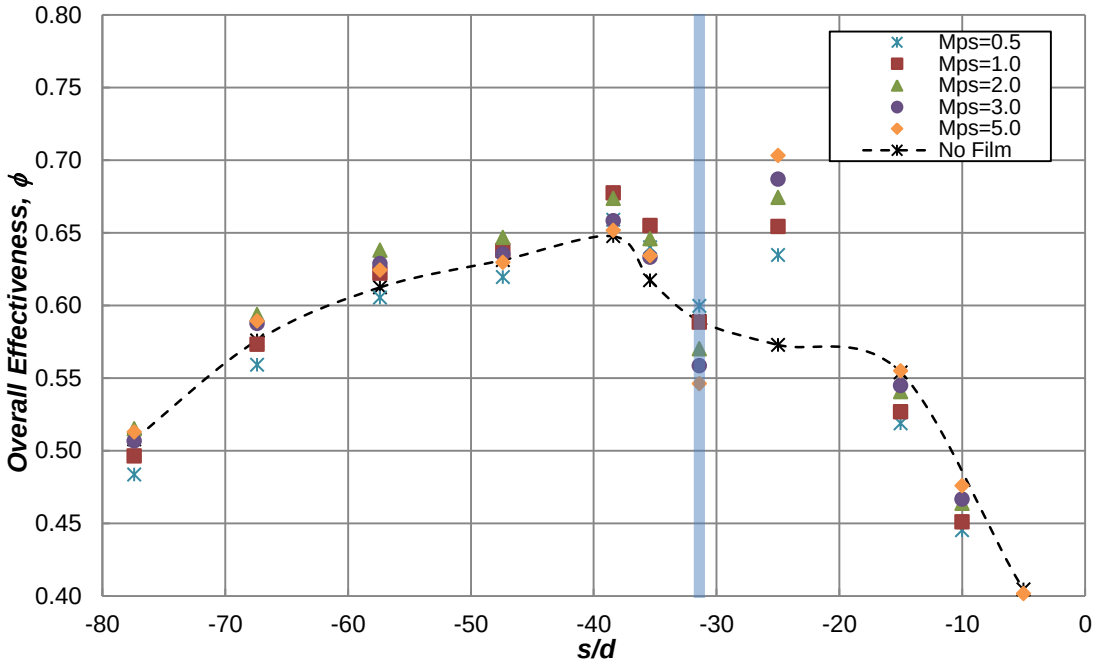

Figure 4.6: Overall effectiveness, ϕ, with a pressure side realistic trench and no showerhead blowing, $t/d = 0.6$

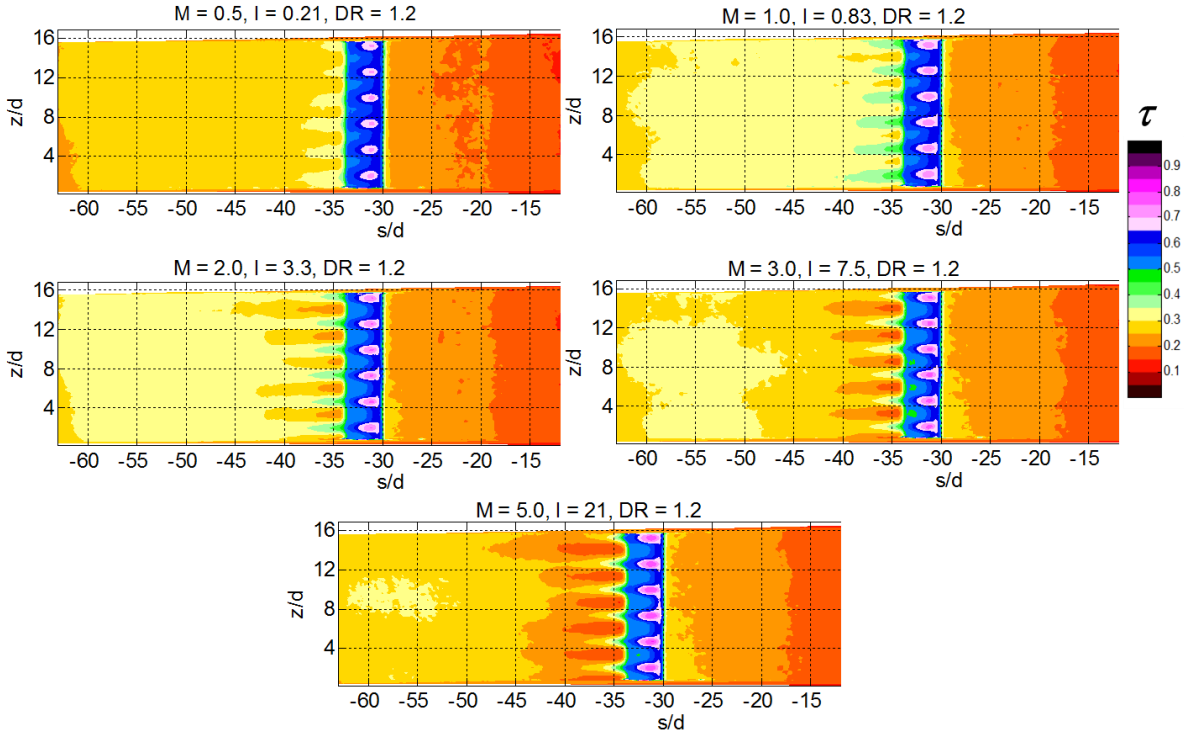

Figure 4.7: Contour plots of external effectiveness, τ, with the pressure side realistic trench, *t/d* = .6

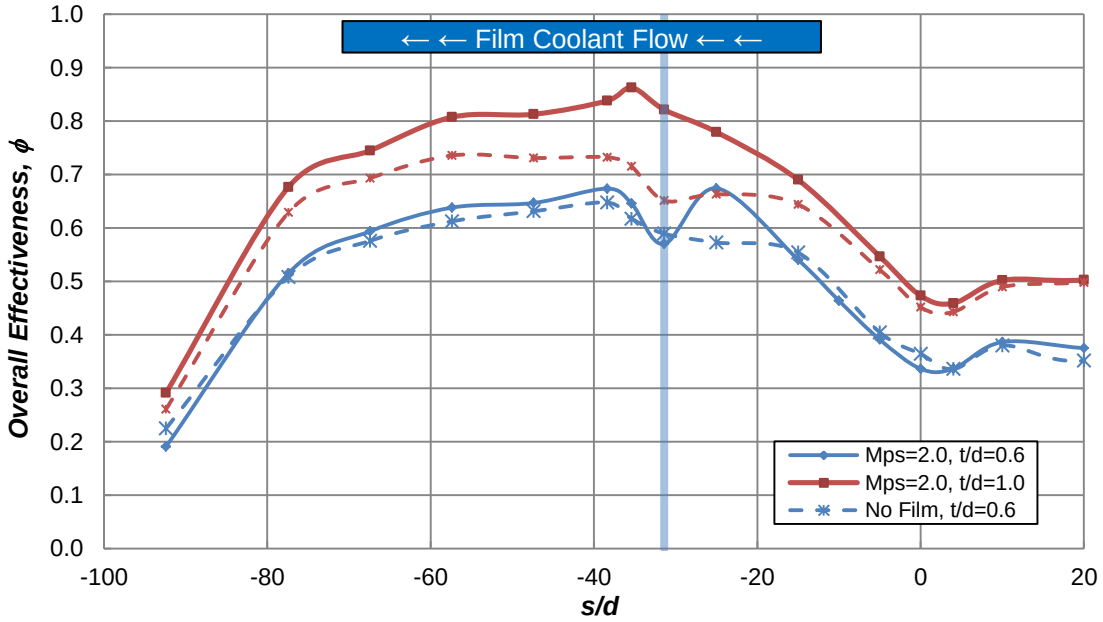

Figure 4.8: Overall effectiveness, ϕ, with the pressure side realistic trench for TBC *t/d* = 0.6 compared to TBC *t/d* = 1.0 (Davidson, et al., 2012)

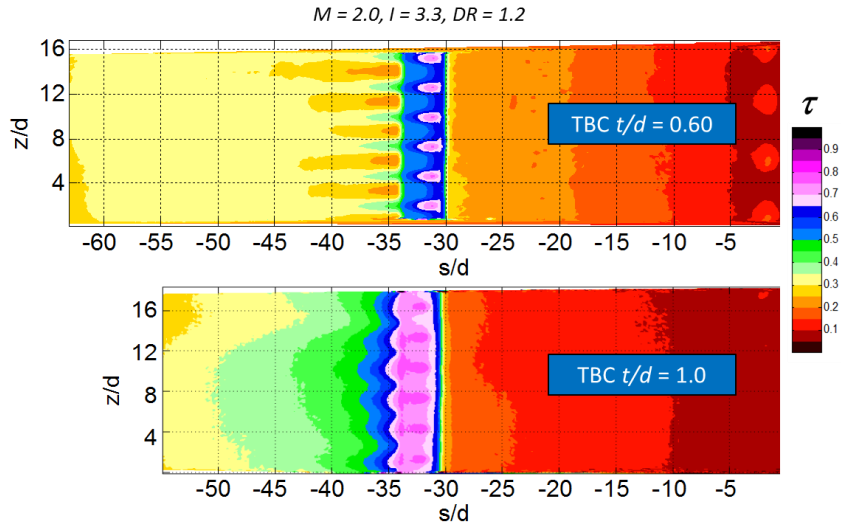

Figure 4.9: Contour plots of external effectiveness, τ, comparing TBC *t/d* = 0.6 and TBC *t/d* =1.0 (Davidson, et al., 2012)

4.4. SHOWERHEAD COOLING

The showerhead of film cooling holes on the leading edge of the vane yielded the greatest improvement in overall effectiveness with the addition of TBC and film cooling. Before TBC and film cooling, the leading edge was the warmest region of the vane, but with TBC and film cooling it becomes one of the most effectively cooled areas. Figure 4.10 shows that the overall effectiveness increased monotonically with blowing ratio with ϕ measurements above 0.80. This trend of increasing effectiveness with increasing blowing ratio was consistent with previous studies of showerhead cooling on the leading edge (Albert, et al., 2011) (Nathan, et al., 2012). Figure 4.3 showed increasing levels of external effectiveness with blowing ratio in the showerhead which corresponds to the increasing levels of overall effectiveness. Additionally, the showerhead was composed of 96 coolant holes resulting in high levels of in-hole convection. The ever-increasing

overall effectiveness in the TBC coated showerhead with blowing ratio stood in contrast to the results on the pressure side of the vane where increased blowing ratios did not yield significant increases in overall effectiveness.

The combined result of film cooling and TBC in the showerhead region is highlighted in Figure 4.11 where overall effectiveness data in the showerhead with and without TBC is presented. The improvements in overall effectiveness with blowing were almost equivalent between the no TBC and TBC t/d = 0.6 vane models. The increase in ϕ from the no film cooling data to the measurements with M_{shd} = 0.8 was $\Delta\phi$ = 0.30 for both the TBC coated vane and the uncoated vane. Further, the increase in ϕ from M_{shd} =0.8 to 2.1 was 0.10 for both vane models, and the increase in ϕ from M_{shd} = 2.1 to 3.2 was 0.05 for both vane models. The large increases in ϕ in the showerhead with TBC were the combined result of in-hole convection and increased film effectiveness.

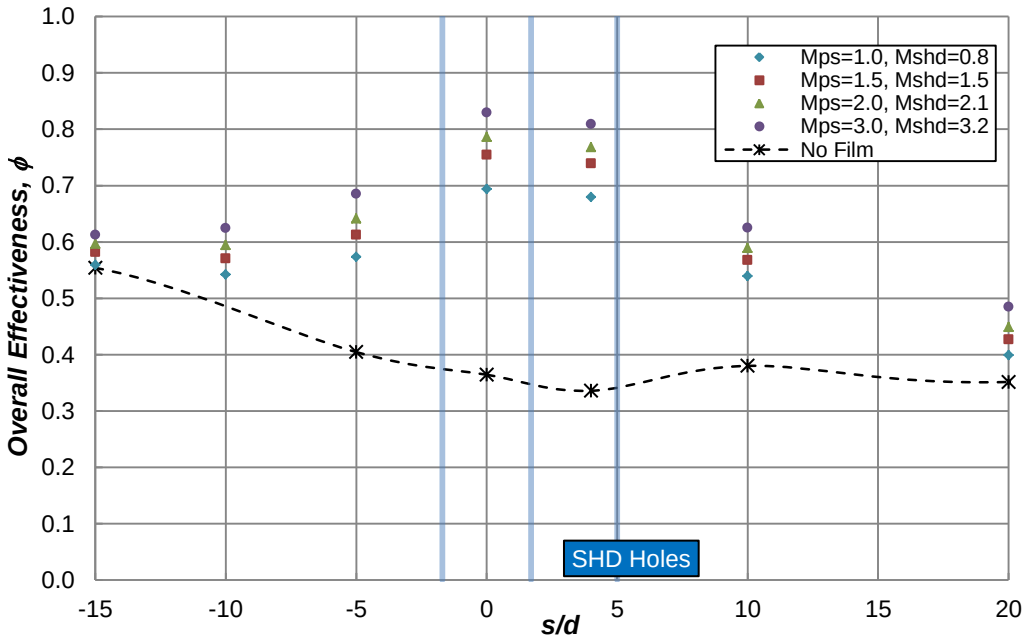

Figure 4.10: Overall effectiveness, ϕ, in the showerhead region with TBC t/d = 0.6

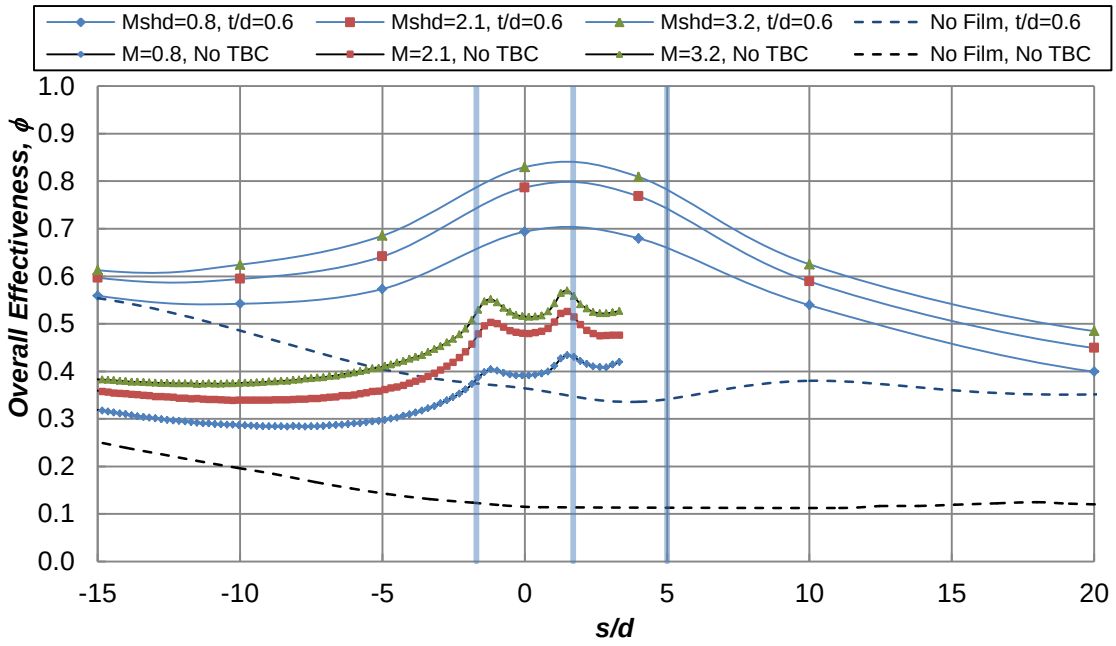

Figure 4.11: Overall effectiveness, ϕ, in the showerhead region for no TBC (Dees, et al., 2013) and TBC t/d = 0.6

4.5. Overall Effectiveness Prediction Analysis

The similar shape of the three sets of overall effectiveness measurements for the no TBC, TBC t/d = 0.6, and TBC t/d = 1.0 in Figure 4.1 prompted a 1-D heat transfer analysis to predict the improvement in cooling effectiveness with TBC. Additionally, the analysis to predict the cooling effectiveness with thicker TBC from the thinner TBC overall effectiveness data was performed. This analysis used the heat transfer coefficient measurements on the C3X vane model from Dees et al. (2013) and thermal conductivity measurements of the Corian and cork discussed in Section 2.4.

4.5.1. Derivation

A 1-D thermal circuit model for the heat transfer through the vane wall is pictured in Figure 4.12 showing the thermal resistances of each layer. The thermal resistance of

each level was needed to predict the overall effectiveness: the thermal resistance from internal convection, the vane wall, the TBC, radiation from the external vane surface, and external convection. With the measurements of Dees et al., (2013) only the internal heat transfer coefficient and radiation were unknown, so the overall effectiveness measurements with no TBC were used to solve for the internal heat transfer coefficient, and radiation heat transfer was assumed to be negligible. The entire analysis was done including and ignoring radiation heat flux, and the difference was found to be very small, $\Delta\phi$ = 0.01 – 0.03. A second analysis is shown in the next section that predicts the overall effectiveness with thick TBC and calculating the internal heat transfer coefficient using the thin TBC overall effectiveness data. For this case, the external surface temperature of the TBC was unknown and radiation could not be corrected for; therefore, because radiation effects were small, they were ignored in both analyses. First, the heat flux through the vane wall was found using the mainstream temperature, the vane wall temperature, and the external heat transfer coefficient shown:

$$q''_{no\,TBC} = \frac{T_\infty - T_{v,no\,TBC}}{R_{conv,ext}} \tag{4.1}$$

where $T_\infty$was the mainstream gas temperature, $T_{v,no\,TBC}$ was the surface temperature of the vane, and $R_{conv,ext}$ was the heat transfer coefficient between the external vane surface and the mainstream. In the second analysis, where the overall effectiveness with the thicker TBC was predicted using the overall effectiveness from the thinner TBC, Equation 4.2 uses $T_{v,TBC}$, which was the temperature of the vane surface beneath the TBC. Then, the calculated heat flux, mainstream temperature, coolant temperature, vane wall resistance, and external heat transfer coefficient were used to determine the internal heat transfer coefficient of the vane:

$$R_{conv,int} = \frac{T_\infty - T_c}{q''_{no\,TBC}} - R_{wall} - R_{conv,ext} \tag{4.2}$$

where T_c was the temperature of the coolant inside the vane and R_{wall} was the thermal resistance of the vane wall from the thermal conductivity and the thickness. The coolant temperature was linearly interpolated from the U-bend inlet to the U-bend outlet to find the local coolant temperature. The interpolation was performed for every position for which there was a surface thermocouple on the external surface of the vane. Now, using the mainstream and coolant temperatures, and the known thermal resistances for all parts of the thermal circuit in Figure 4.12, the heat flux through the vane surface was calculated:

$$q''_{TBC} = \frac{T_\infty - T_c}{R_{conv,int} + R_{wall} + R_{TBC} + R_{conv,ext}} \tag{4.3}$$

where R_{TBC} was the thermal resistance of the TBC. Finally, the heat flux at each *s/d* position, along with the mainstream temperature and the thermal resistances of the vane wall and TBC on the vane was used to calculate the temperature on the vane surface:

$$T_{v,TBC} = T_\infty - q''_{TBC}\left(R_{conv,ext} + R_{TBC}\right) \tag{4.4}$$

The vane surface temperature allowed the overall effectiveness values to be calculated for the given TBC thermal resistance using Equation (1.5).

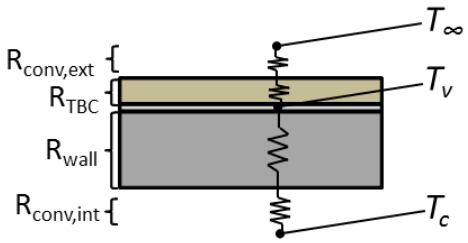

Figure 4.12: Thermal resistance circuit for the overall effectiveness prediction equations

4.5.2. Prediction Results

The first results from the prediction analysis are presented in Figure 4.13 which shows the overall effectiveness with no TBC, TBC t/d = 0.6, and the predicted overall effectiveness data with TBC t/d = 0.6 from the no TBC data. The prediction accounted for 80% of the improvement in ϕ when adding TBC, but under-predicted the improvement for all s/d locations. However, there was a region near the leading edge, -5 $\leq s/d \leq$ 20, where the predicted and measured overall effectiveness data agree within the uncertainty bands. The uncertainty in the predicted ϕ results was much higher than the measured data because of the uncertainty in the temperature measurements from the IR camera. The discrepancy between the predicted and measured ϕ values may be attributed to the 1-D heat transfer assumption which does not account for lateral or streamwise conduction.

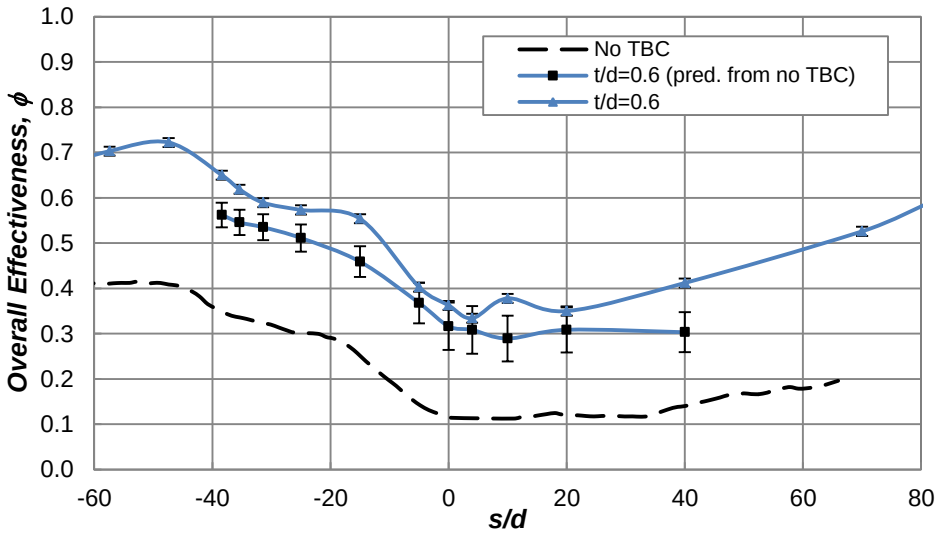

Figure 4.13: Predicting the overall effectiveness with TBC t/d = 0.6 from the no TBC (Dees, et al., 2013) overall effectiveness data with no film cooling

An alternative prediction is shown in Figure 4.14, where the overall effectiveness for the vane with the thicker TBC was predicted using the data for the vane with the

thinner TBC. In this analysis the vane wall temperature under the TBC was used to calculate the heat flux similar to Equation (4.1):

$$q''_{no\,TBC} = \frac{T_\infty - T_{v,\,thinner\,TBC}}{R_{conv,ext} + R_{thinner\,TBC}} \tag{4.5}$$

with the external heat transfer coefficient as well as the TBC thermal resistance. The TBC thermal resistance was added to the right side of Equation (4.2) to find the internal heat transfer coefficient:

$$R_{conv,int} = \frac{T_\infty - T_c}{q''_{no\,TBC}} - R_{wall} - R_{conv,ext} - R_{thinner\,TBC} \tag{4.6}$$

Then the predicted heat flux was calculated in a similar fashion to Equation (4.3) using the thermal resistance of the thick TBC:

$$q''_{thick\,TBC} = \frac{T_\infty - T_c}{R_{conv,int} + R_{wall} + R_{thick\,TBC} + R_{conv,ext}} \tag{4.7}$$

Finally, the vane surface temperature was found using a similar equation to Equation (4.4) but using the thermal resistance of thicker TBC as opposed to the thinner TBC:

$$T_{v,thick\,TBC} = T_\infty - q''_{TBC}\left(R_{conv,ext} + R_{thick\,TBC}\right) \tag{4.8}$$

The vane surface temperature was then used to calculate the overall effectiveness using Equation (1.5).

The predicted overall effectiveness results for the thick TBC are shown in Figure 4.14. This analysis yielded predicted ϕ values that fell within the uncertainty of the measured ϕ values for all *s/d* locations except for *s/d* = 20. The prediction from one TBC dataset to another was noticeably more successful than the prediction using the no TBC case to predict the thinner TBC dataset. There was a bond coat thermal resistance between the TBC and the vane model that existed in both the TBC configurations and would not have existed in the no TBC case. The thermal resistance of this bond coat

would have been accounted for in the estimation of the internal heat transfer coefficient ultimately yielding the more accurate prediction of overall effectiveness seen in Figure 4.14.

The purpose of the overall effectiveness prediction analysis was to determine whether the effects of TBC on overall effectiveness were easily predictable. If the insulation impact of TBC was predictable, then experiments to simulate TBC are not necessary. The results of this study showed that the effect of TBC was not predictable from a 1-D heat transfer analysis using measurements of overall effectiveness on a vane model without TBC, but using measurements of overall effectiveness with a thicker TBC did give a successful prediction of overall effectiveness. It is important to note that the prediction did not use measurements of overall effectiveness with film cooling. The 1-D assumption is not valid with film cooling because the heat transfer becomes a 3-D problem.

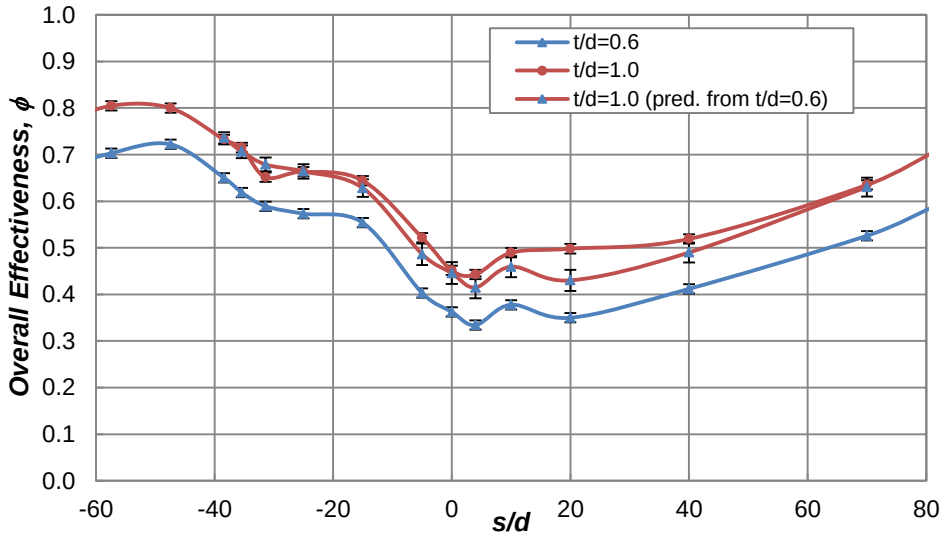

Figure 4.14: Predicting the overall effectiveness with TBC *t/d* = 1.0 (Davidson, et al., 2012) from the TBC *t/d* = 0.6 overall effectiveness data with no film cooling

Chapter 5: Contaminant Deposition

The work of Davidson et al. (2012) studied the effects of contaminant deposition on turbine cooling with the thicker TBC, t/d = 1.0, and this study expands on those experiments to include the effect of deposition on turbine cooling with a thinner TBC, t/d = 0.6. Additionally, this study includes velocity and temperature measurements in the wake of the model turbine vane with and without deposition.

5.1. Deposition Effects on Turbine Cooling with a Realistic Trench

Figure 5.1 shows the leading edge and the pressure side of the vane model with film cooling from the showerhead and realistic trench and the resulting contaminant deposition. The two red circles indicate where the film cooling impacted how the deposition formed on the vane surface. In the showerhead region, the film cooling holes created furrows of reduced deposition in their path while coolant momentum was slowed outside of the coolant holes. The realistic trench had a similar impact on the deposition except the furrows where more exaggerated and almost looked like tunnels. The deposition collected high between the coolant holes near the trench. The height of the deposition in the showerhead region was t = 4.5 mm which was consistent with the deposition experiments of Davidson et al. (2012) with the thick TBC. Additionally, there was little to no deposition on the suction side of the vane seen near the blue circle. Figure 5.2 shows how the level of deposition decreased further from the stagnation line and then down past the trench. Most of the deposition accumulated near the film cooling locations, and between the pressure side trench and the showerhead, the showerhead accumulated more deposition.

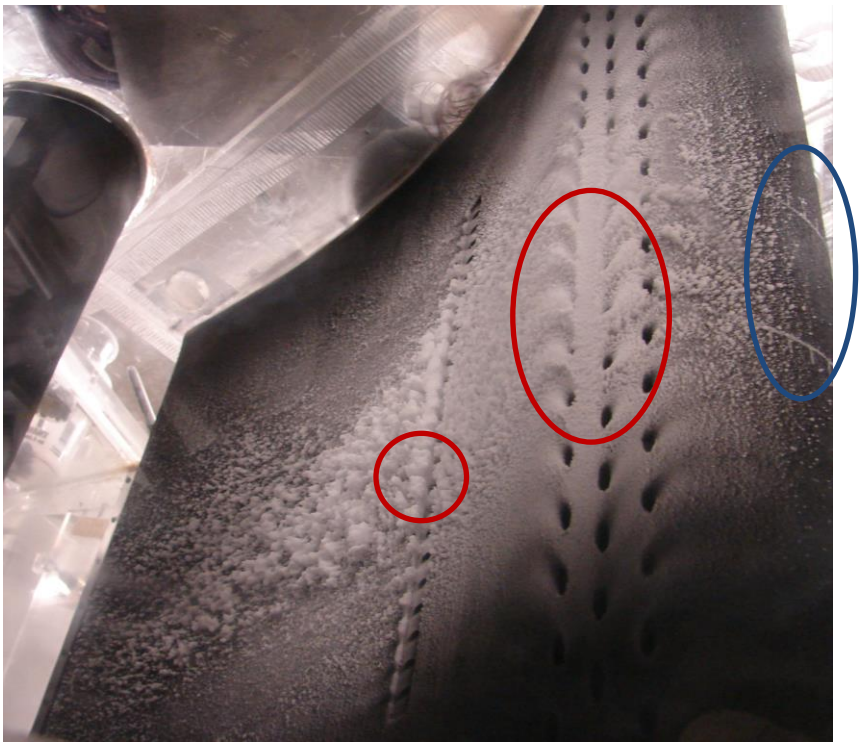

Figure 5.1: Vane model after deposition test viewing the leading edge and pressure side of the vane

Figure 5.2: Image of the pressure side of the vane showing the extent of the deposition

In Figure 5.3 are pictures of the pressure side realistic trench before and after wax spray deposition. In this figure one can see that the deposition tended to develop on the downstream edge of the trench with a maximum thickness, t = 14 mm. Table 5.1 shows

that this phenomenon was consistent with the deposition trends with a trench seen by Kistenmacher et al. (2013) for a realistic width trench cut into thicker TBC, t/d = 1.0 where the maximum deposition thickness was t = 3.8 mm at the location of the downstream edge of the trench (s/d = -34). However, the shallower trench in the thinner TBC accumulated much more deposition (t = 14 mm) than the deeper trench with the thick TBC (t = 3.8 mm). However, these thicknesses do not paint the entire picture. The thick TBC also had a significant accumulation of deposition on the downstream edge of the trench, shown in Figure 5.4(b), but the large accumulation broke off a few minutes after the deposition ended. On the contrary, the accumulation on the downstream edge of the trench in the thinner TBC did not break off. Far downstream of the trench, the thickness of the deposition was nominally equal between the thick and thinner TBC realistic trench cases. It is important to note that the showerhead was no blowing for the thick TBC realistic trench case, so the comparison was limited to downstream of the pressure side coolant holes. Table 5.1 shows the deposition thickness results for other cases with the thick TBC though, and the deposition thickness on the leading edge with showerhead blowing was consistent between the two TBC cases. This was likely because the geometric configuration of the showerhead holes was unchanged between the two thicknesses of TBC. Additionally, the external effectiveness, or TBC surface temperature was roughly equivalent between the two thicknesses TBC in the showerhead region, $\phi \approx$ 0.25, and the equivalent surface temperature would result in similar levels of deposition sticking.

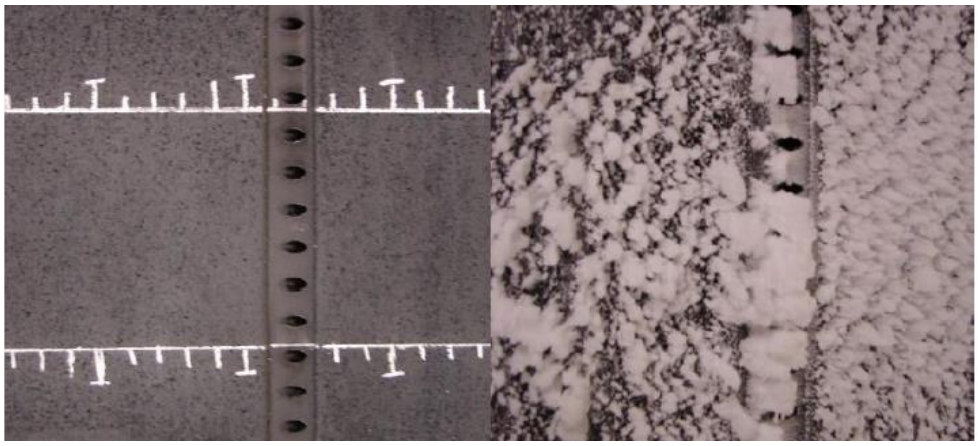

Figure 5.3: Pressure side realistic trench with and without deposition

Table 5.1: Thicknesses of contaminant deposition at various vane locations for the thick and thinner TBC

	Deposition Thickness (mm)					
TBC	**s/d**	**0**	**-17**	**-34**	**-44**	**M**
t/d = 1.0	**No Film**	2.5	3.8	5.1	5.1	**0**
t/d = 1.0	**Round**	2.5	3.8	10.2	5.1	**0.7**
t/d = 1.0	**Round +SHD**	4.6	5.1	13.2	6.4	**2.0**
t/d = 1.0	**Realistic Trench**	1.8	2.5	3.8	2.5	**2.0**
t/d = 0.6	**Realistic Trench + SHD**	4.5	5	14	2	**2.0**

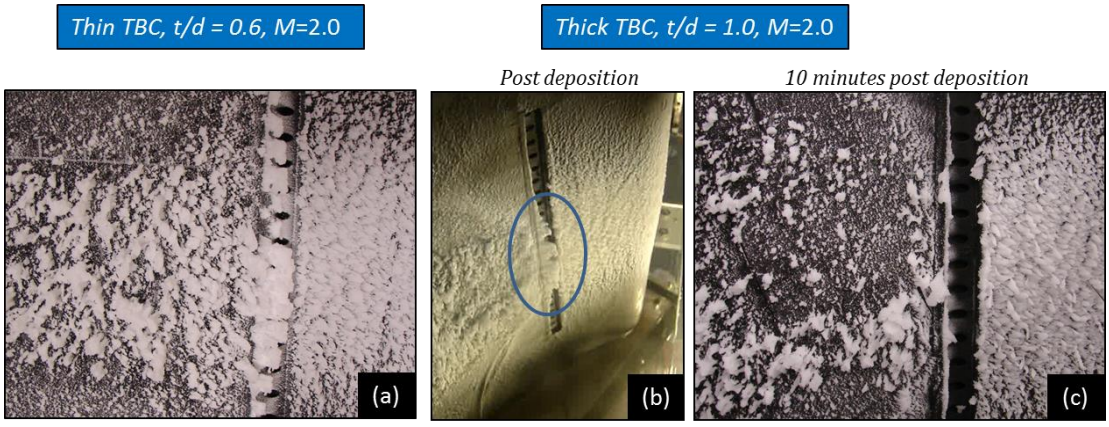

Figure 5.4: Comparison of contaminant deposition for thinner and thick TBC with pressure side realistic trench

Overall effectiveness measurements with and without deposition are given in Figure 5.5. The suction side of the vane showed no change in overall effectiveness with and without deposition because no wax formed on the suction surface. The consistency of measurements for $s/d > 40$ provided a good check on the repeatability of measurements.

Accumulated deposition was expected to both increase the heat transfer coefficient because of increased surface roughness, which would decrease ϕ, and insulate the vane surface, which would increase ϕ. Figure 5.5 shows the overall effectiveness either increased or was unchanged with deposition at all locations on the vane surface. The showerhead region had overall effectiveness increased by $\Delta\phi = 0.07$ proving that the insulating protection the deposition dominated over the increased turbulent mixing and heat transfer coefficient. Additionally, the deposition lowered the momentum of the coolant on the pressure side helping to keep it attached to the vane surface in the showerhead region.

The location of the coolant holes on the pressure side showed the greatest improvement in overall effectiveness with deposition because the trench had previously exposed the vane surface to the mainstream gas, but the trench was now protected by a layer of deposition. Additionally, the trench was previously too low to slow the momentum of the coolant down and allow it to spill over in a uniform layer, and now the deposition had essentially created a high deposition wall which slowed the momentum of the coolant down. This is not to say the coolant was uniform, with deposition, but that the coolant could now adequately collect and protect the exposed vane surface in the trench.

Contour plots of external effectiveness, τ, are shown in Figure 5.6, and provide indications of the level of film cooling effectiveness. The region between $s/d = 0$ and -30 had much lower levels of τ with deposition than without deposition. This was the result of

decreased film cooling effectiveness because of the increased surface roughness, increased external heat transfer coefficient due to surface roughness, and greater insulation thickness due to the wax layer. However, just downstream of the location of the trench the external effectiveness increased because the film coolant coming from the trench was cooling the deposition in that region and there was less separation between the coolant flowing through the wax channels. The colder deposition near the trench also explained why the highest levels of deposition occurred there. The cold deposits on the vane solidified the wax particles impacting the vane surface keeping them attached.

Figure 5.7 shows a comparison of the overall effectiveness with the realistic trench and showerhead cooling, with and without deposition, between the thicker TBC *t/d* = 1.0 and the thinner TBC *t/d* =0.6. The thicker TBC also showed an increase in overall effectiveness with deposition in the showerhead region and on the pressure side of the vane because the insulating protection had a greater impact than the increased heat transfer coefficient. However, the increase in ϕ was not as great as the increase in ϕ measured on the thinner TBC vane. This highlighted the magnitude of the detrimental effects of the shallow trench with the thinner TBC by showing how great the improvement in cooling was with deposition in the trench.

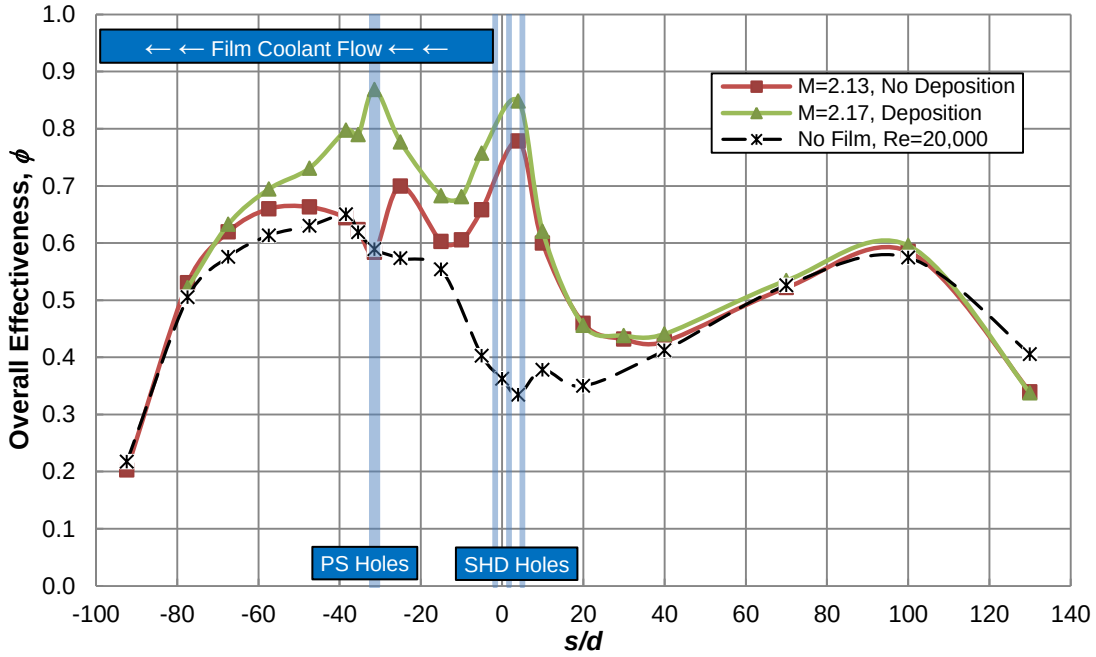

Figure 5.5: Overall effectiveness with pressure side realistic trench and showerhead cooling; with and without deposition; TBC *t/d*=0.6, *M*=2

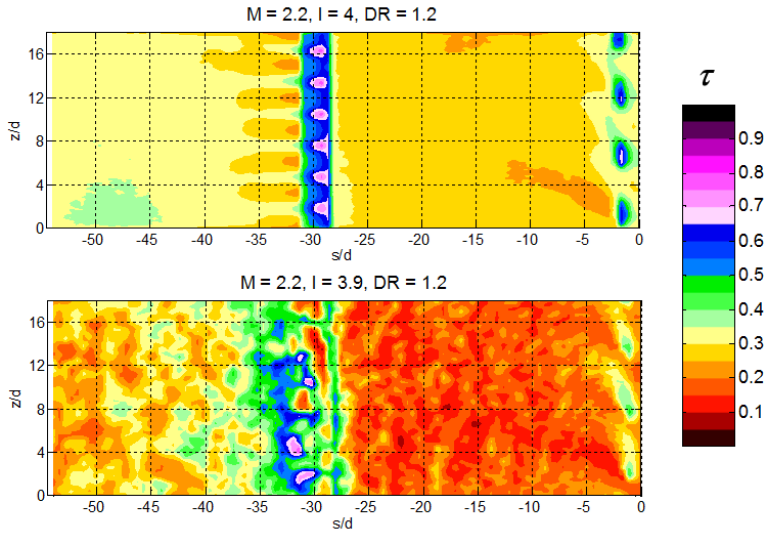

Figure 5.6: External effectiveness with pressure side realistic trench, with and without deposition, TBC *t/d*=0.6, *M*=2.2

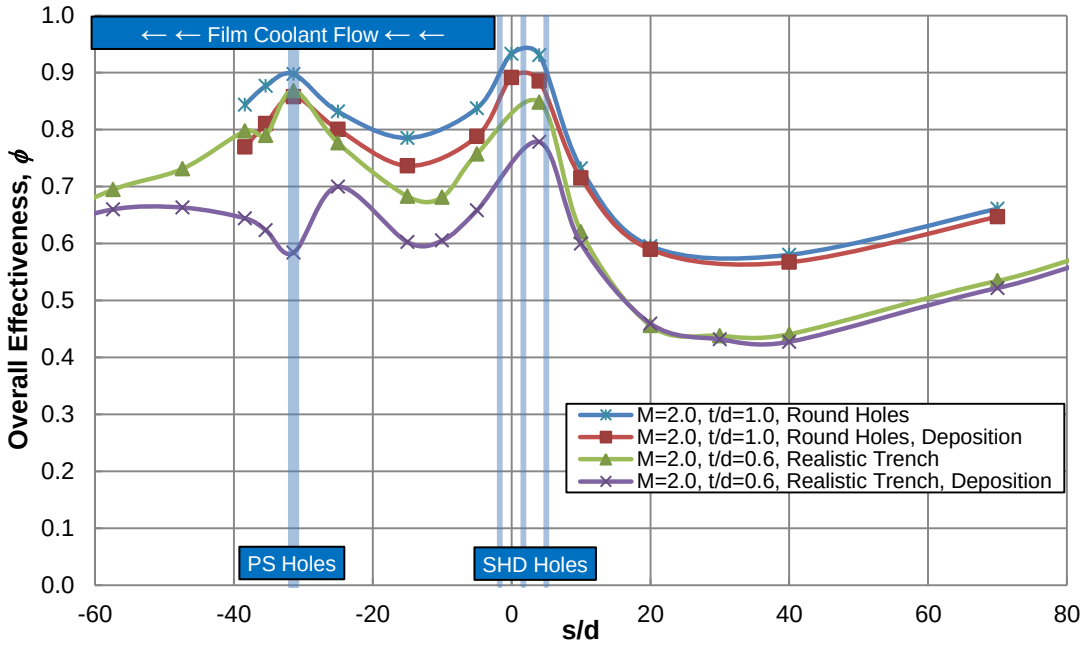

Figure 5.7: Overall effectiveness with pressure side realistic trench and showerhead cooling; with and without deposition; TBC *t/d*=0.6 and *t/d*=1.0, *M*=2 (Kistenmacher, et al., 2013)

5.2. WAKE MEASUREMENTS

Measurements of the temperature, total pressure, and static pressure were taken in the wake of the vane, and total pressure was measured upstream of the vane. These measurements were then organized into the velocity deficit, u/U, and wake temperature, θ. These measurements were taken at x/c_a =0.12 in the wake of the vane and across the pitch of the wake from $-0.18 < y/c_x < 0.12$. In this section, regions of the wake will be referred to as the "pressure side" and "suction side" when in fact these measurements were taken in the vane wake not above the vane surface. This nomenclature was simply used to describe which side of the wake was being referenced.

5.2.1. Velocity Deficit

The mean velocity in the wake of the vane is shown in Figure 5.8 for three cases: no film cooling, film cooling (M_{ps} = M_{shd} = 2.0) with a pressure side realistic trench and showerhead blowing, and film cooling (M_{ps} = M_{shd} = 2.0) with wax contaminant depositions. For all cases the transition from the far field velocity on the suction side to the wake velocity was more gradual than the transition from the far field velocity on the pressure side to the wake velocity. The no film cooling and film cooling mean velocity measurements aligned within uncertainty for all locations in the wake. However, the contaminant deposition on the vane surface caused a significantly greater loss, slowing the velocity significantly on the pressure side of the vane. The wake near the suction side of the vane was not greatly impacted by the deposition which was attributed to there being little to no depositions that formed on that side of the vane.

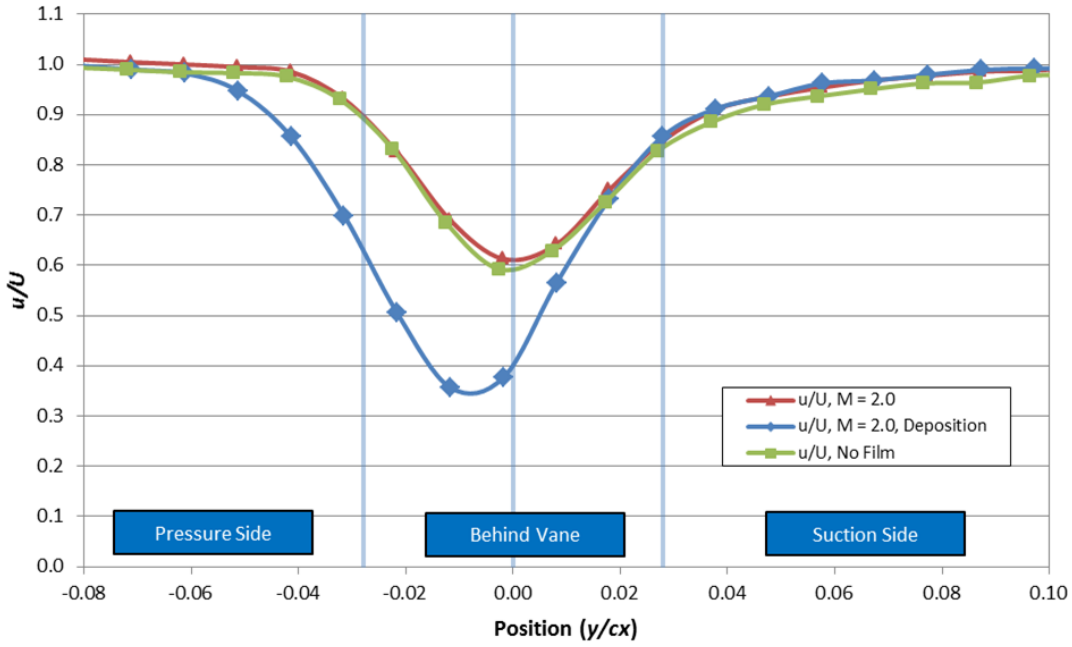

Figure 5.8: Velocity deficit in the wake of the vane without film cooling, with film cooling, and with deposition and film cooling

5.2.2. Wake Temperature

The wake temperature was measured to study how the increased turbulent mixing from the deposition convected the coolant away from the vane surface and into the wake. The wake temperature was non-dimensionalized in a similar manner as ϕ and defined as:

$$\theta = \frac{(T_\infty - T_{wake})}{T_\infty - T_{coolant,vane\ inlet}} \tag{5.1}$$

Figure 5.9 shows the wake temperature measurements with film cooling comparing the vane model with and without contaminant deposition. There was more coolant in the gas coming from the pressure side of the because there were film cooling holes on the pressure side whereas the suction side only had coolant from the showerhead and potentially further cooling due to convective cooling as the flow passed over the cooled vane surface. This was reflected in the wake temperature measurements, in Figure 5.9, where $\theta > 0.015$ up to y/c_x = -0.08 on the pressure side versus y/c_x = 0.06 on the suction side. In general, however, the wake temperature measurements without deposition were as expected.

The wake temperature measurements with and without deposition aligned on the suction side of the vane where there was little to no deposition. The wake temperature measurements with contaminant deposition showed a colder peak in wake temperature than the vane model without deposition. Additionally, in the far field, on the pressure side, the wake temperature was warmer when the vane had contaminant depositions on the surface. It was expected that the surface deposits would increase the turbulent mixing, convecting more of the coolant away from the vane surface. This would have decreased the peak θ in the wake, and increased the θ in the far field on the pressure side. However, this was the opposite of what was observed.

To verify the repeatability of this result because it contrasted what was expected, previously measurements in the wake of the vane were collected. Figure 5.10 shows several measurements of the wake temperature with and without deposition. These measurements were taken with $M = 4.0$, and the wake temperature was measured three separate times. These data showed the same trend as seen in Figure 5.9 where the wake temperature profile with deposition had a colder peak. The repeatability of these measurements between the two blowing ratios and three repeat of measurements for $M = 4.4$ gave confidence that this was the true result.

To help explain why the coolant was not being convected further from the wake centerline, Figure 5.11 shows the wake temperature and velocity deficit profiles on the same curve. The deviation between the two velocity deficit curves began at the same location as the deviation between the two temperature curves, and the curves converged at the same location as well. The lower velocity fluid was the colder fluid in the wake of the vane. Both configurations had the same coolant mass ejected from the coolant holes, so for the same coolant mass to pass through the wake, now mixed with the mainstream, at a slower velocity the gas, on average, must have been colder. Additionally, the deposition lowered the momentum flux of the coolant coming from the film cooling holes helping keep the coolant more coherent near to the vane surface, as observed in the overall and effectiveness plots.

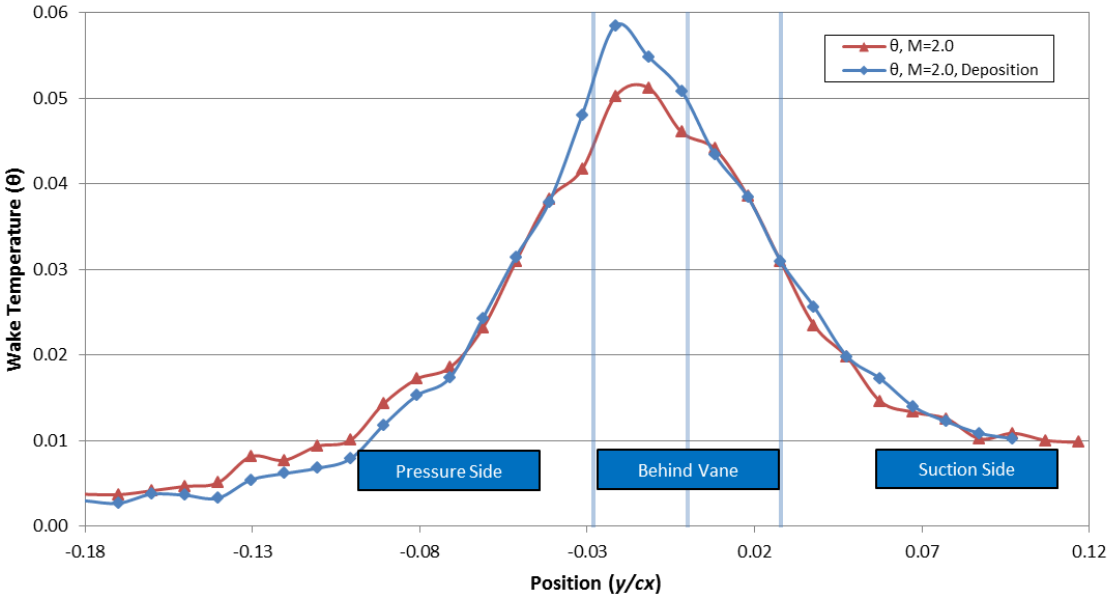

Figure 5.9: Temperature in the wake of the vane with and without deposition, *M*=0.6

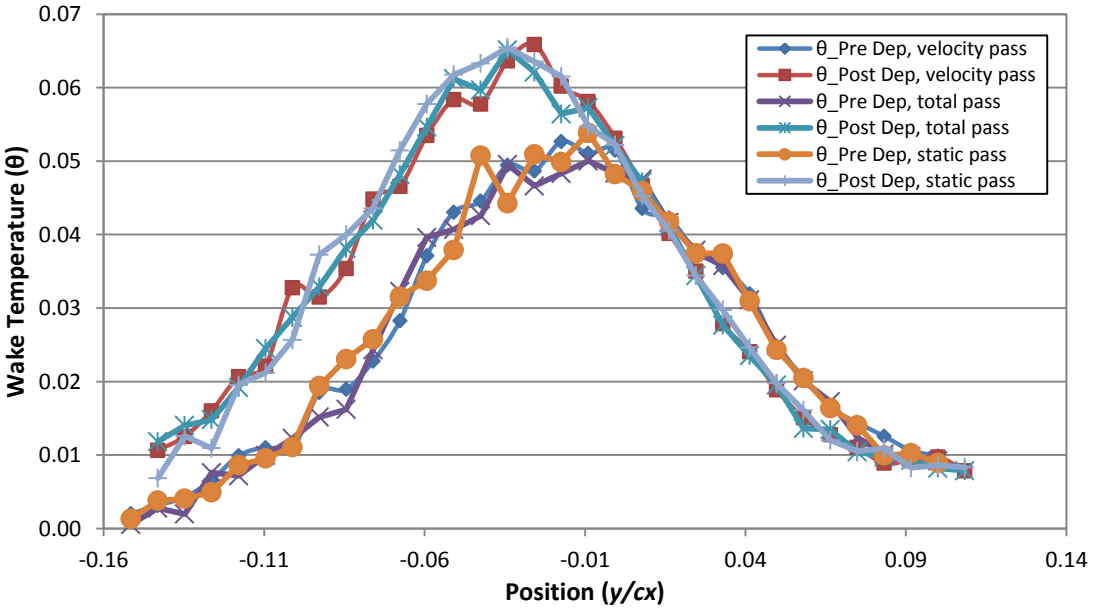

Figure 5.10: Wake temperature with and with deposition, M=4.0, repeatability check

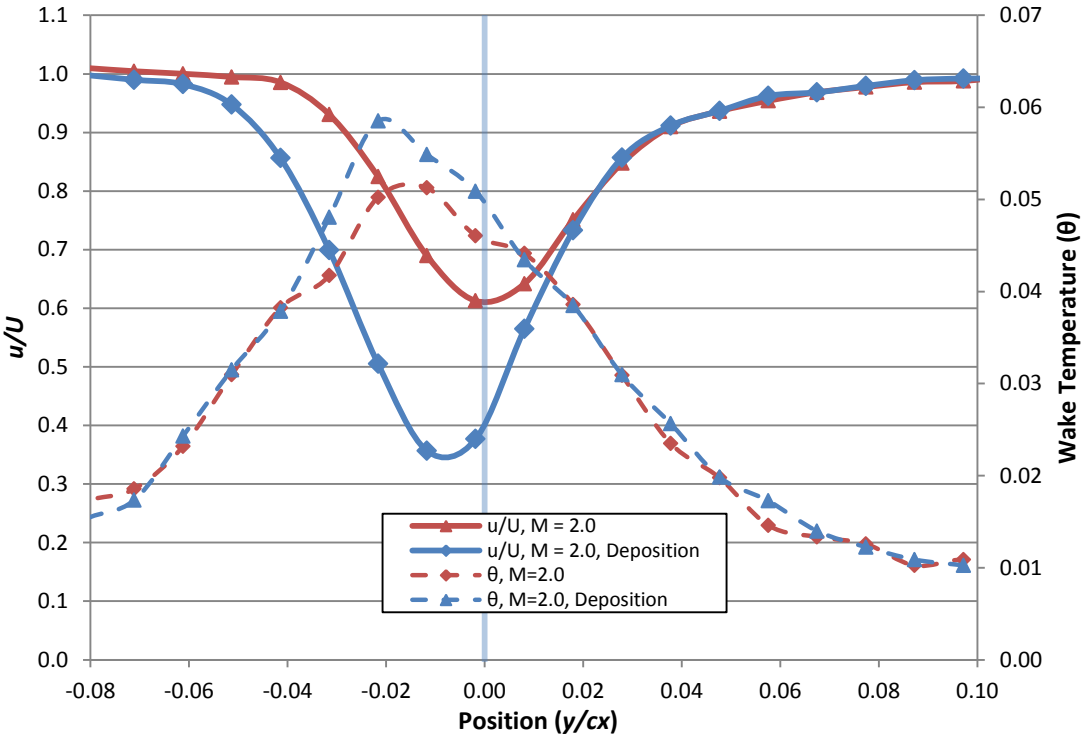

Figure 5.11: Velocity deficit and wake temperature with and without deposition, *M*=2.0

Chapter 6: Conclusions

One of the major goals of this study was to use 2-D thermal profiles of film cooling jets to better understand the accuracy of RANS models prediction of film cooling flow when compared to experimental measurements. These thermal field measurements also accomplished the goal of creating a complete comparison of film cooling jets above adiabatic and conducting vane models to be studied, so that the adiabatic wall temperature could be studied as the driving temperature for heat transfer. Additionally, the insulating properties of TBC were studied with an emphasis on understanding how the thickness of the TBC impacts the overall effectiveness. Finally, measurements of overall effectiveness and measurements in the wake of the vane with and without simulated contaminant deposition were studied.

6.1. Thermal Fields

Thermal field measurements were taken at three locations, x/d = 0, 5, and 10, downstream of a row of film cooling holes on the suction side of a vane model above an adiabatic vane wall and a thermally scaled matched Biot number vane wall. The two vane models were simulated computationally by Dyson et al. (2012), so that the thermal planes at x/d = 5 and 10 could be compared to the experimental measurements. Comparisons of adiabatic and overall effectiveness measurements between experiments and predictions previously revealed the inability of RANS models to predict film cooling effectiveness. The predictions of laterally average surface temperature were reasonable for some blowing ratios, but the contour plots revealed problems. However, these were studies of surface temperature which were limited to the footprint of the jet; thermal field measurements above the vane surface allowed for a more comprehensive comparison.

Convection within the coolant hole could have significantly altered the thermal profile of the coolant, so the thermal fields at $x/d = 0$ above the adiabatic and conducting vane models allowed for the hole-exit profiles to be compared. It was shown that the in-hole convection was shown did not alter the general thermal profile of the jet above the conducting vane model which allowed for the effect of the conducting wall to be isolated in the downstream thermal measurements. Additionally, the profiles at $x/d = 0$ showed the interaction of the film cooling jet and the upstream thermal boundary layer. These measurements revealed that the thermal boundary layer does not flow over the coolant jet but around it.

The thermal field measurements at x/d =5 and 10 were compared to the computational simulations using the k-ω SST RANS model of Dyson et al (Dyson, et al., 2012). The measurements in these comparisons revealed that the RANS model consistently under-predicted the level of lateral spreading of the coolant jet. The core temperatures of the simulated coolant jet from the RANS model were consistently colder than the core temperatures of the experimentally measured jets by $\Delta\theta = 0.40$. Additionally, for the coolant jets separated from the vane surface, the RANS model predicted a dominating effect of counter-rotating-vortices on the thermal profile, when the experimental measurements did not. However, the level of wall-normal spreading and the height of the core of the coolant jet were well predicted by the RANS model (Dyson, et al., 2012).

The k-ω SST RANS model assumes isotropic turbulence that decays near the wall, so in general the level of wall-normal mixing is well predicted, but the isotropy assumption causes significant under-predictions in the lateral mixing. The adverse effects of this assumption were revealed in these thermal field comparisons. The under-

prediction of turbulent mixing yielded colder core temperatures and narrower jets because the jets did not diffuse properly. The under-prediction of turbulent mixing also did allow the counter-rotating-vortex pair to be broken apart as the experimental measurements showed.

Several studies have previously studied the relationship between adiabatic and overall effectiveness and effects of internal and film cooling, but these studies were limited to measurements of surface temperature. The 2-D thermal profiles expanded these comparisons to better understand the effect of the conducting wall on the film cooling jet. For most cases, the conducting wall and boundary layer interaction did not significantly impact the thermal profile of the jet. When the coolant jet was attached to the vane surface, the thermal profiles above the adiabatic and conducting vane surfaces were almost identical, with the exception of a few cases very near the wall where conduction had a small effect on the thermal profile. However, the separated coolant jets showed greater deviation between the two sets of thermal fields. The separated coolant jets above the adiabatic vane model allowed hot mainstream gas to mix in underneath the jet, but the separated coolant jet above the conducting vane model allowed the cooled thermal boundary layer to mix in underneath the coolant jet. The effects of this difference were magnified farther downstream of the hole because a new thermal boundary layer would begin to develop underneath the separated coolant jet. Therefore, the comprehensive thermal field comparisons showed that the adiabatic wall temperature was a good indication of the driving temperature for heat transfer when the coolant jet was attached to the vane surface, and the adiabatic wall temperature was a poor indication of the driving temperature for heat transfer when the coolant jet was separated from the vane surface.

6.2. TBC THICKNESS EFFECTS

Davidson et al. (2012) used a matched Biot number model vane previously to study the combined effects of TBC, film cooling, and internal cooling. Davidson et al. showed that overall effectiveness was less sensitive to film cooling geometry and blowing ratio with TBC (Davidson, et al., 2012). Film cooling geometries that had proven to increase adiabatic effectiveness or film cooling effectiveness showed only slight improvements to overall effectiveness. The current study expanded that work by decreasing the thickness, and thus the insulating ability, of the TBC, to find if decreasing the thickness of TBC increases the sensitivity of overall effectiveness to film cooling geometry and blowing ratio. Additionally, the previously studied TBC thickness was near the high end of the range of thermal resistances, the TBC thickness used in this study was closer to the middle of this range.

The vane model had three rows of showerhead cooling on the leading edge and one pressure side row of round film cooling holes. The leading edge showed increasing overall effectiveness with increasing blowing ratio, and the leading edge had peak overall effectiveness values above ϕ = 0.8 for M =3.0. The pressure side of the vane had increased levels of overall effectiveness upstream of the row of film cooling holes due to convective cooling inside the coolant hole. The TBC insulated the vane surface allowing this in-hole convection to more effectively cool the vane wall. The increased level of effectiveness upstream of the coolant holes was greater for the higher blowing ratios. Downstream of the row of holes, however, the measurements with lower blowing ratios had higher overall effectiveness because, as the contour plots of external effectiveness showed, the lower blowing ratios were attached to the vane surface increasing the

cooling. Despite these trends, the variation in overall effectiveness with varying blowing ratios on the pressure side was small.

A realistic width trench was cut around the pressure side holes to embed them in a trench with depth $t/d = 0.6$. The trench height was too low to collect the coolant in the trench and allow for the coolant to spill over in a uniform "sheet". Instead, the exposed vane surface in the trench was warm between coolant holes and warmer than positions upstream or downstream of the trench. Effectiveness decreased with blowing ratio because high blowing ratios were separated from the vane surface and did not provide film cooling. However, under the TBC upstream or downstream of the trench, these variations in overall effectiveness were small compared to variations seen without TBC.

A simple 1-D heat transfer analysis was used to predict the overall effectiveness without film cooling but with TBC from overall effectiveness measurements without TBC. The prediction was shown to under-predict the overall effectiveness at all locations, but accounted for 80% of the difference between the two curves. However, an analogous analysis was conducted to predict the overall effectiveness with the thicker TBC, $t/d = 1.0$, from measurements of overall effectiveness with TBC, $t/d = 0.6$. This second prediction successfully estimated the overall effectiveness within uncertainty for all but one location on the vane. The second prediction was more successful because the 1-D heat transfer assumption was not true, but the heat transfer was most likely more similar between the two cases with TBC than one case with TBC and one with no TBC.

6.3. CONTAMINANT DEPOSITION EFFECTS

A wax spray technique was implemented to simulate contaminant depositions seen in gas turbine engines. The goal was to identify where the deposition accumulations

were focused, and its impact on cooling effectiveness. The deposition predominantly accumulated in the showerhead region and on the downstream edge of the realistic trench. The depositions were expected to increase the turbulent mixing because of increased surface roughness above the vane surface and therefore also increase the heat transfer coefficient. It was also expected to insulate the vane surface from the hot mainstream gas because the depositions had a low thermal conductivity which would add a layer of thermal resistance between the mainstream and the vane wall. Measurements of overall effectiveness with deposition showed improvements when compared to measurements without deposition. The insulating properties of deposition dominated over the increases in turbulent mixing. Additionally, the deposition on the edge of the realistic trench slowed the momentum of the coolant resulting in two things: allowing the coolant to collect in the trench and helping keep the coolant attached to the vane surface.

Wake measurements of temperature and velocity were made without film cooling, with film cooling from the showerhead and the pressure side, and with film cooling and deposition. Film cooling was shown to have no effect on the velocity profile of the wake of the vane. Deposition caused a significant increase in the velocity deficit in the wake of the vane near to the pressure side of the vane. This was consistent with the results that little to no deposition formed on the suction side of the vane, thus the wake profile was largely unchanged by deposition on this side.

Deposition was expected to increase turbulent mixing and convect the coolant away from the vane surface, but the opposite trend was observed where the wake with deposition had a colder temperature near the centerline and a warmer profile further from the centerline. It was speculated that the lower velocity regions of the wake with deposition aligned caused the colder regions of the wake with deposition. For a

consistent mass flow rate of film coolant, a slower mainstream gas was expected to have a colder temperature.

6.4. Recommendations for Future Work

CFD models such as LES or URANS are computationally much more expensive than RANS simulations, but they have the potential to more accurately predict film cooling effectiveness. Comparisons of surface temperatures and velocity fields between URANS simulations and experimental measurements have been conducted, but the literature is lacking a comparison of thermal fields. This comparison will be crucial to understanding the additional computational cost of URANS or LES is worthwhile.

Comprehensive thermal field measurements were taken for only a single row of film cooling holes, and these measurements could be expanded to include the interactions of multiple rows of film cooling jets. Several superposition models exist to predict the resulting film cooling effectiveness from several rows of film cooling holes, and these models have been investigated with surface temperature measurements. However, the interaction of the thermal boundary at the film cooling hole exit showed the thermal boundary layer did not develop over the coolant jet but around it. Upstream film cooling may interact in a similar fashion, or the upstream film cooling might increase the thickness of the thermal boundary layer resulting in a different type of interaction. The Sellers (1963) superposition model assumes the upstream coolant becomes the mainstream temperature in predicting the downstream adiabatic effectiveness. However, this assumes the upstream coolant flows over, not around, the downstream film cooling jet which was not observed in the interaction between the thermal boundary layer and

film cooling jet. Therefore, comprehensive thermal fields of this interaction could provide crucial insight into film cooling superposition models.

The thinner TBC thickness in this study showed that the insulating property of the TBC dominated over film cooling effectiveness, especially when compared to overall effectiveness measurements without TBC. Thus, further decreasing the thermal resistance of the TBC to find the threshold value at which film cooling effectiveness will increase the overall effectiveness would enhance our understanding of the TBC – film cooling interaction.

Finally, studies of overall effectiveness on turbine vane models with TBC have shown the strong cooling ability of in-hole convection. The measurements in this study showed significant increases in effectiveness at the location of the film cooling holes and even upstream of the holes. Therefore, flat plate studies of multiple rows of film cooling with TBC could expand our understanding of in-hole convection. In fact, overall effectiveness, especially upstream of the row of coolant holes, with TBC was less sensitive to film cooling geometry than it was to blowing ratio. Therefore, the most effective film cooling geometry and configuration for adiabatic effectiveness or a turbine vane without TBC is most likely not the most effective configuration for a vane model with TBC. Flat plate studies of the in-hole convection with TBC would enhance the understanding of the most effective cooling methods with TBC.

Bibliography

Albert, J. E., & Bogard, D. G. (2011). Experimental Simulation of Contaminant Deposition on a Film Cooled Turbine Vane Pressure Side with a Trench. *ASME Turbo Expo GT2011-46709*. Vancouver, Canada.

Albert, J., & Bogard, D. (2011). Measurements of Adiabatic Film and Overall Cooling Effectiveness on a Turbine Vane Pressure Side with a Trench. *ASME Turbo Expo GT2011-46703*.

Ames, F. (1998). Aspects of Vane Film Cooling with High Turbulence: Part II - Adiabatic Effectiveness. *J. Turbomach*, Vol. 120.

Bogard, D. G., & Thole, K. A. (n.d.). Gas Turbine Film Cooling. *22*(No. 2, March-April 2006).

Bunker, R. (2009). The Effects of Manufacturing Tolerances on Gas Turbine Cooling. *J. Turbomach*, Vol. 131.

Clarke, D., Oechsner, M., & Padture, N. (2012, October). Thermal-barrier coatings for more efficient gas-turbine engines. *Materials Research Society*, Vol. 37.

Crosby, J., Lewis, S., Bons, J., Ai, W., & Fletcher, T. (2008). Effects of Temperature and Particle Size on Deposition in Land Based Turbines. *13*.

Davidson, F., Kistenmacher, D., & Bogard, D. (2012). A Study of Deposition on a Turbine Vane with a Thermal Barriet Coating and Various Film Cooling Geometries. *ASME Turbo Expo*. GT2012-70033.

Davidson, F., Kistenmacher, D., & Bogard, D. (2012). Film Cooling with Thermal Barrier Coating: Round Holes, Craters, and Trenches. *ASME Turbo Expo*. GT2012-70092.

Dees, J., Bogard, D., Ledezma, G., & Laskowski, G. (2011). The Effects of Conjugate Heat Transfer on the Thermal Field Above a Film Cooled Wall. *ASME Turbo Expo*. GT2011-46617.

Dees, J., Bogard, D., Ledezma, G., & Laskowski, G. (2013). Overall and Adiabatic Effectiveness Values on a Scaled Up, Simulated Gas Turbine Vane. *J. Turbomach*, Vol. 135.

Dees, J., Bogard, D., Ledezma, G., Laskowski, G., & Tolpadi, A. (2009). Experimental Measurements and Computational Predictions for an Internally Cooled Simulated Turbine Vane. *IMECE*. 2009-11622.

Dees, J., Ledezma, G., Bogard, D. G., & Laskowski, G. (2012). Experimental and Computational Measurements for an Internally Cooled Simulated Gas Turbine Vane with 90 degree Rib Turbulators. *134*.

Dorrington, J., Bogard, D., & Bunker, R. (2007). Film Effectiveness Performance for Coolant Holes Embedded in Various Shallow Trench and Crater Depressions. *ASME Turbo Expo*. GT2007-27992.

Dyson, T. E., Bogard, D. G., & Bradshaw, S. D. (2012). Evaluation of CFD Simulations of Film Cooling Performance in the Showerhead Region of a Turbine Vane Including Conjugate Effects. (IMECE2012-88386).

Dyson, T., Bogard, D., & Bradshaw, S. (2012). Evaluation of CFD Simulations of Film Cooling Performance on a Turbine Vane Including Conjugate Heat Transfer Effects. *ASME Turbo Expo*. GT2012-69107.

Dyson, T., McClintic, J., Bogard, D., & Bradshaw, S. (2013). Adiabatic and Overall Effectiveness for a Fully Cooled Turbine Vane. *ASME Turbo Expo*. GT2013-94928.

Eckert, E. (1984). Analysis of Film Cooling and Full Coverage Film Cooling of Gas Turbine Blades. *Journal of Engineering Gas Turbines*, Vol. 106.

Eningeering ToolBox, The. (n.d.). Retrieved January 22, 2014, from http://www.engineeringtoolbox.com/thermal-conductivity-d_429.html

Ethridge, M., Cutbirth, J., & Bogard, D. (2001). Scaling of Performance for Varying Density Ratio Coolants on an Airfoil with Strong Curvature and Pressure Gradient Effects. *J. Turbomach*, Vol. 123.

Feurstein, A., & al., e. (2008). Technical and Economical Aspects of Current Thermal Barrier Coating Systems for Gas Turbine Engines by Thermal Spray and EBPVD: A Review. *Journal of Thermal Spray Techniques*, Vol. 17(2). pp. 199-213.

Gladden, H. J., & Liebert, C. H. (1980). Effects of a Cermaic Coating on Metal Temperatures of an Air-Cooled Turbine Vane.

Hamed, A., Tabakoff, W., & Wenglarz, R. (2006). Erosion and Deposition in Turbomachinery. *22*(No. 2, March-April 2006).

Han, J., Dutta, S., & Ekkad, S. (2000). *Gas Turbine Heat Transfer and Cooling Technology*. New York, USA: Taylor and Francis.

Harrison, K., & Bogard, D. (2008). Comparison of RANS Turbulence Models for Prediction of Film Cooling Performance. *ASME Turbo Expo*. GT2008-51423.

Incropera, F., & De Witt, D. (1990). *Fundamentals of Heat and Mass Transfer*. New York: John Wiley & Sons, Inc.

Kistenmacher, D., Davidson, F., & Bogard, D. (2013). Realistic Trench Film Cooling with a Thermal Barrier Coating and Deposition. *ASME Turbo Expo*. GT2013-95921.

Leylek, J., & Zerkle, R. (1994). Discrete-Jet Film Cooling: A Comparison of Computational Results with Experiments. *J. Turbomach*, Vol. 116.

Maikell, J., Bogard, D., Piggush, J., & Kohli, A. (2009). Experimental Simulation of a Film Cooled Turbine Blade Leading Edge Including Thermal Barrier Coating Effects. *ASME Turbo Expo*. GT2009-60286.

Mathew, S., Ravelli, S., & Bogard, D. (2011). Evaulation of CFD Predictions Using Thermal Field Measurements on a Simulated Film Cooled Turbine Blade Leading Edge. *ASME Turbo Expo*. GT2011-46619.

Matias, L., Santos, C., M., R., & Gil, L. (1997). Declared value for the thermal conductivity coefficient of insulation corkboard. *31*.

Na, S., Williams, B., Dennis, R., Bryden, K., & Shih, T.-P. (2007). Internal and Film Cooling of a Flate Plate with Conjugate Heat Transfer. *ASME Turbo Expo*. GT2007-27599.

Nathan, M., Dyson, T., Bogard, D., & Bradshaw, S. (2012). Adiabatic and Overall Effectiveness for Showerhead Film Cooling of a Turbine Vane. *ASME Turbo Expo*. GT2012-69109.

Patrylak, R., & Donnelly, A. (2013). *2013 Energy Market Outlook and Industry Trends*. Black and Veach.

Pichon, Y. (2009). *Turbulence Field Measurements for the Large Windtunnel.* The University of Texas at Austin. TTCRL Internal Report.

Schmidt, P. S., Ezekoye, O. A., Howell, J. R., & Baker, D. K. (2006). Thermodynamics. Hoboken, NJ: John Wiley & Sons.

Sellers, J. (1963). Gaseous Film Cooling with Multiple Injection Stations. *AIAA*, 2154-2156.

Special Metals Corporation. (2004, September). *Inconel alloy X-750 Data Sheet, Publication No. SMC-067.* Retrieved from www.specialmetals.com

Unger, D., & Herzog, H. (1998). *Comparative Study on Energy R&D Performance: Gas Turbine Case Study.* Massachusetts Institute of Technology Energy Laboratory.

United States. (2012). *Annual Energy Review 2011.* Department of Energy. Energy Information Administration.

United States. (2013). *Monthly Energy Review August 2013.* Department of Energy. Energy Information Adminsistration.

Vasudev, S. (2006). Effects of Gas Radiation in Scaled Cooling Effectiveness Tests of Turbine Vanes. *AIAA.* Sacramento, CA.

Voigt, S., & Noll, B. A. (2010). Aerodynamic Comparison and Validation of RANS, URANS, and SAS Simulations of Flat Plate Film-Cooling. *ASME Turbo Expo.* GT2010-22475.

Walsh, P. M., Sayre, A., Loehden, D., Monroe, L., Beér, J., & Sarofim, A. (1990). Deposition of Bituminuous Coal Ash on an Isolated Heat Exchanger Tube: Effects of Coal Properties on Deposit Growth. *Progress in Energy and Combustion Science, 16*, 327-346.

Wenglarz, R., & Fox, R. (1990). Physical Aspects of Deposition From Coal Water Fuels Under Gas Turbine Conditions. *112*, 9-14.

Williams, R., Dyson, T., & Bogard, D. (2012). Sensitivity of the Overall Effectivenesss for a Turbine Vane to Film Cooling and Internal Cooling. *ASME Turbo Expo.* GT2012-69110.

Vita

William Robb Stewart was born in Dallas, Texas in 1989. There he graduate from Lake Highlands High School in 2008 and moved to Austin. He attended the University of Texas at Austin (UT) and graduated with a Bachelor of Science in Mechanical Engineering in 2012. William began graduate school at UT in August 2012 where he conducted research in the Turbulence and Turbine Cooling Laboratory. He began work in the Edison Engineering Development Program at GE Global Research upon completion of his Master's degree in May 2014.

Permanent email: rstewart358@gmail.com

This thesis was typed by the author.